

<b>REPORT DOCUMENTATION PAGE</b>				<i>Form Approved OMB No. 0704-0188</i>	
<p>The public reporting burden for this collection of information is estimated to average 1 hour per response, including the time for reviewing instructions, searching existing data sources, gathering and maintaining the data needed, and completing and reviewing the collection of information. Send comments regarding this burden estimate or any other aspect of this collection of information, including suggestions for reducing the burden, to the Department of Defense, Executive Service Directorate (0704-0188). Respondents should be aware that notwithstanding any other provision of law, no person shall be subject to any penalty for failing to comply with a collection of information if it does not display a currently valid OMB control number.</p> <p><b>PLEASE DO NOT RETURN YOUR FORM TO THE ABOVE ORGANIZATION.</b></p>					
<b>1. REPORT DATE</b> (DD-MM-YYYY)		<b>2. REPORT TYPE</b>		<b>3. DATES COVERED</b> (From - To)	
<b>4. TITLE AND SUBTITLE</b>				<b>5a. CONTRACT NUMBER</b>	
				<b>5b. GRANT NUMBER</b>	
				<b>5c. PROGRAM ELEMENT NUMBER</b>	
<b>6. AUTHOR(S)</b>				<b>5d. PROJECT NUMBER</b>	
				<b>5e. TASK NUMBER</b>	
				<b>5f. WORK UNIT NUMBER</b>	
<b>7. PERFORMING ORGANIZATION NAME(S) AND ADDRESS(ES)</b>				<b>8. PERFORMING ORGANIZATION REPORT NUMBER</b>	
<b>9. SPONSORING/MONITORING AGENCY NAME(S) AND ADDRESS(ES)</b>				<b>10. SPONSOR/MONITOR'S ACRONYM(S)</b>	
				<b>11. SPONSOR/MONITOR'S REPORT NUMBER(S)</b>	
<b>12. DISTRIBUTION/AVAILABILITY STATEMENT</b>					
<b>13. SUPPLEMENTARY NOTES</b>					
<b>14. ABSTRACT</b>					
<b>15. SUBJECT TERMS</b>					
<b>16. SECURITY CLASSIFICATION OF:</b>			<b>17. LIMITATION OF ABSTRACT</b>	<b>18. NUMBER OF PAGES</b>	<b>19a. NAME OF RESPONSIBLE PERSON</b>
a. REPORT	b. ABSTRACT	c. THIS PAGE			<b>19b. TELEPHONE NUMBER</b> (Include area code)

ONR Award No: N00014-16-1-2738

**FINAL PROJECT REPORT:**  
**Unified *In Vivo/Ex Vivo* Sensing Architectures for Monitoring  
Osseointegrated Prosthetics**

**Report Authors:**

Prof. Jerome Lynch, University of Michigan, Ann Arbor, MI

Dr. Wentao Wang, University of Michigan, Ann Arbor, MI

Dr. Peng Sun, University of Michigan, Ann Arbor, MI

Dr. Andrew Burton, University of Michigan, Ann Arbor, MI

**Principle Investigator:**

Jerome P. Lynch

Professor, Civil and Environmental Engineering

Professor, Electrical Engineering and Computer Science

2380 G. G. Brown Building

University of Michigan

Ann Arbor, MI 48109-2125

[jerlynch@umich.edu](mailto:jerlynch@umich.edu)

**Program Managers:**

Dr. Liming Salvino and Dr. Tim Bentley

Office of Naval Research

Code 342

**Date of Report:**

September 30, 2018

## TABLE OF CONTENTS

EXECUTIVE SUMMARY.....	3
SECTION 1: PROJECT OVERVIEW .....	4
SECTION 2: GUIDE WAVE THEORY AND ITS APPLICATION TO OSSEOINTEGRATED PROSTHESES .....	7
SECTION 3: <i>EX VIVO</i> MONITORING TO ASSESS HEALING IN OSSEOINTEGRATED PROSTHESES USING GUIDED WAVES .....	24
SECTION 4: DETECTION OF BONE FRACTURE IN OSSEOINTEGRATED PROSTHESES USING FLEXURAL MODES.....	35
SECTION 5: DEVELOPMENT OF BIO-COMPATIBLE WIRELESS INDUCTIVE THIN FILM STRAIN SENSOR FOR BONE GROWTH MONITORING .....	45
SECTION 6: CHARACTERIZATION AND EXPERIMENTS OF THE BIO-COMPATIBLE WIRELESS INDUCTIVE THIN FILM STRAIN SENSOR .....	54
SECTION 7: CONCLUSIONS.....	69
REFERENCES.....	71

## EXECUTIVE SUMMARY

Advances in medicine have led to the development of prostheses that can be integrated directly to the host bone of residual limbs. Osseointegration of the prosthesis comes with many benefits including its use in patients with short residual limbs. There are also a number of challenges associated with their use including high rates of tissue infection, the potential for loosening, and uncertainty in determining when the limb can be loaded after surgery. Clinical approaches to addressing these challenges have been largely qualitative in nature. Recent advances in sensing technologies and data analytics has created the opportunity to develop a quantitative approach to monitoring osseointegrated (OI) prostheses to assess their integration after surgery and performance well after surgery. Hence, the overarching goal of this Office of Naval Research (ONR) project was to develop a comprehensive monitoring architecture that could monitor OI prostheses starting at the post-operative stage and continuing through the prosthesis lifespan. A unified *in vivo/ex vivo* sensing architecture was explored to monitor OI prostheses. First, the effort explored the adoption of *ex vivo* sensors that could be attached to the percutaneous extension of the OI prosthesis. In particular, piezoelectric transducers were studied to introduce body waves into the prosthesis to assess its structural condition and the degree of integration with the host bone. Experimental tests were done to verify the ability for guided waves to assess integration, OI prosthesis loosening, and fracture in the host bone. Second, biocompatible thin film sensors were considered for *in vivo* placement in the host limb to monitor the mechanical behavior of the OI prosthesis and bone. Additive thin film manufacturing of lithographically patterned materials on biocompatible thin film substrates was advanced to create an array of sensing transducers including those capable of measuring strain and bone growth. Inductive wireless interfaces were integrated in the thin film sensors to provide a means of powering and reading sensor outputs from outside the limb. The *in vivo* and *ex vivo* sensing strategies were unified into a single monitoring system through the use of a compact wireless sensing node that interrogates the *in vivo* sensors (through inductive coupling) and *ex vivo* sensors. Again, experimental testing is performed to show the resolution of thin film sensors for OI prostheses.

This report is organized into five main sections. The overview of the project is first presented in Section 1 including a description of the unified *in vivo/ex vivo* sensing strategy for monitoring OI prostheses. Sections 2 through 4 report on the use of guided waves generated by thin piezoelectric elements mounted to the percutaneous end of the OI prosthesis to identify prosthesis fixture integration with bone in addition to bone fracture after integration has occurred. These three sections provide a theoretical basis to the guided wave approach before presenting extensive experimental validation of the approach. In Section 5, the report introduces the design and fabrication of thin film circuit primitives for a thin film sensing circuit including a strain-sensitive parallel plate capacitor, spiral coil inductor for wireless coupling, and resistive fuse element for peak strain detection. In Section 6, the individual circuit elements are fabricated into a thin film wireless sensor for strain monitoring of bone; the integrated sensors are numerically and experimentally validated to ensure performance is as designed. Finally, Section 7 serves as a summary of key project achievements and a discussion of future work in the area.



## SECTION 1: PROJECT OVERVIEW

Globally 9 million people are affected by traumatic limb loss with nearly 2 million of them living in the United States<sup>1</sup>. While the socket prosthesis design is the most widely used prosthesis today, it has many drawbacks. Socket prostheses can be difficult to fit properly with slight changes in amputee tissue mass leading to discomfort and skin irritation; additional difficulties are presented by unbalanced load transfer from the artificial limb to the skeletal system<sup>2, 3</sup>. Osseointegrated (OI) prosthesis is an alternative to the socket prosthesis. OI prostheses are surgically implanted fixtures that are placed in the limb bone with a percutaneous end extending out of the limb for attachment of an artificial limb (Figure 1)<sup>4, 5</sup>. The benefits of OI prostheses are enormous including use in patients with limbs too short for a socket prosthesis and reports of amputees considering the prosthesis as a natural extension of their own bodies.

OI prostheses have been in use for decades and are based on the approach of dental implants which osseointegrate an implant into the jawbone. There are many OI prostheses designs that have been proposed and adopted by the orthopedic community. As shown in Figure 2, three OI prosthetic designs exist in the market including<sup>6</sup>: screw-shaped titanium prostheses (*e.g.*, OPRA marketed by Integrum), press-fit chrome cobalt molybdeen alloy or titanium prostheses (*e.g.*, those marketed by ESKA/OrthoDynamics/Permedica), and compression titanium prostheses (*e.g.*, marketed by Zimmer-Biomet). The OPRA and press-fit devices are the most common osseointegrated designs and consist of solid rod fixtures that are surgically implanted into the host bone.

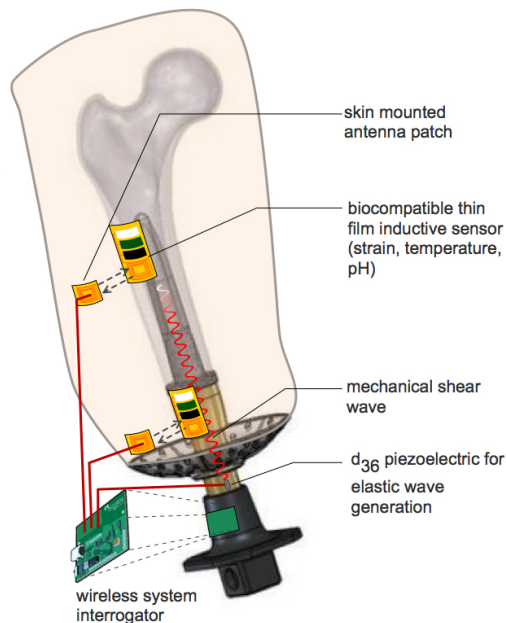


Figure 1. Proposed unified *in vivo* and *ex vivo* sensing architecture for monitoring of osseointegrated (OI) prostheses (OI prostheses consist of a metallic fixture implanted in bone with an artificial limb attached to a percutaneous end)

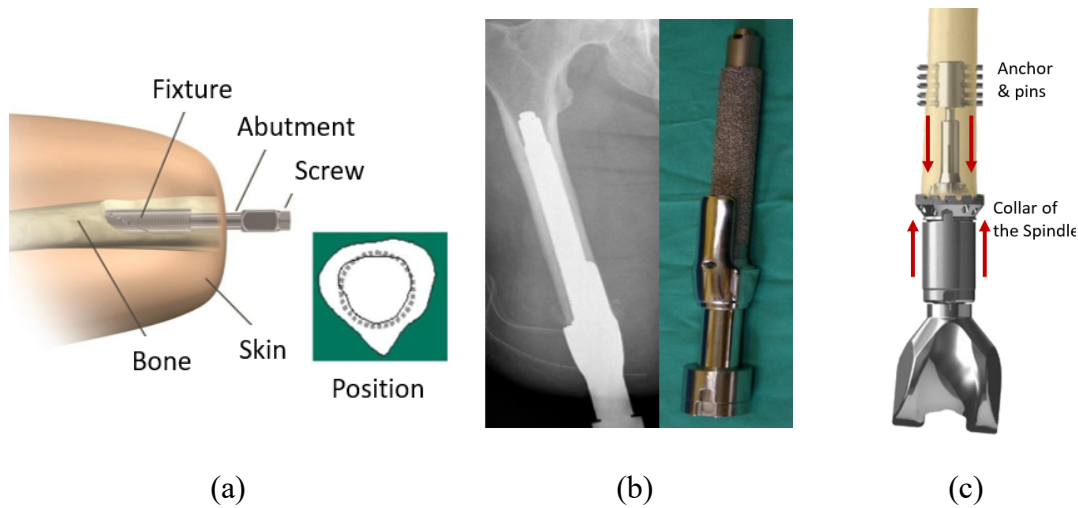


Figure 2. Osseointegrated prosthetic designs: (a) screw-shaped titanium prostheses, (b) press-fit titanium prostheses, and (c) compression titanium prostheses.

While OI prostheses eliminate many of the drawbacks of socket prostheses, they have their own limitations. First, there is a lack of quantitative methods that can ascertain when an OI prosthesis can be loaded. Rehabilitation protocols that govern when an osseointegrated prosthesis can be loaded is based on doctor judgment. Additional limitations include: 1) long-term risk exposure of tissue and bone to infections due to biofilms entering the limb via the prosthesis, and 2) bone fracture during the life of the prosthesis. There is a growing need to monitor the integration and long-term performance of OI prostheses in order to accurately identify when a prosthesis can be loaded. Monitoring can also help to identify issues such as loosening of the prosthesis fixture and fracture in the host bone over time. Currently, clinical evaluation of osseointegration is mostly based on X-ray imaging. The method is qualitative due to doctor interpretation of X-ray images; patients are also exposed to radiation <sup>7, 8</sup>. In addition, X-ray techniques cannot be used to measure the bone-interface because of diffraction effects due to the presence of titanium <sup>9, 10</sup>.

Directly needed are clinical methods that offer postoperative methods of quantitatively characterizing the osseointegration of the prosthesis. This proposal explores the adoption of structural monitoring technologies to monitor the structural mechanics of the OI prosthesis. Monitoring technologies have rapidly matured over the past five decades leading to low cost sensors with high sensing accuracy. The overarching goal of this project is to develop a comprehensive monitoring strategy optimized for OI prostheses to provide the medical community quantifiable data pertaining to: 1) post-operative healing processes occurring in bone and tissue after osseointegration, and 2) long-term performance of the bone-prosthesis system over the lifecycle of the prosthesis. The key research objectives necessary to achieve this goal include:

- Exploration of using the percutaneous extension of an OI prosthesis to generate guided waves thereby using the prosthesis as a wave guide that can interrogate the bone-prosthesis interface;

- Creation of an *ex vivo* sensing approach to provide quantitative data that allows the post-operative healing processes occurring in bone to be observed
- Extension of the *ex vivo* sensing approach to identify distress in the OI prosthesis including loosening and bone fracture;
- Design an *in vivo* thin film wireless sensing systems for strain sensing of prosthesis and host bone using a wireless interrogator outside of the body;
- Development of a wearable wireless node designed as a data acquisition system to interrogate the *in vivo* and *ex vivo* sensors.

The project can be divided into two major thrusts: *ex vivo* monitoring using guided waves and *in vivo* thin film wireless sensors to monitor bone strain in OI prostheses. As shown in Figure 1, the *ex vivo* sensing strategy consists of piezoelectric wafers bonded to the surface of the prosthesis outside the limb on the percutaneous end. These piezoelectric wafers can act as an actuator generating elastic stress waves into the fixture based on an applied voltage field to the piezoelectric. The stress waves generated would propagate along the longitudinal axis of the prosthesis with the prosthesis fixture serving as a wave guide. Upon interaction with bone, the wave properties would change before reflecting back to the percutaneous end. The piezoelectric wafers can also serve as sensors that convert the received stress waves into an electrical voltage that can be read by a data acquisition system. It is hypothesized that the guided waves will be sensitive to fundamental changes in the bone-metal interface at which osseointegration occurs. Changes at the interface including post-surgical osseointegration, loosening, and bone fracture would imprint unique changes on the guided waves allowing for clinical evaluation of the OI prosthesis condition.

The *in vivo* sensing strategy is intended to extend the reach of a OI prosthesis monitoring system to the bone supporting the OI prosthesis fixture. Currently, no viable option exists for implantable sensing of the host bone. Monitoring the bone is critical compress-type OI prosthesis which rely on post-tensioning of the fixture to induce permanent axial compression of the bone thereby stimulating bone growth and osseointegration with the fixture. Sensors implanted in the body must be fully biocompatible and free of reliance on a power source coupled with the sensor. Hence, wireless inductive coupling with the implanted sensor is one of the few approaches to powering implanted sensors. The *in vivo* sensing strategy relies on thin film sensors fabricated in a clean room environment using biocompatible materials including biocompatible polymers (*e.g.*, polyimide, parylene) and metals (*e.g.*, gold, titanium). Thin films have seen widespread use for sensors in a number of biomedical applications. In this project, an approach to layering different circuit elements associated with a resistor-inductor-capacitor (RLC) circuit is adopted to create a thin film sensor capable of being wirelessly powered and read. The sensor is designed with two approaches to reading its measurement: strain-sensitive capacitor and a fuse for detection of peak strain associated with circumferential bone growth in a compress-type OI prosthesis. After attachment to the bone during surgical implantation of the prosthesis fixture, the thin film sensor can be interrogated from outside the body using an inductive antenna attached to a frequency spectrum analyzer as shown in Figure 1.

## SECTION 2: GUIDE WAVE THEORY AND ITS APPLICATION TO OSSEOINTEGRATED PROSTHESES

### INTRODUCTION

The concept of the osseointegrated prosthesis is based on the success of dental implants which are osseointegrated into the jaw bone <sup>11, 12</sup>. The prosthesis consists of a metallic rod or structural anchor that is surgically inserted into the bone of the limb with the prosthesis exposed through the skin and an artificial limb is attached to a protruding taper adapter <sup>13, 14</sup>. As previously presented, Figure 2 shows the three major OI prostheses in current use based on screw implantation, press fitting, and compressive pre-stressing. The *ex vivo sensing* strategy proposed in this project are especially well suited for the screw and press fit fixture designs due to their cylinder-like geometric designs.

Guided wave methods are an ideal candidate because sensors can be installed outside the body but the prosthesis can be leveraged as a wave guide where guided waves will effectively interrogate the bone-prosthesis interface <sup>15</sup>. The proposed *ex vivo* approach to monitoring the healing and long-term performance of OI prostheses consists of piezoelectric wafer elements bonded to the surface of the percutaneous end of the prosthesis (Figure 3). The elastic stress waves generated in the prosthesis fixture will propagate along the longitudinal axis of the prosthesis <sup>14</sup>. The strategy of exploiting the prosthesis as a wave guide is attractive because it effectively allows sensors to be placed outside of the human body to interrogate the properties of the bone-prosthesis interface where osseointegration will occur after placement of the prosthesis. Placement of sensors outside of the body avoid issues associated with biocompatibility and reduce the regulatory requirements of taking the sensors to market. In addition to assessing osseointegration after surgery, guided waves also offer a method of tracking the long-term performance of the interface to detect issues such as loosening of the prosthesis attributed to bone infection and fracture of the host bone.

To explore the feasibility of guided waves as part of a broader *ex vivo* sensing strategy, this section will establish the mathematical principles of guided waves in titanium cylindrical rods implanted in bone as shown in Figure 3. The surrounding soft tissue of the limb will be ignored to allow investigation of the prosthesis-bone system. The principles of guided waves will be validated in this section using a titanium rod implanted in a high density polyethylene (HDPE) which has a modulus and density similar to mammalian bone. An important contribution of the section is the theory of tuning the guided waves in solid cylindrical rods assuming ideal bonding of a piezoelectric wafer. The piezoelectric material used in this study is a piezoelectric ceramic termed lead zirconate titanate ( $\text{Pb}[\text{Zr}_{(x)}\text{Ti}_{(1-x)}]\text{O}_3$  or simply “PZT”) which is a  $d_{31}$ -type piezoelectric that is often used in structural health monitoring to generate guided waves in structures. The optimization of the length of the PZT and the excitation frequency are achieved based on the tuned curve of longitudinal waves to enhance the accuracy of the proposed technique.

## GUIDED WAVE THEORY

Consider an elastic, isotropic solid titanium rod defined in cylindrical coordinates (where  $r$ ,  $z$  and  $\theta$  are the radial, longitudinal, and angular coordinates, respectively) as shown in Figure 3. Waves in an elastic, isotropic body with no body forces applied can be analytically expressed by Navier equations in cylindrical coordinates<sup>16-18</sup>. Navier equations are often simplified to describe displacements in a body,  $\mathbf{u}$ , as a sum of a dilational scalar potential,  $\Phi$ , and an equivoluminal vector potential field,  $\mathbf{H}$ . In the case of a solid rod, the boundary at the rod surface ( $r = R$ ) is assumed to be traction-free where the state of stress is stated as  $\sigma_{rr} = \sigma_{r\theta} = \sigma_{rz} = 0$ . Fundamentally, the scalar potential field  $\Phi$  and vector potential field  $\mathbf{H}$  satisfy the following wave equations<sup>17, 18</sup>:

$$\frac{\partial^2 \Phi}{\partial r^2} + \frac{1}{r} \frac{\partial \Phi}{\partial r} + \frac{1}{r^2} \frac{\partial^2 \Phi}{\partial \theta^2} + \frac{\partial^2 \Phi}{\partial z^2} = \frac{1}{c_p^2} \frac{\partial^2 \Phi}{\partial t^2} \quad (1)$$

$$\begin{aligned} & \left( \nabla^2 H_r - \frac{H_r}{r^2} - \frac{2}{r^2} \frac{\partial H_\theta}{\partial \theta} \right) \bar{\mathbf{e}}_r + \left( \nabla^2 H_\theta - \frac{H_\theta}{r^2} + \frac{2}{r^2} \frac{\partial H_r}{\partial \theta} \right) \bar{\mathbf{e}}_\theta + \nabla^2 H_z \bar{\mathbf{e}}_z \\ & = \frac{1}{c_s^2} \frac{\partial^2 \mathbf{H}}{\partial t^2} \end{aligned} \quad (2)$$

where  $\nabla^2$  is the 3-dimensional Laplace operator,  $c_p = \sqrt{\lambda + 2\mu/\rho}$  and  $c_s = \sqrt{\mu/\rho}$  are the pressure and shear wave velocities in the medium (which are 6070 m/s and 3310 m/s for titanium, respectively),  $t$  is time,  $\rho$  is the material density,  $\mu$  is the material shear modulus,  $\lambda$  is the material Lamé constant,  $H_r$ ,  $H_\theta$ , and  $H_z$  are the components of vector potential function  $\mathbf{H}$  in cylindrical coordinates, and  $\bar{\mathbf{e}}_r$ ,  $\bar{\mathbf{e}}_\theta$ , and  $\bar{\mathbf{e}}_z$  are the unit basis vectors that define the cylindrical coordinate system itself.

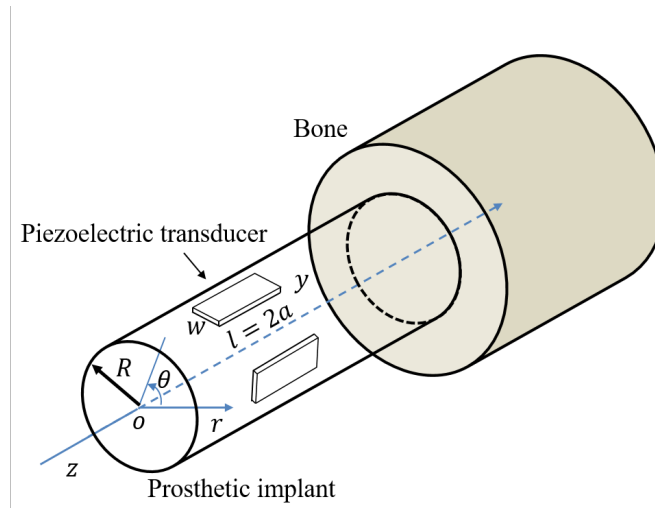


Figure 3. Schematic of the prosthesis-bone model coordinate system with PZT wafers shown on the prosthesis fixture.

The components of the scalar and vector fields in equations (1) and (2) for harmonic waves are of the form<sup>18</sup>:

$$\Phi = f \cdot \cos n\theta \cos(\omega t + \xi z) = A J_n(\alpha r) \cos n\theta \cos(\omega t + \xi z) \quad (3)$$

$$H_r = h_r \cdot \sin n\theta \sin(\omega t + \xi z) = B J_{n+1}(\beta r) \sin n\theta \sin(\omega t + \xi z) \quad (4)$$

$$H_\theta = h_\theta \cdot \cos n\theta \sin(\omega t + \xi z) = -B J_{n+1}(\beta r) \cos n\theta \sin(\omega t + \xi z) \quad (5)$$

$$H_z = h_z \cdot \sin n\theta \cos(\omega t + \xi z) = C J_n(\beta r) \sin n\theta \cos(\omega t + \xi z) \quad (6)$$

where  $\alpha^2 = \frac{\omega^2}{c_p^2} - \xi^2$ ,  $\beta^2 = \frac{\omega^2}{c_s^2} - \xi^2$ ,  $n$  is the wave order (which is an integer value of zero or greater),  $J_n$  are Bessel's functions of the first kind,  $\xi$  is the wavenumber,  $\omega$  is the angular frequency, and  $A$ ,  $B$ , and  $C$  are constants. Substituting the components stated in equations (3) to (6) into equations (1) and (2), the displacement field can be stated<sup>17, 18</sup>:

$$u_r = \left[ \frac{df}{dr} + \frac{n}{r} h_z + \xi h_r \right] \cos n\theta \cos(\omega t + \xi z) \quad (7)$$

$$u_\theta = \left[ -\frac{n}{r} f + \xi h_r - \frac{dh_z}{dr} \right] \sin n\theta \cos(\omega t + \xi z) \quad (8)$$

$$u_z = \left[ -\xi f - \frac{dh_r}{dr} - \frac{n+1}{r} h_r \right] \cos n\theta \sin(\omega t + \xi z) \quad (9)$$

The general displacement field in the rod can be decomposed into three harmonic wave modes: longitudinal modes,  $L(0, m)$ , which exist when  $u_\theta$  vanishes, torsional modes,  $T(0, m)$ , which exist when  $u_r$  and  $u_z$  both vanish, and flexural modes,  $F(n, m)$ , which consist of all three displacement components, where the mode order is defined by  $n$  and the mode number is defined by integer values of  $m$ <sup>19</sup>. The longitudinal and torsional modes are axially symmetric while the flexural modes are non-axisymmetric<sup>16, 17</sup>. The generation of different guided wave modes depends on the piezoelectric element type used, spatial configuration of the piezoelectric element, and the nature of the excitation signal. Guided waves in a rod exhibit velocity dispersion (except for the lowest order torsional mode) which means the propagation velocity of the mode varies with the excitation frequency. In this study, a prosthetic fixture implanted in bone will be a titanium rod with a 15.9 mm diameter (the material properties for titanium considered herein are: elastic modulus ( $E$ ) of 110 GPa, density ( $\rho$ ) of 4330 kg/m<sup>3</sup>, and Poisson's ratio ( $\nu$ ) of 0.30). Figure 4 presents the theoretical phased velocities and group velocities of the various wave modes in a 15.9 mm diameter titanium<sup>17</sup>. Figure 5 also pictures the  $L(0,1)$ ,  $T(0,1)$  and  $F(1,1)$  wave modes in the same rod.

In order to introduce the desired fundamental longitudinal wave into the titanium rod, a three-cycle Hanning window tone-burst signal is employed as the excitation signal:

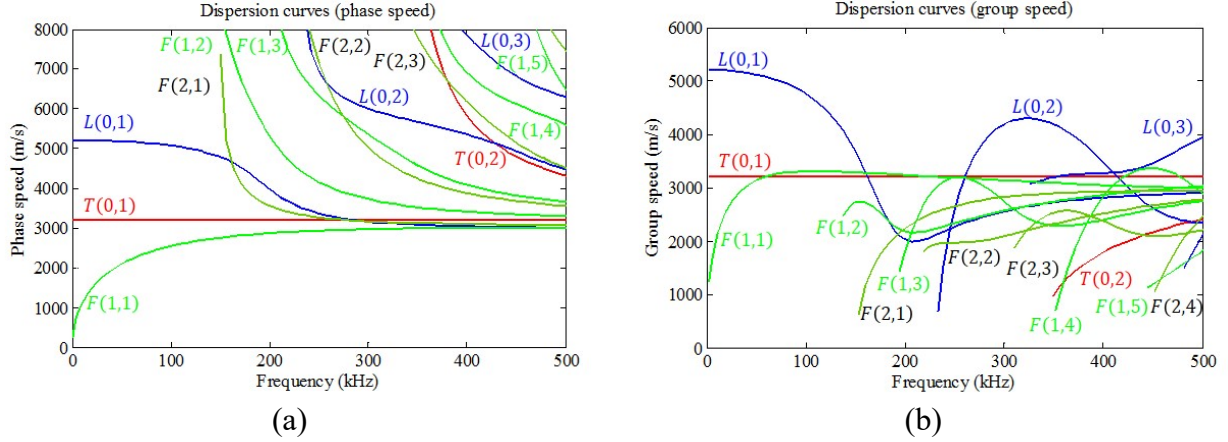


Figure 4. Dispersion curves of ultrasonic guided waves in a solid titanium 15.9 mm diameter rod: (a) phase velocity and (b) group velocity

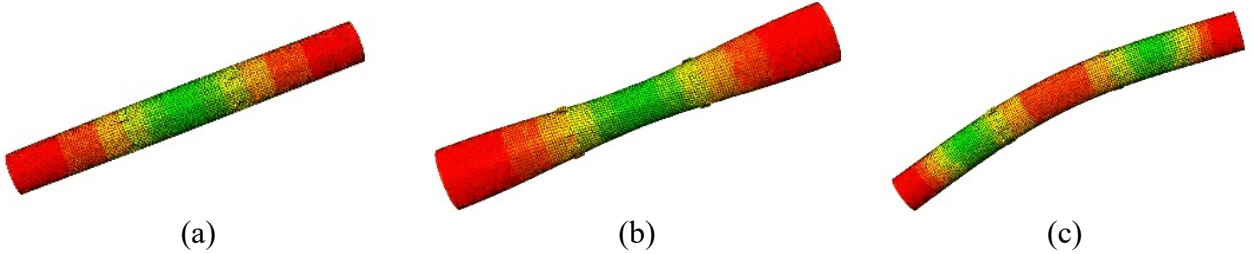


Figure 5. First fundamental wave mode in a solid titanium 1.58 cm diameter rod: (a)  $L(0,1)$ , (b)  $T(0,1)$ , and (c)  $F(1,1)$  modes.

$$V(t) = A_w [H(t) - H(t - N_c/f_c)] \left(1 - \cos \frac{2\pi f_c t}{N_c}\right) \sin(2\pi f_c t) \quad (10)$$

where  $A_w$  is the wave amplitude,  $H(t)$  is the Heaviside function, and  $N_c = 3$  and  $f_c$  are the cycle numbers and the center frequency of the excitation signal, respectively. The center frequency is selected to ensure higher order modes are not introduced and to maximize the strain field based on the size of the PZT element (as will be discussed later).

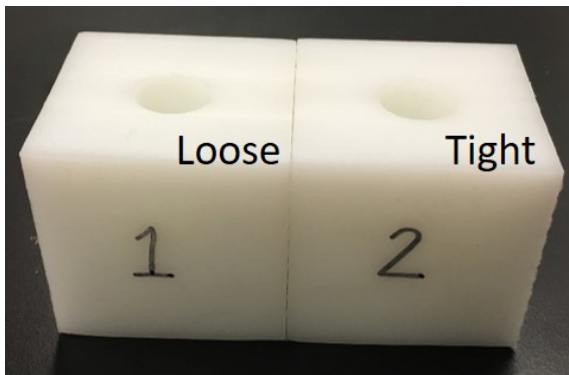
The strategy to be explored in this study is the development of an active sensing strategy that relies on the generation of ultrasonic body waves at the percutaneous tip of an OI prosthesis. The guided waves use the prosthesis as a wave guide to allow the prosthesis-bone interface to be assessed. The sensing strategy aims to assess from reflected waves: 1) the degree of integration at the bone-prosthesis interface; 2) changes in the fixture due to loosening and/or bone damage (*e.g.*, fracture). To explore the potential effectiveness of this sensing strategy, a simplified model is considered. The model consists of a titanium rod with a 15.9 mm diameter and 15.25 cm length implanted in a cubic block (5 by 5 by 5 cm<sup>3</sup>) of high-density polyethylene (HDPE). HDPE is selected because its density ( $\rho = 0.93$  g/cm<sup>3</sup>) and Young's modulus ( $E_{HDPE} = 1$  GPa) are close to that of human bone whose density ranges from 0.15 to 0.80 g/cm<sup>3</sup> and whose modulus ranges from 0.2 to 1.1 GPa<sup>20</sup>.

The Poisson's ratio of the HDPE material is  $\nu_{HDPE} = 0.4$ . The titanium rod has a Young's modulus of  $E_{tit} = 110$  GPa and Poisson's ratio of  $\nu_{tit} = 0.33$ .

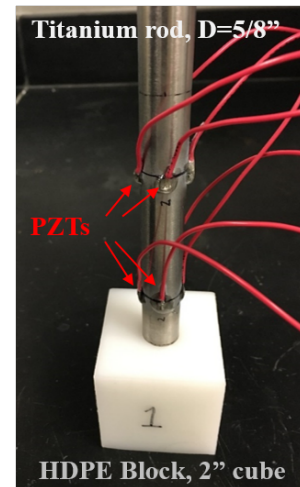
To model different integration states between the titanium rod (acting as a prosthetic fixture) and the HDPE host (acting as host bone), two HDPE blocks are used with different diameter holes machined in its center; hole diameters are 15.87 and 15.90 mm and have the same depth of 5.1 cm. The smaller diameter is intended to ensure that the HDPE provides a greater confining stress on the rod when implanted. Eight piezoelectric elements (4.0 by 4.0 by 0.5 mm<sup>3</sup>) are bonded to the surface of the titanium rod. Four piezoelectric elements are bonded at the quarter points of two different circumferences roughly 51 and 102 mm from the rod percutaneous end. The piezoelectric elements 51 mm from the percutaneous end will serve as actuators to generate body waves in the rod while the piezoelectric elements 102 mm from the percutaneous end will serve as sensors. In this study, the rod will be implanted to different lengths into the HDPE block. Also, PZT and PMN-PT piezoelectric elements will be explored. A picture of the lab set-up is shown in Figure 6.

## NUMERICAL VALIDATION

To assess the properties of the guided waves in the prosthesis and the host bone, a finite element (FE) model was developed in ABAQUS (Dessault Systems). The titanium rod and host HDPE blocks are both modeled using the geometries and material properties of the laboratory set-up. To ensure the accuracy of simulating different guided wave modes in the titanium rod, the FE model was developed with a fine mesh with elements less than one-tenth of the shortest mode wavelength; the time step is also selected to be one-tenth of the central frequency of the excitation signal,<sup>21</sup>



(a)



(b)

Figure 6. (a) Two machined HDPE blocks with varying hole diameters (loose has a 15.9 mm diameter and tight has a 15.77 cm diameter); (b) titanium rod implanted in the loose HDPE block with PZT actuator and sensing arrays shown.



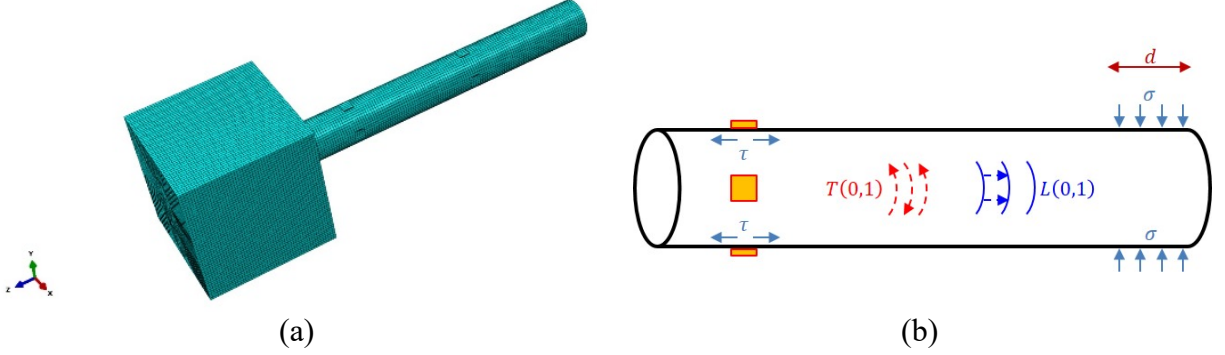


Figure 7. (a) Meshed FE model in ABAQUS; (b) the actuator array on the titanium rod.

$$\begin{aligned} \Delta t &\leq \frac{1}{10f_c} \\ \Delta d_{FE} &\leq \frac{1}{10} \lambda_{min} \end{aligned} \quad (11)$$

where  $\Delta t$  is the time step,  $f_c$  is the central frequency of the excitation signal,  $\Delta d_{FE}$  is the size of the FE model,  $\lambda_{min}$  stands for the shortest wavelength among the  $L(0,1)$ ,  $T(0,1)$  and  $F(1,1)$  modes in the rod. Based on the dispersion curves previously presented in Figure 6, the theoretical group velocities in the rod when a 100 kHz waveform is used as an excitation are 4764.3 m/s for  $L(0,1)$ , 3329.0 m/s for  $T(0,1)$  and 3307.2 m/s for  $F(1,1)$ ; the corresponding wavelengths are  $\lambda_L = 19.9\text{mm}$ ,  $\lambda_T = 16.1\text{mm}$  and  $\lambda_F = 14.4\text{mm}$ , respectively. Thus, the element size of this model is selected to be 1 mm for the rod, and the time step is 0.5  $\mu\text{s}$ , which is appropriate to obtain accurate representation of the wave fields. The HDPE is modeled a little more coarsely. This meshing size resulted in a total of 36,480 elements in the rod, 13,236 in the HDPE, and 48 elements per piezoelectric element. The meshed FE model is shown in Figure 7(a).

For the piezoelectric material, electrical behavior and elastic property are combined into coupled equations as shown in Eq. (12). The piezoelectric material generates a voltage when deformed in strain (*i.e.*, sensing effect) and will strain if an electric field is applied (*i.e.*, actuation effect). The corresponding equations modeling this coupling are

$$\begin{aligned} \{S\} &= [s^E]\{T\} + [d]\{E\} \\ \{D\} &= [d]\{T\} + [\epsilon]\{E\} \end{aligned} \quad (12)$$

where  $\{S\}$  is the strain vector,  $\{T\}$  is stress vector,  $[s^E]$  is the compliance matrix as determined by material elastic properties,  $\{D\}$  is the electric displacement,  $[\epsilon]$  is the material permittivity, and  $\{E\}$  is electric field strength vector, and  $[d]$  is a matrix of piezoelectric constants. Absent the piezoelectric effect,  $\{S\} = [s^E]\{T\}$  would represent the elastic property of the PZT material; however, the strain induced by the piezoelectric effect is reflected by the second term,  $[d]\{E\}$ .

To properly model the PZT elements using Eq. (12), a special C3D8E (8-node, linear) solid piezoelectric element is used in ABAQUS. The rod and HDPE are modeled with classical C3D8R (8-node, linear) solid elements. The element is made from an orthotropic piezoelectric material consisting of the piezoelectric effect matrix  $[d]$ , stiffness matrix  $[C^E]$  (where  $[C^E] = [s^E]^{-1}$ ), and dielectric matrix  $[\epsilon]$ , with matrix terms of  $[d]$  defined by the material properties provided by the piezoelectric manufacturer (Piezo Systems). Two types of piezoelectrics are considered: PZT which is a  $d_{31}$  piezoelectric and PMN-PT which is a  $d_{36}$  piezoelectric. The matrix of piezoelectric coefficients, stiffness matrix  $[C^E]$  and the relative dielectric constant matrix of the  $d_{31}$ -type PZT are:

$$d_{31} = \begin{bmatrix} 0 & 0 & 0 & 0 & 590 & 0 \\ 0 & 0 & 0 & 590 & 0 & 0 \\ -191 & -191 & 430 & 0 & 0 & 0 \end{bmatrix} \times 10^{-12} C/N \quad (13)$$

$$C^E = \begin{bmatrix} 15.2 & 10.2 & 10.0 & 0 & 0 & 0 \\ 10.2 & 15.2 & 10.0 & 0 & 0 & 0 \\ 10.0 & 10.0 & 12.7 & 0 & 0 & 0 \\ 0 & 0 & 0 & 2.1 & 0 & 0 \\ 0 & 0 & 0 & 0 & 2.1 & 0 \\ 0 & 0 & 0 & 0 & 0 & 2.5 \end{bmatrix} \times 10^{10} N/m^2 \quad (14)$$

$$\frac{\epsilon'}{\epsilon_0} = \begin{bmatrix} 1780 & 0 & 0 \\ 0 & 1780 & 0 \\ 0 & 0 & 1950 \end{bmatrix}, \quad \epsilon_0 = 8.854 \times 10^{-12} F/m \quad (15)$$

The matrix of piezoelectric coefficients, stiffness matrix  $[C^E]$  and the relative dielectric constant matrix of the  $d_{36}$ -type piezoelectric wafers are<sup>22-24</sup>:

$$d_{36} = \begin{bmatrix} 0 & 0 & 0 & -1276.8 & 1459.8 & 0 \\ 0 & 0 & 0 & 1459.8 & -1276.8 & 0 \\ -187.8 & -187.8 & 1454.6 & 0 & 0 & -1918.4 \end{bmatrix} \times 10^{-12} C/N \quad (16)$$

$$C^E = \begin{bmatrix} 16.5 & 7.2 & 5.7 & 0 & 0 & -2.2 \\ 7.2 & 16.5 & 5.7 & 0 & 0 & -2.2 \\ 5.7 & 10.0 & 14.7 & 0 & 0 & 4.4 \\ 0 & 0 & 0 & 3.7 & 3.0 & 0 \\ 0 & 0 & 0 & 3.0 & 3.7 & 0 \\ -2.2 & -2.2 & 4.4 & 0 & 0 & 3.4 \end{bmatrix} \times 10^{10} N/m^2 \quad (17)$$

$$\frac{\epsilon'}{\epsilon_0} = \begin{bmatrix} 3856 & -2176 & 0 \\ -2176 & 3856 & 0 \\ 0 & 0 & 5880 \end{bmatrix}, \quad \epsilon_0 = 8.854 \times 10^{-12} F/m \quad (18)$$

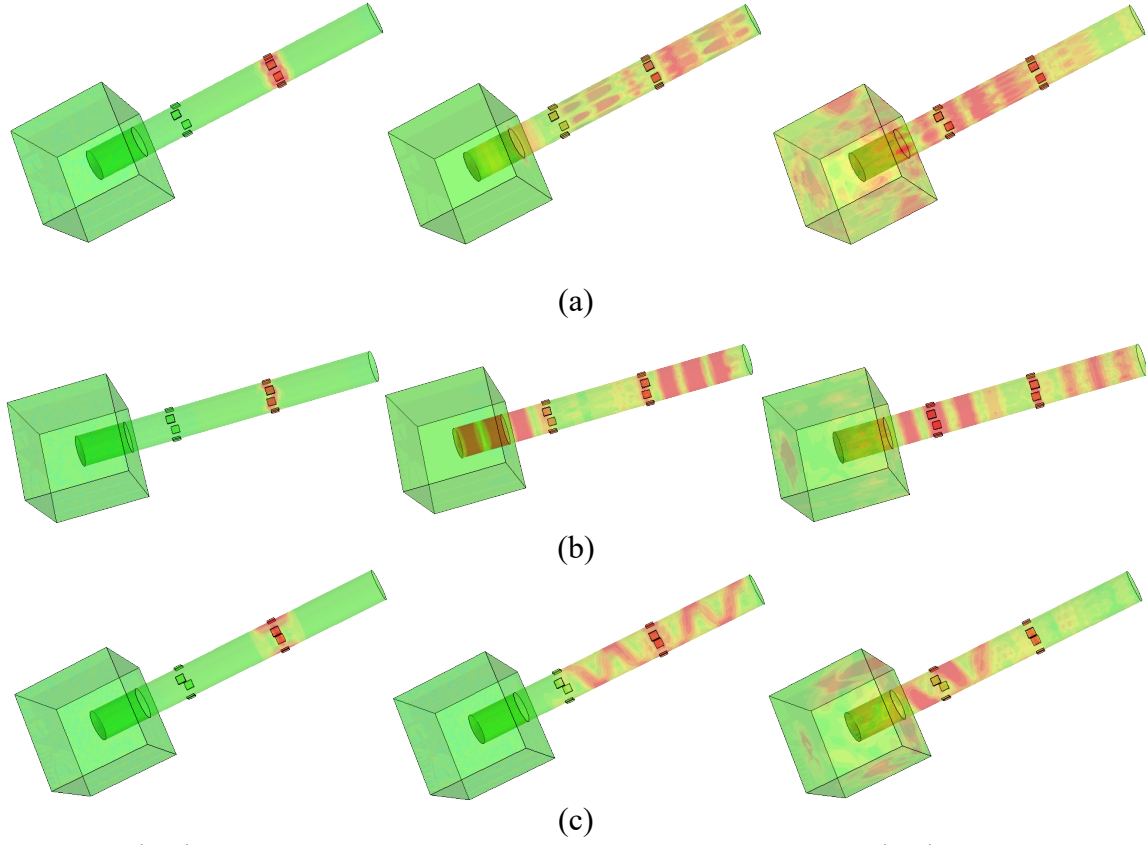


Figure 8. (a)  $L(0,1)$  mode excited by  $d_{31}$  type piezoelectric wafers; (b)  $T(0,1)$  mode excited by  $d_{36}$  type piezoelectric wafers; (c)  $F(1,1)$  mode excited by  $d_{31}$  type piezoelectric wafers with different phases.

The three distinct parts of the model (titanium rod, HDPE block and piezoelectric wafers) are assembled in ABAQUS to model the complete OI prosthesis. The interface between the rod and HDPE block is defined through the use of a friction coefficient; also, various implantation depths of the rod are considered in the model.

Different modes of guided waves can be induced in the rod by controlling the wave forms issued to the piezoelectric array used for actuation purposes. Figure 8(a) shows the generation of the first longitudinal wave in the rod,  $L(0,1)$ , by using PZT actuators with a waveform (three-tone burst centered at 100 kHz) issued with no phase between the elements. The figure reveals the propagation of the wave field with time. When the ultrasonic wave crosses the titanium-HDPE interface, the HDPE block generates its own wave motion which is derived by the guided wave in the rod. Figure 8(b) illustrates the generation of the  $T(0,1)$  mode using the PMN-PT piezoelectric elements which can generate shear waves in the rod. As can be seen, the torsional mode dominates the titanium rod with some of the wave propagating into the HDPE block. Finally, Figure 8(c) shows the  $F(1,1)$  mode introduced by a PZT array with the individual piezoelectric elements actuated out of phase by  $180^\circ$ . In this approach, the  $F(1,1)$  mode is enhanced with the suppression of the  $T(0,1)$  and  $L(0,1)$  modes in the rod.

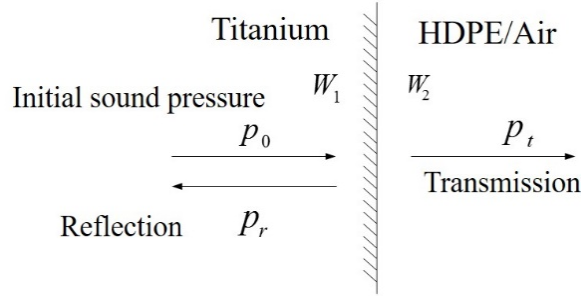


Figure 9. Schematic of the interface between the titanium rod and HDPE block.

## EXPERIMENTAL VALIDATION

Two HDPE block are machined with holes on their top surface 51 mm deep. Block 1 (with the 15.9 mm diameter hole) is “loose” with low confining stress on the rod and Block 2 (with the 15.87 mm diameter hole) is “tight” with high confining stress. Figure 6(b) shows the experimental set-up of the titanium rod implanted in Block 1; the top array containing four PZT elements (Piezo Systems PSI- 5A4E) is the actuator array while the lower four PZT elements (Piezo Systems PSI- 5A4E) constitute the sensing array.

For the detection of the  $L(0,1)$  mode, eight  $d_{31}$  type PZTs are employed to be the actuator (4) and sensor (4) arrays. The induced ultrasonic waves encounter the interface between the titanium rod and HDPE block with a portion of the waves reflected back up the rod and the other waves transmitted into the host block, as shown in Figure 9. The reflection and transmission coefficients are derived as follows,

$$R = \frac{p_r}{p_0} = \frac{W_1 - W_2}{W_1 + W_2} \quad (19)$$

$$T = \frac{p_t}{p_0} = \frac{2W_2}{W_1 + W_2} \quad (20)$$

where  $R$  and  $T$  refer to the reflection and transmission coefficients,  $p_0$  is the initial longitudinal pressure wave,  $p_r$  and  $p_t$  are the reflected and transmitted components of the wave.  $W_1$  and  $W_2$  are the acoustic impedance of the titanium rod and HDPE block, respectively. The acoustic impedance is defined as  $W_i = \rho c_p$ , where  $c_p$  is the velocity of the pressure wave. The density of the titanium is  $\rho = 4540 \text{ kg/m}^3$  with the velocity of the pressure wave as  $c_p = 6,100 \text{ m/s}$ . The density of the HDPE is  $\rho = 965 \text{ kg/m}^3$  with the velocity of pressure wave as  $c_p = 2,000 \text{ m/s}$ . Thus, the reflection coefficient of the titanium-HDPE interface is 0.86 which means 14% of the ultrasonic wave energy is transmitted to the HDPE block resulting in energy loss in the reflected wave.

A three-cycle Hanning window tone burst signal centered at various center frequencies (100 and 200 kHz) is employed as the excitation signal. Figure 10 shows a time history of the reflected waves captured by the sensor array for both the titanium rod by itself and when implanted fully

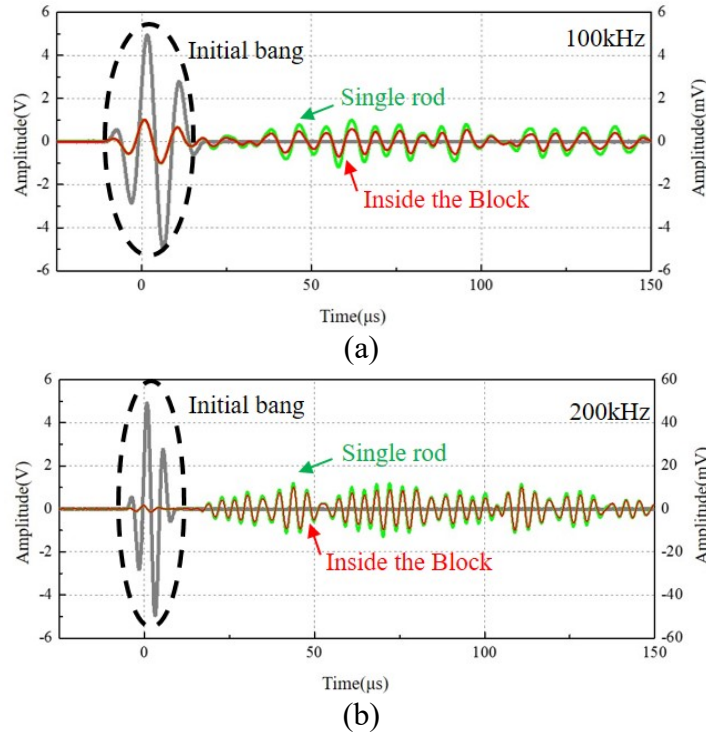


Figure 10. Receive signals with different central frequencies of the excitation signal: (a) 100 kHz; (b) 200 kHz.

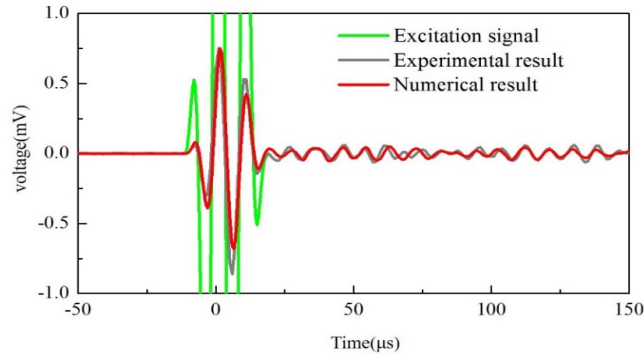


Figure 11. Comparison of the numerical result and experimental signal.

into the HDPE block. As can be seen, the amplitude of the received wave descends as the titanium rod is implanted into the HDPE block regardless of the central frequency of the excitation signal. Figure 11 indicates the numerical results from ABAQUS have good agreement with the experiment.

The study next explored the integration of the rod with the two blocks. A set of tests are conducted of the rod implanted in each block at two depths: 1.27 cm (0.5 in) and 2.54 cm (1 in). Furthermore, waveforms at two center frequencies are applied to each block-penetration depth case to generate longitudinal waves in the titanium rod: 100 kHz and 200 kHz. For each test, the amplitude of the received waveform (after it travels down the rod and reflects back to the sensor array) is measured for each block and penetration depth; the amplitude is plotted for each block-center frequency in

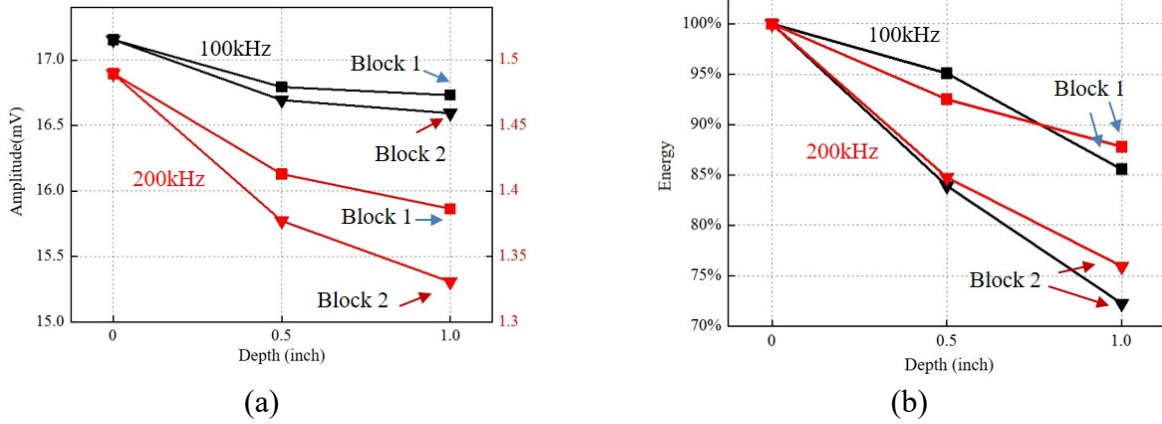


Figure 12. Received signals from the sensing array with different integration degree of the prosthesis and the host bone: (a) amplitude; (b) energy.

Figure 12(a). The energy of the waveform (integration over time of the waveform amplitude squared) is also calculated and plotted in Figure 12(b). Both waveform amplitude and energy prove sensitive to the penetration depth of the rod. Irrespective of the waveform center frequency, the reduction in waveform energy was nearly linear with penetration depth as shown in Figure 12(b). This is expected because a greater penetration depth offers a larger surface area (with area linearly proportional to penetration depth) at the titanium-HDPE interface over which energy is transferred from the rod to the HDPE block. Similarly, the reduction in energy is greater for Block 2 at each penetration depth, irrespective of center frequency of the waveform. This implies the confining stress on the rod permits a greater transfer of energy from the rod to the block.

## OPTIMIZED WAVE GENERATION USING PIEZOELECTRIC ELEMENTS

The previous tests using HDPE as a bone surrogate validate that guided wave energy will be adsorbed at the interface between bone and the prosthesis fixture. This means osseointegration occurring at a bone-prosthesis interface could be potentially monitored using guided waves. The measured energy in the wave signal propagating along the fixture will be directly dependent on the interface between the prosthesis fixture and the bone. Hence, changes in the bone-prosthesis interface such as bone attachment and growth into the porous surface of the prosthesis (*i.e.*, osseointegration) will increase the absorbed wave energy at the interface. In this study, the energy content of guided wave modes is considered as a quantitative basis of assessing the mechanical properties of the prosthesis-bone interface.

Ideally, the wave mode introduced in the prosthesis wave guide should be easy to excite with piezoelectric wafer elements mounted on the fixture surface. Furthermore, it should have a high signal-to-noise ratio (SNR) for accurate wave acquisition using piezoelectric wafer elements mounted on the fixture surface. The fundamental longitudinal mode ( $L(0, 1)$ ) selectively excited

in the low frequency spectrum (lower than the cutoff frequency for the second flexural mode) is proposed because at low frequencies the fundamental longitudinal mode dominates, thereby simplifying the wave field and reducing coherent noise from higher modes. While flexural and torsional modes can exist at these lower frequency bands (as shown in the dispersion curve of a titanium rod in Figure 4), the piezoelectric actuation strategy will ensure longitudinal modes are selectively generated. To generate the desired fundamental longitudinal wave field, a  $d_{31}$ -type piezoelectric wafer array (namely PZT ceramic wafers) will be installed on the circumference of the prosthesis rod with all elements of the array excited by the same electrical signal. Each piezoelectric element is defined by length,  $l$ , width,  $w$ , and thickness  $y$  (Figure 3). Four elements are proposed to be mounted to the quarter points of the circumference of the prosthesis fixture to serve as actuator and sensor arrays that generate and sense the longitudinal wave, respectively. The piezoelectric wafer dimensions and signal frequency must be optimized to ensure guided wave modes have large strain fields; this ensures a high SNR for the waves measured in the prosthesis. This is especially important when considering the fact the guided wave amplitudes will attenuate in time so a high SNR ensures a detectable signal for a more precise assessment of guided wave energy. This section details the optimization of the piezoelectric geometry to maximize SNR.

The compatibility established between a piezoelectric wafer and host structure is achieved through interfacial shear stress  $\tau(z, t)$ <sup>25</sup>. In the case of ideal bonding (no shear lag across the piezoelectric wafer-structure interface), the shear stress induced in the structure can be modeled using the simplified pin-force model where the shear exists only at the wafer boundaries<sup>21</sup>. Thus, the shear stress along the longitudinal axis that is induced by the piezoelectric wafer,  $\tau(z, t)$ , in harmonic excitation can be expressed as,

$$\tau(z, t) = a\tau_0[\delta(z - a) - \delta(z + a)]e^{i\omega t} \quad (21)$$

where  $a$  is the half-length of the piezoelectric wafer,  $a\tau_0$  is the pin force magnitude applied at the end of the piezoelectric wafer,  $\delta(\cdot)$  is Dirac function in space (in this case, applied at the ends of the  $2a$  long wafer),  $\omega$  is the excitation frequency, and  $t$  is time. Here, the harmonic component is generalized to  $e^{i\omega t}$  but later only the real component of the solution will be of interest.

Similar to Lamb wave tuning in thin plates by Giurgiutiu<sup>21</sup>, this study tunes the piezoelectric size to maximize the amplitudes of the strain fields associated with the fundamental longitudinal wave in a solid titanium rod with a 15.9 mm diameter. To simplify the analysis, it is performed in the wavenumber ( $\xi$ ) domain by applying the Fourier transform to functions defined in the space ( $z$ ) domain:

$$\tilde{g}(\xi) = \int_{-\infty}^{\infty} g(z)e^{-i\xi z} dz \quad (22)$$

The expressions for the scalar and vector fields (equations (1) and (2)), the assumed form of the field components (equations (3) to (6)), the displacement fields (equations (7) to (9)) and stress fields can be transformed to the wavenumber domain using equation (22).

This section deals with the theoretical solution of PZT tuning mechanism when longitudinal guided waves are introduced in a solid cylindrical rod with ideal bonding of PZT elements. The space domain Fourier transform is used to resolve the problem using complex integrals<sup>21</sup>. The excitation signal in the wavenumber domain via the Fourier transform (equation (22)) is expressed as:

$$\begin{aligned}\tilde{\tau}_a(\xi) &= \int_{-\infty}^{\infty} a\tau_0[\delta(z-a) - \delta(z+a)]e^{-i\xi z} dz \\ &= (-2i \sin \xi a)a\tau_0\end{aligned}\tag{23}$$

Applying the space domain Fourier transform to equations (1) through (9), the general solution of equations (1) and (2) in the wavenumber domain is of the form:

$$\tilde{\Phi} = \tilde{\varphi}(r, z) \cdot \cos n\theta e^{-i\omega t} = \tilde{A}J_n(\alpha r)\cos n\theta e^{-i\omega t}\tag{24}$$

$$\tilde{H}_r = \tilde{\psi}_r(r, z) \cdot \sin n\theta e^{-i\omega t} = \tilde{B}J_{n+1}(\beta r)\sin n\theta e^{-i\omega t}\tag{25}$$

$$\tilde{H}_\theta = \tilde{\psi}_\theta(r, z) \cdot \cos n\theta e^{-i\omega t} = -\tilde{B}J_{n+1}(\beta r)\cos n\theta e^{-i\omega t}\tag{26}$$

$$\tilde{H}_z = \tilde{\psi}_z(r, z) \cdot \sin n\theta e^{-i\omega t} = \tilde{C}J_{n+1}(\beta r)\sin n\theta e^{-i\omega t}\tag{27}$$

Thus, the displacements and stress in wavenumber domain can be expressed as:

$$\tilde{u}_z = \left[ i\xi \tilde{\varphi} - \frac{d\tilde{\psi}_r}{dr} - \frac{n+1}{r} \tilde{\psi}_r \right] \cos n\theta e^{-i\omega t}\tag{28}$$

$$\tilde{\sigma}_{rr} = \left\{ -\lambda(\alpha^2 + \xi^2)\tilde{\varphi} + 2\mu \left[ \frac{d^2\tilde{\varphi}}{dr^2} + \frac{n}{r} \left( \frac{d\tilde{\psi}_z}{dr} - \frac{\tilde{\psi}_z}{r} \right) + i\xi \frac{d\tilde{\psi}_r}{dr} \right] \right\} \cos n\theta e^{-i\omega t}\tag{29}$$

$$\tilde{\sigma}_{r\theta} = \mu \left\{ -\frac{2n}{r} \left( \frac{d\tilde{\varphi}}{dr} - \frac{\tilde{\varphi}}{r} \right) - \left( 2 \frac{d^2\tilde{\psi}_z}{dr^2} - \beta^2 \tilde{\psi}_z \right) - i\xi \left( \frac{n+1}{r} \tilde{\psi}_r - \frac{d\tilde{\psi}_r}{dr} \right) \right\} \sin n\theta e^{-i\omega t}\tag{30}$$

$$\tilde{\sigma}_{rz} = \mu \left\{ 2i\xi \frac{d\tilde{\varphi}}{dr} - \frac{n}{r} \left[ \frac{d\tilde{\psi}_r}{dr} + \left( \frac{n+1}{r} - \beta^2 + \xi^2 \right) \tilde{\psi}_r \right] + \frac{i\xi n}{r} \tilde{\psi}_z \right\} \cos n\theta e^{-i\omega t}\tag{31}$$

For the fundamental longitudinal mode  $n = 0$ , a new boundary condition is applied to reflect the harmonic wave generation at the piezoelectric surface where  $r = R$ . Specifically, for the



fundamental longitudinal mode ( $n = 0$ ) the boundary conditions in the wavenumber domain at the piezoelectric wafer can be specified as,

$$\tilde{\sigma}_{rr}|_{r=R} = \tilde{\sigma}_{r\theta}|_{r=R} = 0 \quad (32)$$

$$\tilde{\sigma}_{rz}|_{r=R} = \tilde{\tau}_a = (-2i \sin \xi a) a \tau_0 e^{i\omega t}$$

where  $\tilde{\sigma}_{rz}|_{r=R}$  is essentially the pin-force shear model transformed to the wavenumber domain. Consider the equation (29) to (31) with the boundary condition equation (32) as a system of linear equation involving with variables of  $\tilde{A}$ ,  $\tilde{B}$  and  $\tilde{C}$ , thus, applying the Cramer's rule, the solution of the system of three linear equations yields:

$$\tilde{A} = \frac{L_A}{D_0} \tilde{\tau}_a \quad (33)$$

$$\tilde{B} = \frac{L_B}{D_0} \tilde{\tau}_a \quad (34)$$

$$\tilde{C} = 0 \quad (35)$$

where

$$L_A = 2i\xi\mu\beta J_1'(\beta R) \left( \mu\beta^2 J_0(\beta R) + \frac{2\mu\beta}{R} J_0'(\beta R) \right) \quad (36)$$

$$L_B = \left( \frac{\lambda(\alpha^2 + \xi^2) + 2\mu}{\alpha^2} J_0(\alpha R) - \frac{2\mu}{\alpha^2 R} J_0'(\alpha R) \right) \left( \mu\beta^2 J_0(\beta R) + \frac{2\mu\beta}{R} J_0'(\beta R) \right) \quad (37)$$

$$D_0 = \begin{vmatrix} -\frac{\lambda(\alpha^2 + \xi^2) + 2\mu}{\alpha^2} J_0(\alpha R) + \frac{2\mu}{\alpha^2 R} J_0'(\alpha R) & 2i\xi\mu\beta J_1'(\beta R) & 0 \\ 0 & i\xi\mu \left[ \beta J_1'(\beta R) - \frac{1}{R} J_1(\beta R) \right] & \mu\beta^2 J_0(\beta R) + \frac{2\mu\beta}{R} J_0'(\beta R) \\ -2\mu i\xi\alpha J_0'(\alpha R) & (\beta^2 - \xi^2)\mu J_1(\beta R) & 0 \end{vmatrix} \quad (38)$$

Thus, applying the inverse Fourier transform and recurrence relationship associated with first order Bessel functions:  $x \frac{d}{dx} J_n'(x) + n J_n(x) = x J_{n-1}(x)$  to equation (28) yields the displacement in the physical domain:

$$\begin{aligned}
u_z(z, \theta, t)|_{r=R} &= \frac{1}{2\pi} \int_{-\infty}^{\infty} \left[ i\xi \tilde{\varphi} - \frac{d\tilde{\psi}_r}{dr} - \frac{1}{r} \tilde{\psi}_r \right] \cos n\theta e^{-i\omega t} e^{i\xi z} d\xi \\
&= \frac{1}{2\pi} \int_{-\infty}^{\infty} \left( i\xi \frac{L_A}{D_0} J_0(\alpha R) - \frac{L_B}{D_0} \beta J_0(\beta R) \right) \tilde{\tau}_a \cos n\theta e^{-i\omega t} e^{i\xi z} d\xi
\end{aligned} \tag{39}$$

The integrant in equation (39) is singular at the roots of  $D_0 = 0$ , which is exactly the frequency equation for the longitudinal wave. The evaluation of the integral in equation (39) can be done by the residue theorem, which yields the integral by the sum of the residues:

$$u_z(z, \theta, t)|_{r=R} = 2a\tau_0 \left( \sum_{\xi^L} i\xi^L \frac{L_A(\xi^L)}{D_0(\xi^L)} J_0(\alpha R) - \sum_{\xi^L} \frac{L_B(\xi^L)}{D_0(\xi^L)} \beta J_0(\beta R) \right) \sin \xi^L a e^{i(\xi^L z - \omega t)} \tag{40}$$

Thus, the solution for the  $z$ -component of the wave field displacement, as defined in the wavenumber domain, is:

$$\tilde{u}_z = \frac{\partial \tilde{\Phi}}{\partial z} + \frac{1}{r} \frac{\partial}{\partial \theta} (r \tilde{H}_\theta) - \frac{1}{r} \frac{\partial \tilde{H}_r}{\partial \theta} \tag{41}$$

where  $\tilde{\Phi}$ ,  $\tilde{H}_r$ ,  $\tilde{H}_\theta$ , and  $\tilde{H}_z$  are the components of the scalar and vector fields in equations (3) to (6) in the wavenumber domain via the Fourier transform (equation (22)). The displacement in the physical domain can be obtained by applying the residue theorem in the evaluation of the integral of the inverse Fourier transform via the sum of residues

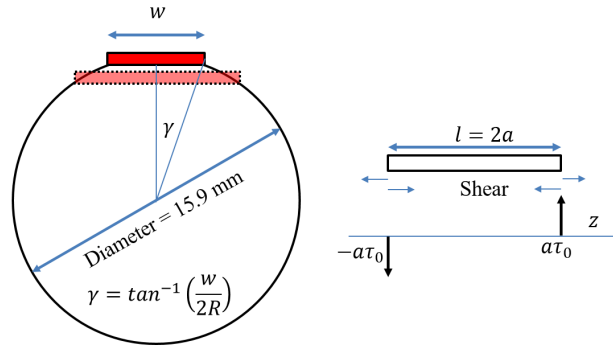
$$u_z(z, \theta, t)|_{r=R} = 2a\tau_0 \left( \sum_{\xi^L} i\xi^L \frac{L_A(\xi^L)}{D_0(\xi^L)} J_0(\alpha R) - \sum_{\xi^L} \frac{L_B(\xi^L)}{D_0(\xi^L)} \beta J_0(\beta R) \right) \sin \xi^L a e^{i(\xi^L z - \omega t)} \tag{42}$$

Here  $L_A$ ,  $L_B$ , and  $D_0$  are functions that depend on the excitation signal frequency and piezoelectric wafer dimensions. Similar solution can be obtained for the fundamental torsional mode and flexural mode.

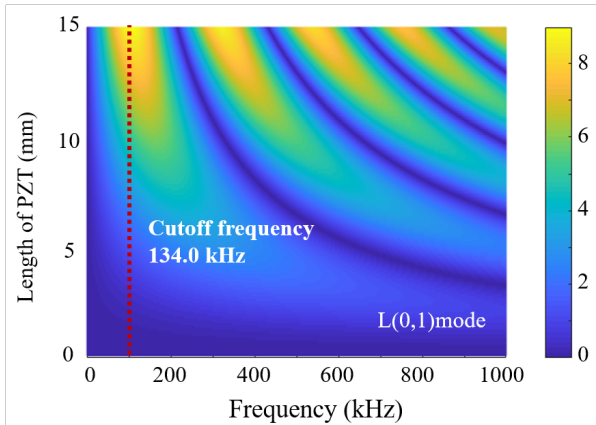
In summary, equation (42) indicates the guided wave modes can be tuned in the rod via  $\sin \xi^L a$ . The maximum displacement magnitude occurs when  $\xi^L a = (2n - 1)\pi/2$  resulting in  $\sin \xi^L a = 1$ ; consequently, a wave mode will not be excited when  $\xi^L a = n\pi$ . The guided wave mode tuning principles derived here for an active piezoelectric transducer apply equally well for a receiver (sensing) piezoelectric transducer. Thus, the amplitude of the induced wave mode will change with both the central frequency of the excitation signal that induces the wavelengths of the wave field and the length of the piezoelectric wafer<sup>21</sup>.

The 15.9 mm diameter titanium rod is now considered with rectangular PZT piezoelectric transducers bounded to the rod circumference. The PZT wafers are assumed to be 0.508 mm thick based on the piezoelectric wafers used later during experimental validation (hence,  $y = 0.508$  mm). The rod is machined to offer a perfectly flat rectangular surface prior to bonding. This approach to preparing the rod for the piezoelectric wafers will control the width,  $w$ , of the wafer. To machine no deeper than 5% of the radius,  $R$ , the wafer width,  $w$ , is selected to satisfy the function  $\gamma = \tan^{-1}(w/2R) < 18.2^\circ$  (see Figure 13(a)). Hence, for the 15.9 mm diameter rod, this results in a maximum width of 4.95 mm. In this study, the width is selected to be  $w = 4$  mm.

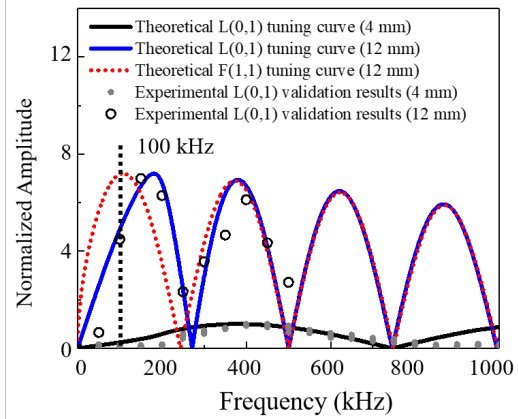
The tuning process to maximize the longitudinal wave field displacement described previously is used to select the wafer length,  $l$ . Figure 13(b) plots the absolute value of  $\sin \xi^L a$  as a function of wave frequency and element wafer length,  $l=2a$ , to allow an appropriate length wafer to be selected. The relationship between the longitudinal wave wavenumber,  $\xi$ , and frequency,  $\omega$  is simply  $\omega^L = \xi^L c_{ph}^L$ , where  $c_{ph}^L$  is the phase velocity of the longitudinal mode.



(a)



(b)



(c)

Figure 13. Optimization of the piezoelectric wafer length: (a) schematic of the piezoelectric wafer dimensions and the simplified pin-force model, (b) tuning curve ( $\sin \xi^L a$ ) of the  $L(0,1)$  mode, and (c) validated tuning curves.

Two lengths of the PZT wafer are considered in this study: 4 mm and 12 mm. Considering Figure 13(b), the normalized maximum surface displacement (equation (42)) is plotted for each wafer size considered. While the previous tuning procedure considered only the fundamental longitudinal mode, similar tuning equations for the first flexural mode can also be derived. In the tuning process described herein, flexural modes are considered in addition to longitudinal modes to leave open the possibility of using flexural modes for osseointegration assessment in future studies. The same tuning curves are plotted in Figure 13(c) for the flexural modes. There is a stark difference in the normalized amplitudes between 12 mm and 4 mm with the 12 mm long wafer offering a much larger amplitude for both the first longitudinal and flexural modes; hence, 12 mm wafers will be elected in this study.

Next, the excitation frequency of the PZT wafer is considered. For the 15.9 mm diameter titanium rod, the cutoff frequencies of the flexural, longitudinal and torsional modes are 134.0 kHz, 231.6 kHz, and 345.6 kHz, respectively. To suppress higher order wave modes, the excitation frequency should be set to below 134.0 kHz. Based on the tuning curve of Figure 13(c), an excitation frequency of 100 kHz is selected because it provides nearly equal benefit to the longitudinal and flexural modes.

## SUMMARY

This section explored the use of an OI prosthesis as a wave guide for detection of the integration of the prosthesis at the bone-prosthesis interface. The monitoring strategy consists of launching guided waves from the percutaneous tip of the prosthesis using piezoelectric elements. Fundamental longitudinal waves are introduced into the prosthesis rod to interrogate the prosthesis-bone interface. Changes in the waveform reflected along the waveguide can be used to quantify the degree of integration at the bone. To assess the feasibility of this strategy, a series of tests are conducted on a titanium rod implanted in HDPE blocks. The tests reveal sensitivity of the reflected waveform in the titanium rod as a function of both penetration depth and confining stress offered by the block. An important contribution of the study is the theory of tuning guided waves in solid cylindrical rods with ideal bonding of a PZT wafer. The optimization of the length of the PZT and the excitation frequency are achieved based on the tuned curve of longitudinal waves will be used to enhance the accuracy of the proposed *ex vivo* monitoring technique.

## SECTION 3: *EX VIVO* MONITORING TO ASSESS HEALING IN OSSEOINTEGRATED PROSTHESES USING GUIDED WAVES

### INTRODUCTION

The previous section established the theory of guided waves in solid rod geometries and optimized the size of piezoelectric elements for high SNR measurement of guided waves generated in OI prostheses. In this section, the functionality of the *ex vivo* sensing strategy will be validated in the laboratory on prosthetic models consisting of titanium femoral stems implanted in synthetic sawbones. The degree of osseointegration is an essential parameter for clinical decision making (*e.g.*, when can an OI prosthesis be loaded?) during the post-operative healing processes. Thus, fundamental longitudinal waves are introduced into the prosthesis rod to interrogate the prosthesis-bone interface in this section. Similar to the previous section, numerical simulation and experimental validation will be performed.

### OSSEOINTEGRATED PROSTHESIS-BONE MODEL

A synthetic bone model is adopted in this study to explore how osseointegration at the bone-prosthesis interface affects the fundamental longitudinal wave mode in a prosthesis fixture. A synthetic femur bone (Figure 14(a)) is acquired from Sawbones Worldwide (Model 3406-5) to serve as a host to a titanium rod serving as a prosthesis fixture. The femoral sawbone is manufactured from a solid rigid polyurethane foam material (with a density of  $1600 \text{ kg/m}^3$ ). Sawbones are a popular alternative to human cadaver bone for biomechanics research given the degree of mechanical realism the synthetic bone provides. To ensure realism in the experimental study, the density of the synthetic sawbone was selected to ensure the bone has an acoustic

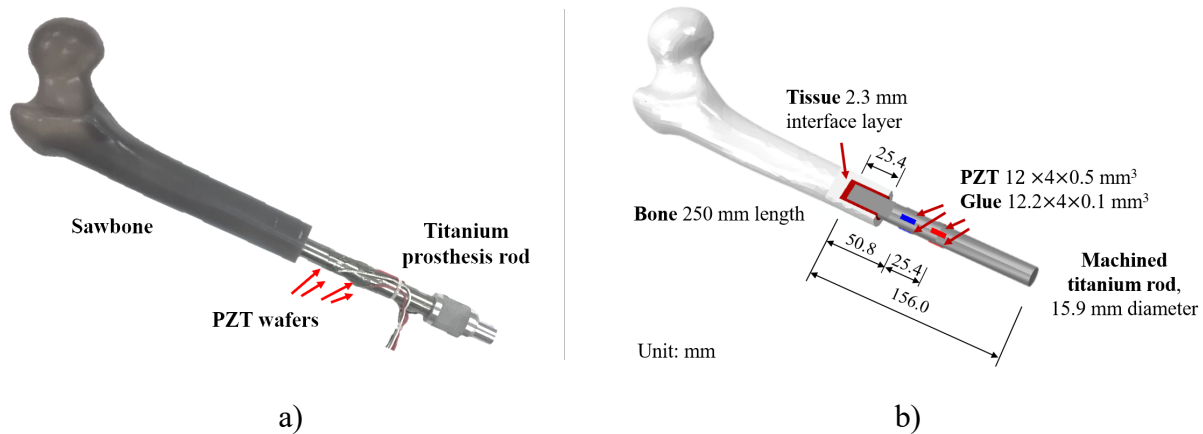


Figure 14. Osseointegrated prosthesis-bone model: (a) picture of femur sawbone with titanium prosthesis rod; (b) titanium rod in host bone model (dimensions are in mm).

impedance ( $5.66 \times 10^6 \text{ kg/m}^2 \text{ s}$ ) similar to that of human femoral bones ( $6 \times 10^6 \text{ kg/m}^2 \text{ s}$ )<sup>26-28</sup>. The bone is cut in half to have an approximate length of 25 cm and its interior is reamed to provide a snug fit for a 15.9 mm diameter titanium rod (similar to that used in the HDPE study presented in the previous section) implanted to a depth of 2.54 cm.

A solid isotropic (Grade 5) titanium rod with a diameter of 15.9 mm and length of 15.60 cm is selected as the prosthesis fixture and machined to allow 8 PZT wafers (Piezo Systems PSI- 5A4E) to be attached. The PZT wafers are 0.508 mm thick and cut from larger wafers to be 12 mm long and 4 mm wide (based on the optimization described previously in Section 2). Piezoelectric sensors are placed on the side of the rod instead of at its end because the end of the prosthesis will have a complex joint with an artificial limb attached. Placement on the side also allows for potential replacement of the PZT wafers with time and offers opportunity to generate different wave modes (longitudinal, torsional, and flexural modes) in the prosthesis<sup>29</sup>. The rod is machined to provide perfectly flat surfaces 12.2 mm long and 4 mm wide at the quarter points of the rod circumference at two circumference locations. The two circumferential arrays are centered 76.2 mm and 50.8 mm from the rod's percutaneous end. The PZT wafers are bonded to the rod surface using standard cyanoacrylate glue. The rod with PZT elements bonded can be implanted into the sawbone to the full machined depth (2.54 cm) as shown in Figure 14(a). To excite the longitudinal wave mode in the rod, the first array of PZT elements is excited with a three cycle tone-burst waveform whose center frequency is 100 kHz. By exciting all four elements of the PZT array at the same time and in phase, only the longitudinal wave mode will be generated. The second array of PZT elements will be used to measure the time history of the longitudinal wave propagating along the fixture.

## **NUMERICAL OSSEOINTEGRATED PROSTHESIS-BONE MODEL**

A finite element model is first created to numerically simulate the waves generated in the prosthesis and the mechanical interaction between the bone and the prosthesis fixture during wave propagation in the prosthesis. The finite element (FE) modeling platform ABAQUS (Dessault Systems) is adopted to model the femur sawbone-titanium rod osseointegration model.

To accurately model the complex three-dimensional (3D) geometry of the femur, laser scanning and photogrammetry is utilized to acquire a precise digital mapping of the femur surface geometry (Figure 15). The NextEngine 3D scanner is used to capture the femur sawbone surface using lasers generating 3D point clouds and cameras mapping RGB values to the surface topology points. Using an automated turn table, a full 360° scan of the femur is conducted. The turning table rotates to 10 positions (poses) and 4 laser beams are used to scan the surface topology at each pose. The laser scanner provides a comprehensive point cloud with a density of 150 sample points per inch. NextEngine Studio is used to align the point clouds generated by the various poses to generate 1635 curved surfaces that constitute the surface geometry of the entire femur. The curved surfaces are then merged to form one complete solid model using Creo 4.0. The meshed solid model of the femur is then imported to ABAQUS for analysis.

The ABAQUS model (Figure 14(b)) is divided into five geometric parts: bone, titanium rod, PZT element, bone tissue at the prosthesis surface, and bond layer between the PZT and prosthesis. The

use of numerical platforms such as ABAQUS (or any other FE package) to model wave mechanics requires an appropriate selection of mesh size and time increment. Both are highly dependent on the frequency and wavelength of the wave modes. First, the time step size must be sufficient to accurately capture the propagating waveform with enough samples to unambiguously represent the waves. In effect, this means the sampling frequency must exceed, at a minimum, two times the highest wave frequency of interest but standard practice is to sample five or more times the highest frequency of interest. Second, the element size (spatial domain) must be small enough to accurately capture the wavelength of the wave field. In general, the element size must be a small fraction of the smallest wavelengths anticipated<sup>30, 31</sup>.

The titanium rod is isotropic and modeled with mechanical properties as follows: elastic modulus  $E_{tit} = 110$  GPa, density  $\rho_{tit} = 4330$  kg/m<sup>3</sup>, and Poisson's ratio  $\nu_{tit} = 0.30$ <sup>32</sup>. The rod is meshed in ABAQUS using C3D20R (20-node, quadratic brick) solid elements. For the guided wave in the rod, using a 100-kHz excitation signal, the wavelengths of the first longitudinal, torsional, and flexural modes are calculated as  $\lambda_L = 47.64$ mm,  $\lambda_T = 32.3$ mm and  $\lambda_F = 33.1$ mm, respectively. The feature size of the solid element is selected to be 1 mm resulting in more than 30 nodes per wavelength and a total of 36,480 elements for the titanium rod.

The femur bone is meshed using a 10-node, quadratic tetrahedron element (C3D10) with a feature size of 4 mm resulting in a total of 31,846 solid elements. The density of the bone is 2000 kg/m<sup>3</sup>. The anisotropic material properties in Table 1 are used for the femur bone with orientation defined

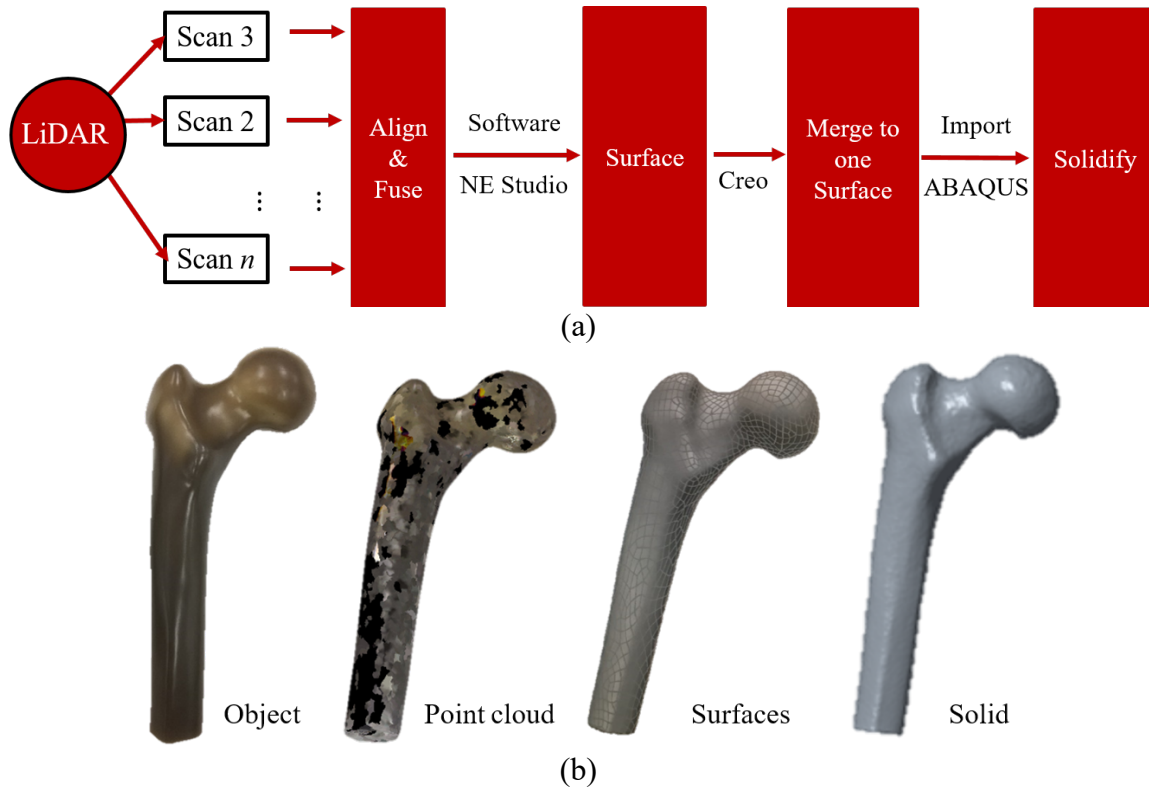


Figure 15. Laser scanning of femur: (a) 3D laser scanning process and (b) the progression of the actual femur object into a solid model for analysis

in the cylindrical coordinate system<sup>33, 34</sup>. It is noted that the values in Table 1 are modified values of density, elastic modulus and Poisson's ratio of the bone based on model updating using experimental results, instead of the initial range provided by the manufacturers and previous studies<sup>33, 34</sup>. A cavity is created in ABAQUS to define the interior surface of the femur. A varying element size strategy is taken for the femur bone to reduce computational cost.

The 20-node, quadratic piezoelectric brick elements (C3D20RE) are used for the PZT elements which are  $12 \times 4 \text{ mm}^2$  in area and 0.504 mm thick. The density of PZT is  $7500 \text{ kg/m}^3$ . The piezoelectric properties are obtained from the piezoelectric manufacturer (Piezo Systems) and imported in ABAQUS format (Table 2 and 3). The grid in length and width is 1 mm with 4 elements in the thickness direction for the PZT wafer, which results in 192 elements per PZT element. The bottom surface (at the rod surface) of each PZT element is grounded with 0 V electric potential, and the top surface is excited by a surface charge related to the excitation signal.

The bond layer is modeled as a 0.1 mm thickness cyanoacrylate glue layer between the PZT and prosthesis. The size of the bond layer is  $12.2 \times 4 \times 0.1 \text{ mm}^3$  with the density of  $1250 \text{ kg/m}^3$  and the elastic modulus of 3.5 GPa. The C3D20R (20-node, quadratic brick) solid element is used to mesh the bond layer. Constraint type "tie" is created between the PZT bottom surface (master surface) and the bond layer's top surface (slave surface). Similarly, another tie constraint pair is created between the bond bottom layer (master surface) and the surface of the titanium rod (slave surface) to transfer the force from the PZT element to the surface of the prosthesis.

A total of 6095 quadratic tetrahedron elements (C3D10) are employed to model the interfacial bone tissue existing between the prosthetic implant and the femoral bone. The material properties of this layer are based on femur bone properties, while all are set as variables to simulate osseointegration. The bone surface tissue is selected to be a 2.3 mm layer tied to both the titanium rod and the bone's cylinder cavity as constraints. The thickness of this connective bone layer is based on the minimum bone cover needed for OPRA implants (2 mm)<sup>35</sup>. The constraint pairs are the titanium to tissue's internal surface (master to slave surface pair, respectively) and the tissue's outer surface to bone's internal cavity (master to slave surface pair, respectively).

Three-cycle tone burst signals with center frequencies of 100 kHz are applied simultaneously to the four PZT actuators on the same circumference. The time step in the ABAQUS/Implicit is chosen as  $0.2 \text{ } \mu\text{s}$  based on the previous discussion. The numerical model has been validated and updated based on experimental results, which will be presented in the next section.

Table 1. Material properties of the femur\*

Young's Modulus (GPa)	Shear Modulus (GPa)	Poisson's ratios
$E_1 = 16.0$	$G_{12} = 3.3$	$\nu_{12} = 0.30$
$E_2 = 6.8$	$G_{23} = 3.6$	$\nu_{12} = 0.45$
$E_3 = 6.8$	$G_{13} = 3.3$	$\nu_{12} = 0.30$

\* 1-direction is longitudinal to femur main axis; 2- and 3-directions are orthogonal to longitudinal axis<sup>33, 34</sup>



Table 2. PZT elastic stiffness constants,  $C_{ij}^E (10^{10} \text{ N/m}^2)$

Material	$C_{11}^E$	$C_{12}^E$	$C_{13}^E$	$C_{33}^E$	$C_{44}^E$	$C_{66}^E$
PSI-5A4E	15.2	10.2	10.0	12.7	2.1	2.5

Table 3. PZT piezoelectric coefficient,  $d_{ij} (10^{-12} \text{ C/N}^2)$ , and dielectric constant,  $\epsilon_{ij} (10^{-8} \text{ F/m})$

Material	$d_{31}$	$d_{33}$	$d_{15}$	$\epsilon_{11}$	$\epsilon_{22}$	$\epsilon_{33}$
PSI-5A4E	-191	430	590	1576	1576	1727

## NUMERICAL SIMULATION OF TITANIUM ROD IN HOST BONE

A key element of the numerical model is the ability to assess changes in the longitudinal mode energy content as osseointegration occurs. A model of osseointegration associated with healing bone is established based on experimental data provided by Manjubala *et al.*<sup>36</sup>. Their study provides a detailed model of adult bone properties during healing including increases in bone density ( $\rho$ ) and elastic modulus ( $E$ ). Their study also reveals the random nature of bone changes over a surface as healing occurs.

To investigate the effects of interfacial tissue on the acoustic impedance signature of the longitudinal wave mode in the prosthesis, the spatial distribution of changes in the bone elastic modulus and density is simulated by a program (macro) written in Python for ABAQUS. The script randomly selects elements to form 10 groups with elements in each group having specific elastic modulus and density values. The average elastic modulus and density of the bone tissue is ranged from 1 kPa and 1 kg/m<sup>3</sup> (approximately 0% healing) to 16.0 GPa and 2000 kg/m<sup>3</sup> (i.e., 100% of the bone modulus and density under mature osseointegration) with increments of 3.2 GPa and 400 kg/m<sup>3</sup> (i.e., 20%). The elastic modulus and density of each group is defined as the average elastic modulus and density multiplied by a scaling factor. The scaling factor ranges from 0.98 to 1.02 with a unique scaling factor assigned to each group. Full osseointegration is defined as when the

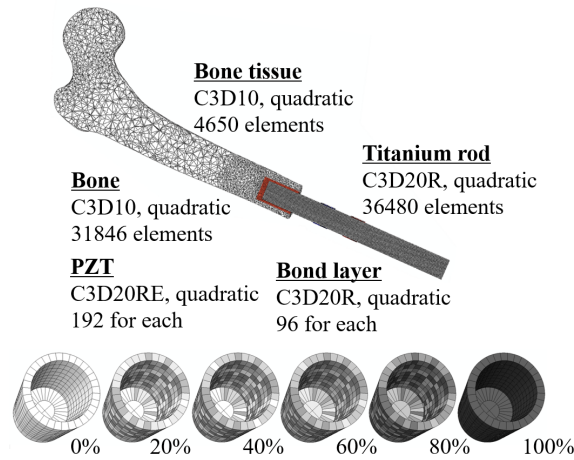


Figure 16. Numerical model and osseointegrated bone tissue

average elastic modulus and density of the bone surface tissue reach the mature femur bone properties in Table 1. Thus, the degree of osseointegration of each stage is on average 0%, 20%, 40%, 60%, 80% and 100%  $\pm 2\%$  integrated (as shown in Figure 16).

The osseointegration model is simulated by ABAQUS/Implicit. The fundamental longitudinal mode ( $L(0, 1)$ ) of guided waves propagating in the titanium rod is received by the sensor array and transferred to the electric potential waveform as shown in Figure 17(a). The energy of the waveform  $E_s$  is calculated according to,

$$E_s = \sum_{i=1}^N |s_i|^2 \quad (43)$$

where,  $s_i$  is the amplitude of the signal and  $N$  is the number of the sampled points in the acquired signal (in this study,  $N=500$ , which means the first 100  $\mu s$  of the waveform will be taken into

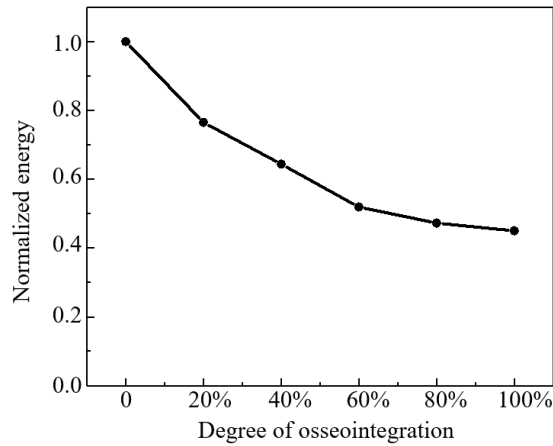
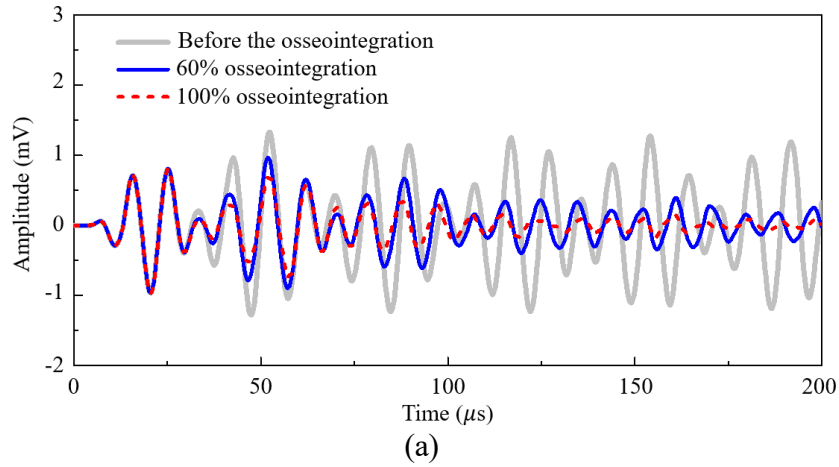


Figure 17. Numerical model and results of the osseointegration: (a) waveforms received by the sensor on the titanium rod and (b) the energy of waveform with various degree of osseointegration.

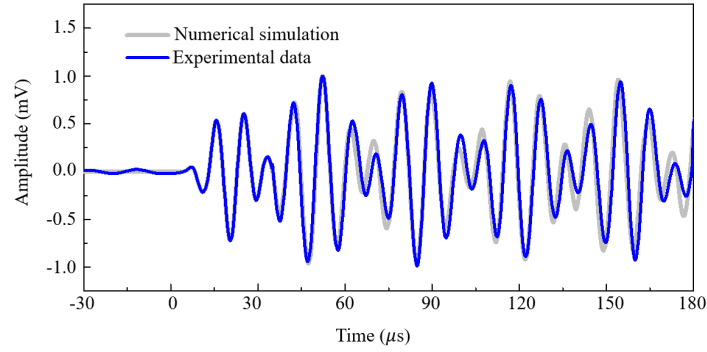
account). Figure 17(b) presents that the energy of the first 100  $\mu\text{s}$  waveform which changes with the degree of osseointegration of the bone tissue under interrogation using the longitudinal guided wave mode. The numerical results establish a clear trend that the amplitude and the energy of  $L(0, 1)$  wave in the prosthesis rod decreases with the degree of bone tissue osseointegration. Both the waveforms and the decreasing energy trend will be validated by experimental testing in the laboratory in the next section.

## EXPERIMENTAL VALIDATION

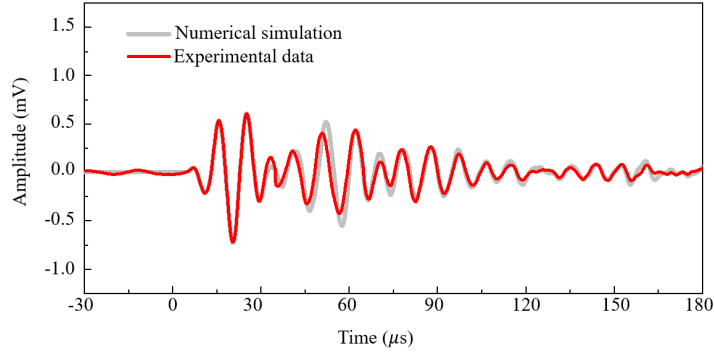
As described in the former section, the titanium rod (with PZT elements pre-attached) is implanted in a sawbone to mimic the OI prosthesis in an adult femur. A National Instruments (NI) 8101 chassis with PXIe-6124 and PXIe-6361 data acquisition cards (DACs) installed is employed to be the target controller to execute the wave generation and wave sensing process. Two DACs offer 4 output channels and 4 input channels for the actuators and sensors, respectively, with a maximum sampling frequency 1 MHz. The entire data acquisition process was driven by a user interface coded in LabVIEW. A PC with LabVIEW is utilized to be the master controller carrying out all of the commands, saving experimental data, and analyzing the waveforms obtained from laboratory experiments. All captured waveforms are transferred from the NI chassis to the remote PC in real-time. A user-friendly interface is created in LabVIEW to visualize and analyze changes in the wave energy correlated to both the degree of integration and the looseness of the prosthesis in the bone.

For the experimental validation of osseointegration in a femur bone, a 30-minute epoxy with a fully cured density of  $1550 \text{ kg/m}^3$  and elastic modulus of 3.5 GPa is applied to the bone-prosthesis interface to mimic the post-operative healing process; specifically the epoxy, like osseointegrating bone, experiences increasing elastic modulus and density. Repeated  $L(0, 1)$  mode guided waves are generated and converted to a scalar metric through the signal energy using equation (43). While the cured density is nearly identical to the sawbone density, the epoxy modulus is slightly greater than half that of bone, but in this case, the epoxy curing is only intended to show sensitivity. Clearly, had the epoxy cured to have a modulus closer to that of bone, the change in acoustic impedance would be even more dramatic making the change in signal energy more pronounced.

After defining the rod geometry and locations of the PZT elements in ABAQUS, the density, elastic modulus, and the Poisson's ratio of the titanium rod and the femur sawbone (which are the most important acoustic medium parameters) are selected as the parameters to update in the model. Model updating is performed to achieve a good fit between the experimental and simulation waveforms<sup>37</sup>. The density and elastic modulus describe the absolute value of acoustic impedance of the bone and rod, which result in the change of wave amplitude<sup>16, 17</sup>. Additionally, the elastic modulus and the Poisson's ratio are adjusted to reconcile the waveform with physical measurements including crest, trough, and phase. It is noted that all the material properties shown in the previous section (Table 1) are updated values based on the experimental results. It is noted that, the signal amplitude or energy is a continuous function of the density and elastic modulus of the bone tissue. Thus, the comparisons of the numerical and experimental results for 0% and 100% degree of osseointegration are sufficient for model updating. After model updating, the waveform captured by the sensor before the osseointegration experiment has good agreement with the 0%

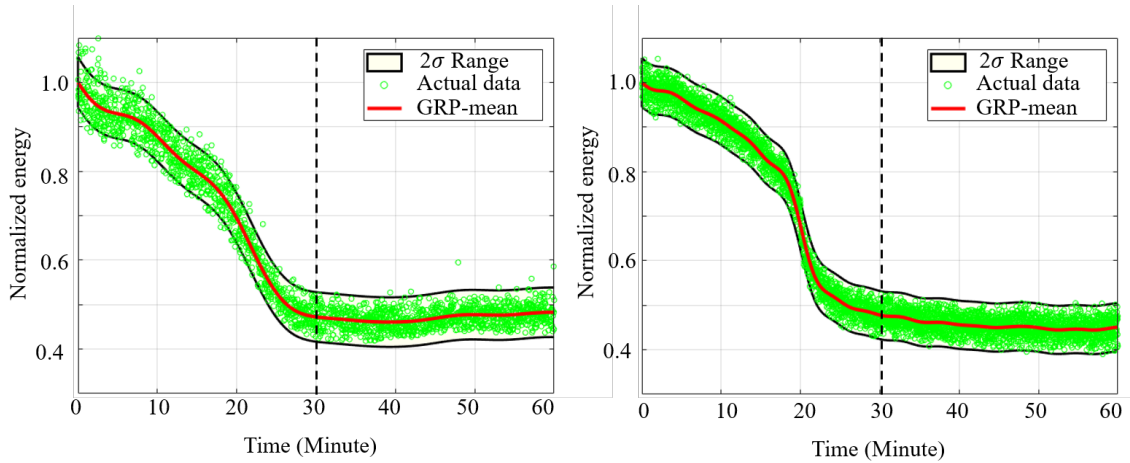


(a)



(b)

Figure 18. Comparison of numerically and experimentally derived waveforms: (a) before osseointegration (0%) and (b) after full osseointegration (100%)



(a)

(b)

Figure 19. GPR of signal energy versus curing time: (a) sample 1 and (b) sample 2.

degree of osseointegration simulated by ABAQUS as demonstrated in Figure 18(a). Meanwhile, the simulated waveform with 100% osseointegration of the bone tissue is nicely fitted into the measurement when the epoxy is fully solidified after 30 minutes (Figure 18 (b)). The change in wave energy as a function of time in the experimentally tested sawbone is shown in Figure 19.

The wave energy absorbed by the bone as osseointegration occurs (modeled by the curing epoxy) increases with time.

Gaussian processes regression (GPR)<sup>38, 39</sup> is used to analyze the relationship between the energy of the longitudinal wave mode and the degree of osseointegration. The purpose of GPR is to model a relationship between wave energy and osseointegration based on the experimental results. Two tests are carried out with a GPR model fit to each experimental result as shown in Figure 19(a) and (b). The energy of the received wave decreases with the osseointegration in the first 30 minutes. After the epoxy solidifies, the energy reaches a stable stage representing the healthy state of the OI prosthesis. The general standard deviation values in the experiments range from 1.76 to 1.79% of the normalized energy. It is also worth mentioning that the two GPR models are very similar underscoring the repeatability of the approach.

Next, considering the fact that 5 to 7% of implants have to be removed because of loosening of the prosthesis, fixture loosening and pullout is experimentally modeled for long-term monitoring research<sup>35, 40</sup>. Figure 20 shows the experimental set-up of penetration depth (*i.e.*, pullout) testing. The femur sawbone is clamped on a rigid structure. Clay is employed to simulate the interfacial tissue between the prosthesis and the bone. The prosthesis fixture is slowly pulled out of the bone using an actuator. Towards this end, the prosthetic titanium rod is connected to a horizontal turn screw motor (Figure 20). The motor is loaded in a quasi-static fashion with increasing displacement controlled by LabVIEW. Two linear variable displacement transducers (LVDTs) and one load cell are employed to monitor both the displacement and force of the pullout maneuver.

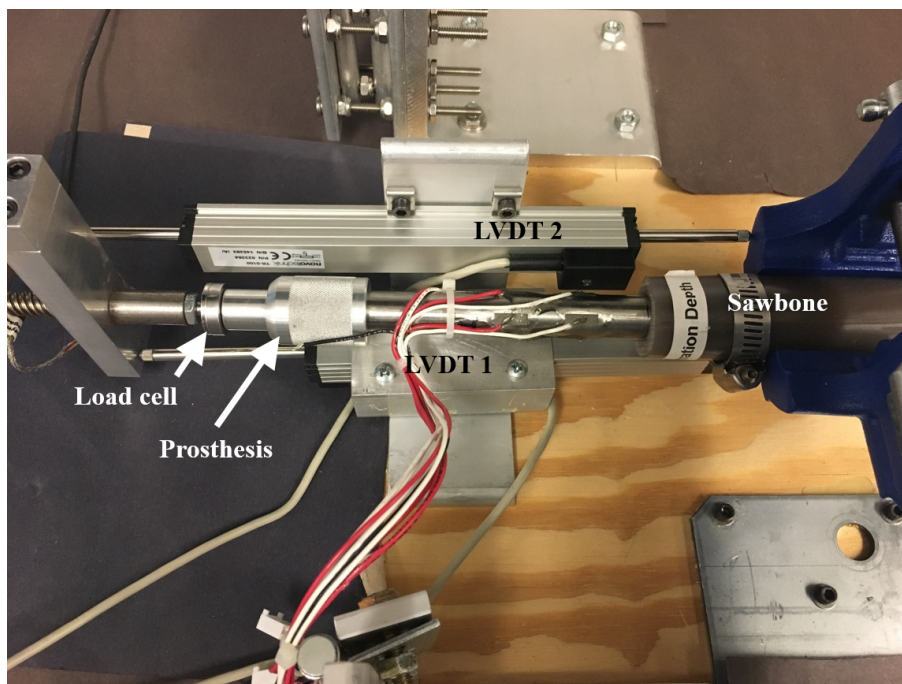


Figure 20. Experimental set-up with two LVDTs and one load cell.

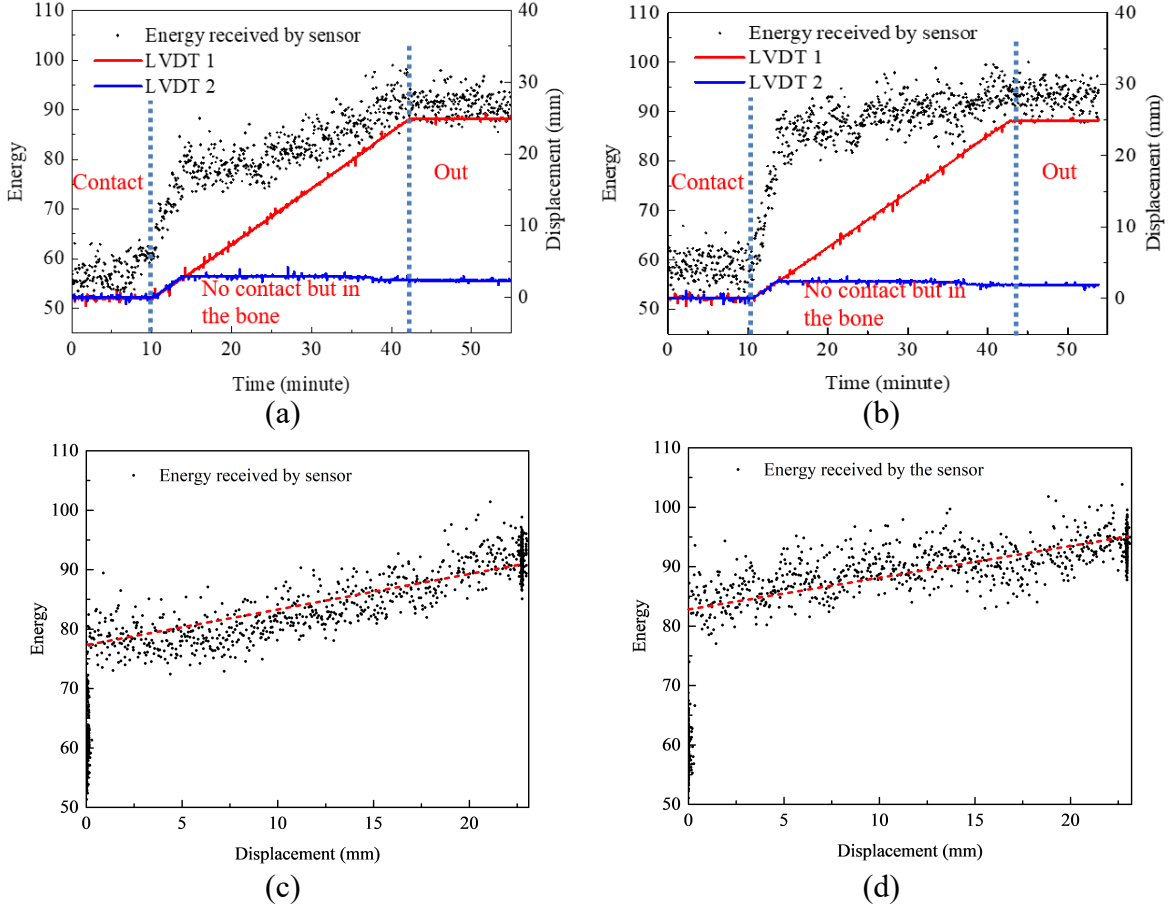


Figure 21. Pull-out experimental results: (a) sample 1; (b) sample 2; (c) sample 1 stage 2 and (d) sample 2 stage 2.

Figure 21 shows the energy of the longitudinal guided waves received by the sensor array as a function of the pull-out displacement. Two stages are observed. First the pullout force begins to relax the pressure the rod applies to the bone at the flat circular surface of the rod when fully seated in the bone. This stage continues until the pressure on the bone at this surface vanishes. Next is the second stage where the rod is now moving out of the bone effectively sliding along the bone's inner cavity. Two LVDTs are used to measure the displacement of the rod to the actuator and the bone relative to the actuator. To ease the readability of the experimental results, the energy is demonstrated in two separated ranges. In the first stage, the wave energy significantly increases at the beginning of the separation of the rod and bone, thereby relaxing pressure on the contact surface of the rod. After the initial detachment, the energy slowly increases due to the pullout, which changes with the penetration depth. Figures 21(a) and 21(b) plot energy (along with displacement) for samples 1 and 2, respectively. Figure 21(c) and 21(d) show the same results just plotting stage 2. The software used to run the experiment can identify both the penetration depth and the contact status by the interrogation of the fundamental longitudinal guided wave. These results verify the sensitivity of guided wave energy to detect loosening and the pulling out of an OI prosthesis fixture.

## SUMMARY

In this section, guided waves are proposed as a tool to predict the degree of osseointegration of bone-prosthesis implants after surgery for clinical decision making (*e.g.*, when can an osseointegrated prosthesis be loaded?). This active sensing strategy is conducted from outside the limb on the percutaneous extension of the prostheses and utilizes piezoelectric wafers to introduce guided wave into the prosthesis fixture. Reflected guided (longitudinal) waves are employed to assess the degree of osseointegration and loosening of the prosthesis based on a scalar energy parameter.

The sensing strategy is first numerically simulated to estimate the degree of osseointegration after surgical placement. 3D laser scanning is utilized to provide a precise digital mapping of the femur sawbone geometry for a numerical model in ABAQUS. Osseointegration is mimicked by increasing the elastic modulus and density of the bone tissue at the prosthesis surface. The energy of received guided waves decreases with the healing processing as is validated by the numerical model. Full osseointegration results in approximately a 50% change in longitudinal wave energy. To verify the sensitivity of the longitudinal wave model on changes in an interface between the prosthesis and bone, experimental results were conducted with epoxy serving as a surrogate for bone healing. Again, results confirmed energy of the wave mode sensitive to changes in the interface. In addition, the separation of the prosthesis from the bone was also studied via pull-out experiments whose results show the wave energy has a significant increase with the pullout. Hence, the proposed strategy is sensitive and selective to both osseointegration and prosthesis loosening. These results demonstrate the great potential of guided waves for clinical evaluation of the bone-prosthesis interface. The use of longitudinal wave mode energy as a metric for evaluation has the advantage of sensitivity to osseointegration and pullout. During the process of osseointegration signal energy monotonically decreases; during loosening and fixture pullout the energy increases. In the next section, the use of guided waves to detect fracture will be explored. To do so, a new wave mode will be adopted: the flexural wave mode.



## SECTION 4: DETECTION OF BONE FRACTURE IN OSSEOINTEGRATED PROSTHESES USING FLEXURAL MODES

### INTRODUCTION

In this section, the case of bone fracture is considered. The guided wave monitoring strategy of the OI prosthesis is tailored to detect fracture in the host bone. Bone fractures can occur when the OI prosthesis is overloaded. In order to detect and localize the occurrence of a fracture in the bone securing the OI prosthesis fixture, flexural guided waves are explored. Flexural waves can be generated in the wave guide by exciting piezoelectric wafers bonded to the surface of the fixture out of phase. To advance this flexural wave sensing strategy, the previously used finite element model consisting of the titanium rod (with PZT elements mounted) implanted in a femoral bone is used. This section also presents a flexible LabView user interface for users that wish to use guided waves for clinical evaluation of OI prostheses.

### FLEXURAL MODE EXCITATION

Again, a titanium rod with a diameter of 15.9 mm and length of 15.60 cm is considered as the prosthesis fixture. As before, attached to the fixture are eight  $12 \times 4 \text{ mm}^2$  PZT wafer organized in two circumferential arrays (four serving as sensors on one circumference and the other four serving as actuators). The fixture is implanted into a synthetic sawbone to mimic the OI prosthesis. The meshed femoral bone-prosthesis FE model of the previous section is used again to study flexural waves; the model is shown in Figure 22(a). To mimic the bone fracture, a longitudinal crack is set on the bone model by cutting its geometry. The size of the longitudinal crack is 25.4 mm (length)  $\times$  0.2 mm (thickness), which is a through-all cut crack near sensor 1 with the crack surface is parallel to y-axis defined in Figure 22(b).

A three-cycle Hanning window tone-burst signal centered at 100 kHz is employed as the excitation signal for the PZT actuator elements. The  $F(1, 1)$  mode of a guided wave is employed to monitor

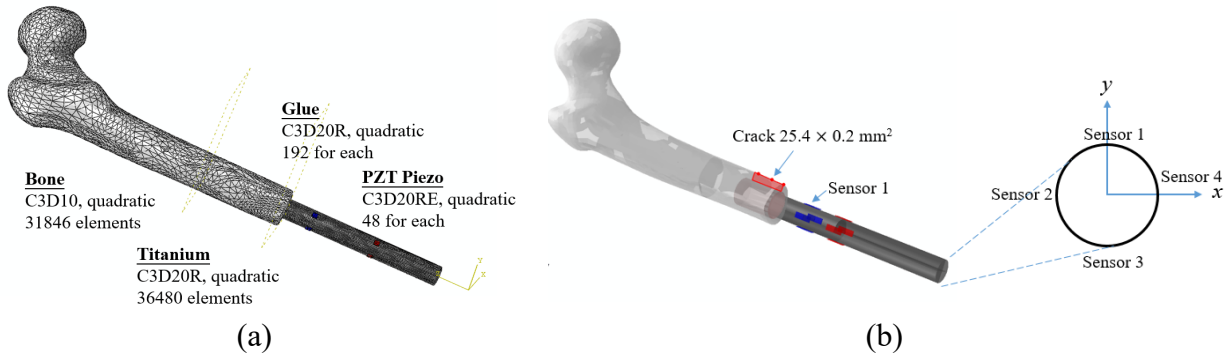


Figure 22. Numerical model in ABAQUS: (a) meshed titanium prosthesis implanted into the bone; (b) schematic of the crack and sensor locations



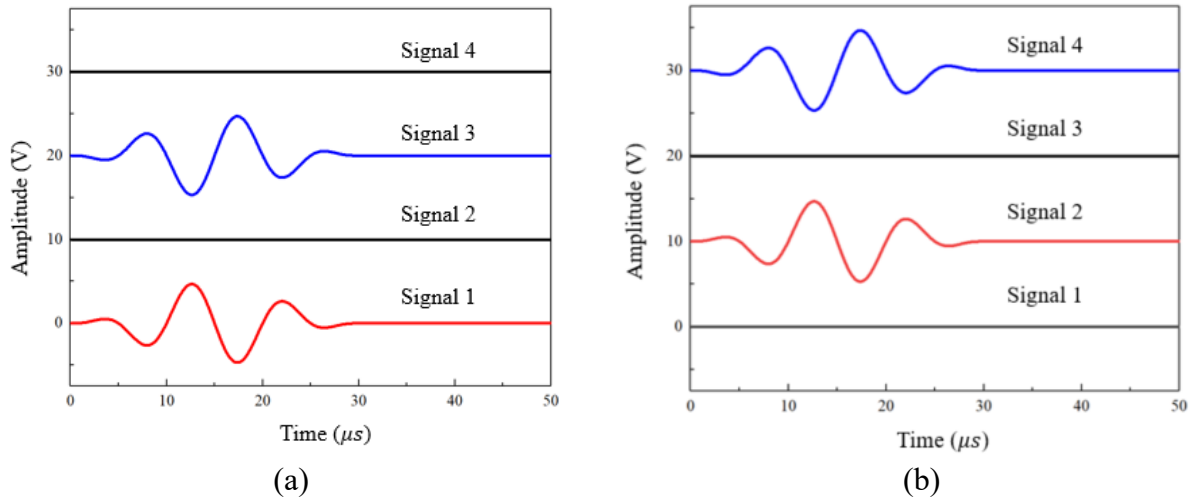


Figure 23. Excitation signals for  $F(1, 1)$  mode of Rayleigh wave: (a) 1-3 direction; (b) 2-4 direction.

the fracture of the host bone. To introduce the desired directional flexural Rayleigh wave, only 2 PZT elements are excited by the excitation signals with the excitation voltage applied out of phase between the two PZT wafers. Two different directions  $F(1, 1)$  mode Rayleigh waves are introduced into the prosthesis rod: one is launched by the actuator pair 1 and 3 (Figure 22(b)) which propagates mainly within the plane defined by the y-axis; the other is launched by actuator pair 2 and 4 propagating mainly within the plane defined by the x-axis. The three-cycle 100 kHz tone burst signals applied to the PZT to generate the different flexural guided waves are represented in Figure 23. To simulate the displacement waveforms in time, a dynamic ABAQUS/Standard implicit simulation is performed over a 200  $\mu\text{s}$  simulation period. The strain field of the entire model (in the titanium rod and bone), the displacement of the titanium rod (25.4 mm and 152.4 mm from the rod's percutaneous end), and electrical potential of the PZT elements is simulated

## NUMERICAL VALIDATION

Figures 24(a) and 24(c) show snapshots of the strain fields in the pristine OI prosthesis system under flexural waves in the 1-3 direction (y-plane) and 2-4 direction (x-plane) at the time  $t=30 \mu\text{s}$ , and  $100 \mu\text{s}$ , respectively. Figure 24(e) and 24(f) show that the maximum circumferential displacement of the prosthetic titanium rod surface under the excitation signal represented in Figures 23(a) and 23(b), which are the excitation to generate directional flexural wave modes.

The visualization results provided by the FE model reveal that the guided waves propagate along the longitudinal axis of the prosthesis fixture to interrogate the properties of the bone-prosthesis interface as desired. It can be clearly seen that the strain of the circumferential surface significantly increases from  $0^\circ$  to  $90^\circ$  and then decreases again in the next  $90^\circ$ , which indicates the desired directional flexural mode are induced by the out-of-phase excitation signals in Figure 23.

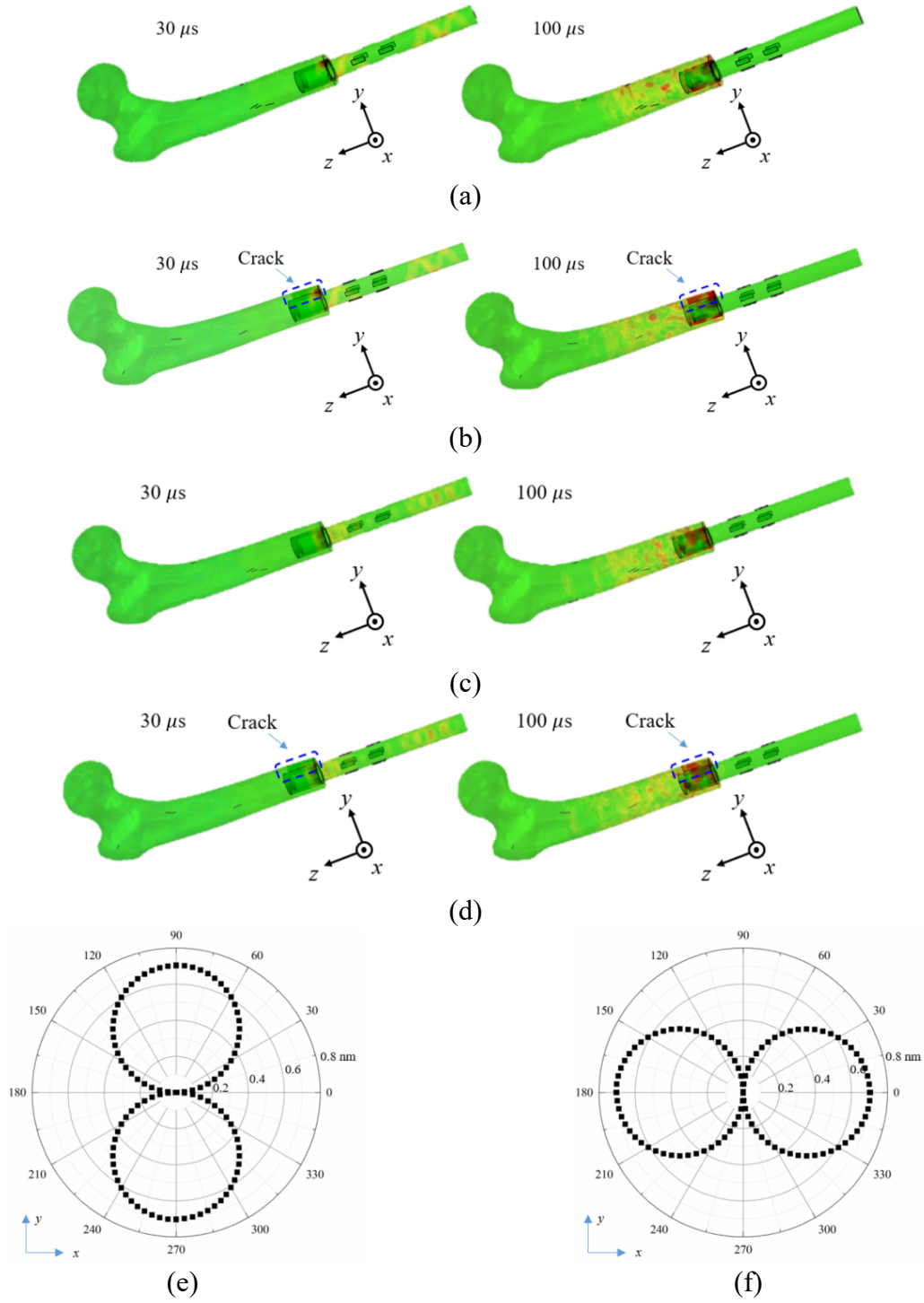
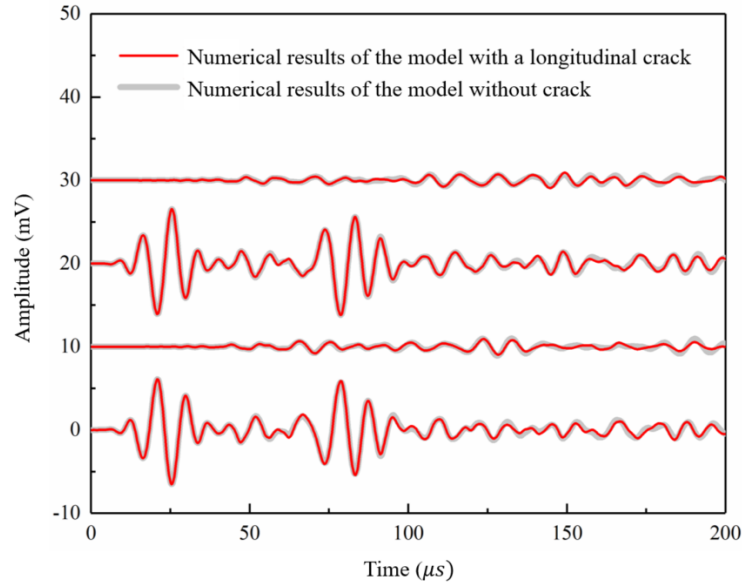
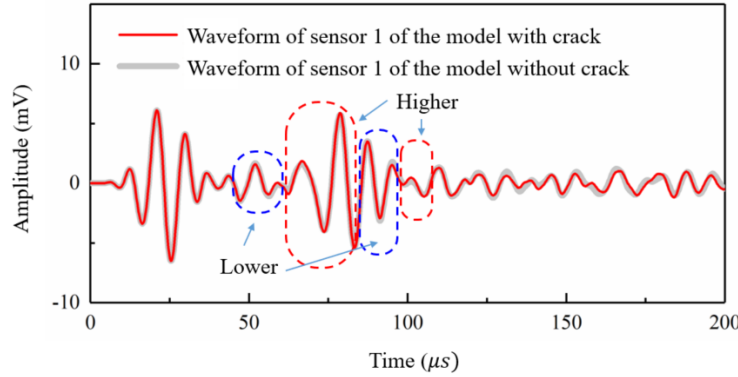


Figure 24. Numerical (strain) results for  $F(1,1)$  wave at 30 and 100  $\mu\text{s}$ : (a) flexural waves in a healthy bone-prosthesis model excited by actuator pair 1 and 3; (b) flexural waves in a bone-prosthesis model excited by actuator 1 and 3 with a longitudinal crack; (c) flexural waves in a healthy bone-prosthesis model excited by actuator pair 2 and 4; (d) flexural waves in a bone-prosthesis model excited by actuator 2 and 4 with a longitudinal crack; circumferential maximum displacements excited by (e) actuator 1 and 3, and (f) actuator 2 and 4.



(a)



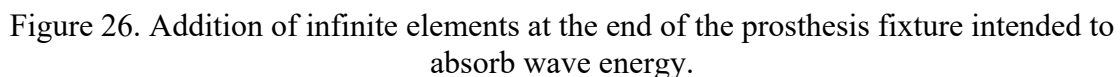
(b)

Figure 25. Comparison of the waveforms with/without the crack in the bone-prosthesis FE model: (a) waveforms of all sensors; (b) waveform of sensor 1.

With bone fracture present, Figure 24(b) and (d) demonstrate the strain fields associated with the flexural wave scattering from the bone fracture in the FE model at the time  $t=30 \mu s$  and  $100 \mu s$ , respectively. The strain field is changed by the bone fracture. Figure 25 overlays the received PZT signal for the two cases: healthy bone and bone with fracture. Some differences are observable on the time history responses measured. Figure 25(b) highlights the signal received in sensor 1 when the flexural wave is contained in the x-plane (as excited by actuator pair 2 and 4). The differences in the simulated waveforms can be due to the fracture site clapping thereby introducing new wave packets into the signals recorded. This observation is consistent with Huygens' principle which stipulates the crack would serve as a new wave source producing a wave package after the flexural wave propagates to its location and excites it. Hence, extracting the difference signal from the healthy baseline case to the case with fracture is a clear approach to identifying the bone fracture.

With the crack distorting the waveforms propagating along the prosthesis fixture, a time-of-flight (ToF) analysis is done to better investigate the influence of the crack. To perform an analysis on the waveform reflected from the bone-end of the prosthesis, a non-reflective fixture end (at the percutaneous end) is created in ABAQUS. An infinite element is used to create a non-reflective boundary in ABAQUS. As shown in Figure 26 the right end of the titanium rod contains 240 infinite elements whose nodes are counterclockwise. Once the waveform is generated by the piezoelectric array, the flexural wave packet propagates along the titanium rod with a velocity of 3308.3 m/s. Upon arrival at the crack, the crack is excited and acts as a new wave source superimposing its wave onto the original waveform. Figure 27 indicates the ToF of the wave packet. The red line is the waveform captured in the damaged bone, and the gray one is the guided wave propagating in the healthy bone (the dotted line is the excitation signal itself).

For the 1-3 direction (y-plane) excitation indicated in Figure 23(a), the arrival time of the wave at sensors one through four are 56.8  $\mu\text{s}$ , 126.0  $\mu\text{s}$ , 95.8  $\mu\text{s}$ , and 148.8  $\mu\text{s}$ , respectively. For the 2-4 direction (x-plane) flexural wave indicated in Figure 23(b), the arrival time at sensors one through four are 165.2  $\mu\text{s}$ , 102.8  $\mu\text{s}$ , 102.8  $\mu\text{s}$ , and 84.6  $\mu\text{s}$ , respectively. Considering the fact that the difference signals are due to the wave excitation at the crack, the arrival times obtained by the two different flexural mode wave are related to both the location of bone fracture and the excitation. The smallest arrival time reveals the crack location, which is the bone-prosthesis interface closest to sensor 1. In addition, the amplitude of the first wave packet is higher when the prosthetic rod is excited by the 1-3 direction flexural mode, which verifies the location of the crack is closest to



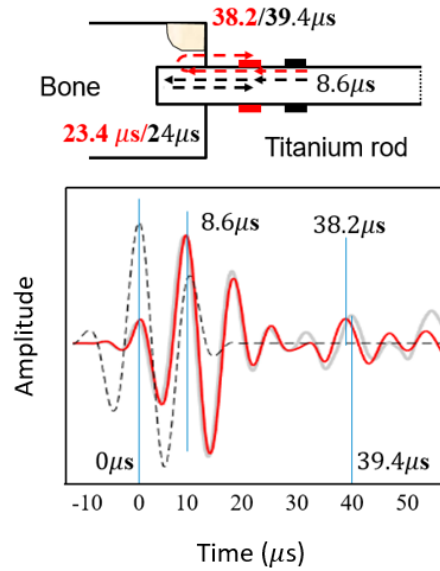


Figure 27. Time-of-flight of the guided wave and the interaction caused by bone fracture.

sensor 1. It is noted that the energy of difference signal excited by the 2-4 direction flexural mode is higher than the energy excited by the 1-3 direction wave after about  $75 \mu s$ . This fact is because the crack direction is parallel to the y- plane, which reflects more energy to the prosthetic rod when the wave begins to propagate in the bone. These results offer a preliminary approach to detecting bone fracture using guided waves in the prosthesis.

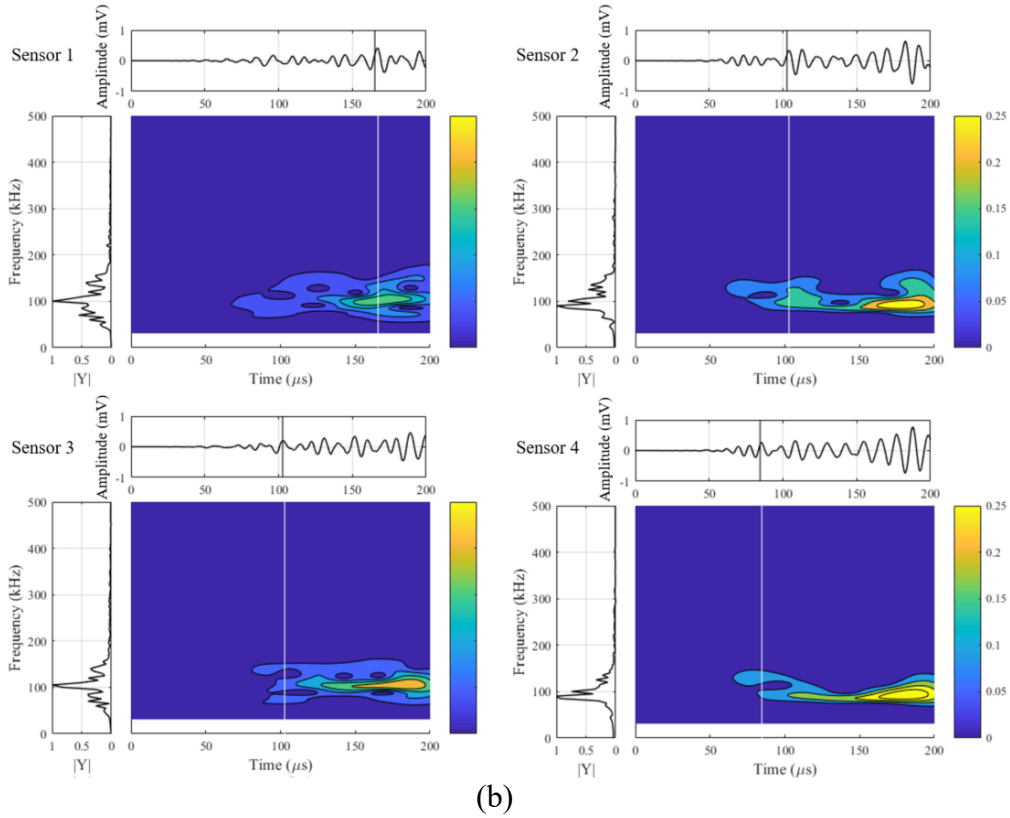
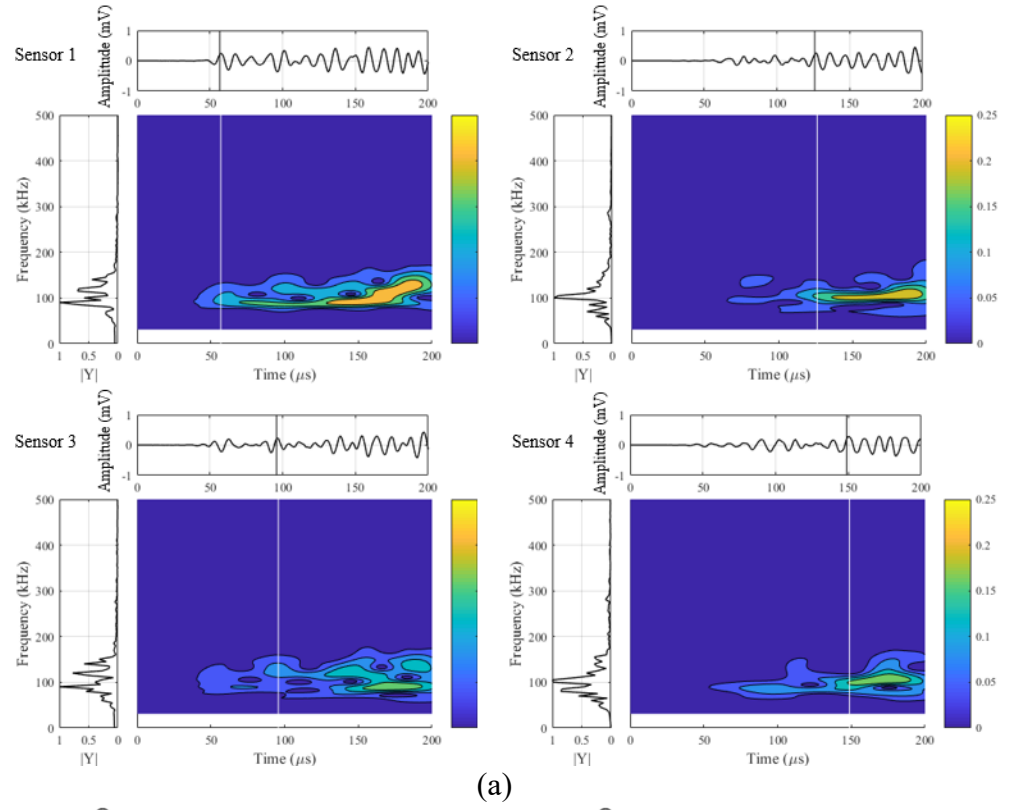


Figure 28. Time-frequency representations of difference signals under repeated excitation: (a) 1-3 direction flexural mode; and (b) 2-4 direction flexural mode.

## DEVELOPMENT OF THE MONITORING INTERFACE

In this study, four cases (Figure 29) are studied to achieve the overarching goal of monitoring the OI prostheses: degree of osseointegration post-surgery, looseness of prosthesis, bone fracture, and development of bone callous associated with compress-type fixtures. The first three are solved via *ex vivo* guided wave monitoring strategy, the last one will be introduced in the following sections by using an *in vivo* thin film sensor. A user interface is created to drive the *ex vivo* guided wave instrumentation and to visualize the results for clinical evaluation of the OI prosthesis.

Both hardware and software were developed to achieve a complete *ex vivo* monitoring solution. The hardware prototype consists of a National Instruments 8101 chassis with 2.0 GHz single-core CPU, 1 GB 800MHz DDR2 RAM, and 80 GB integrated hard-drive; this platform serves as the target controller to execute the monitoring and diagnose process. Included in the chassis are the data acquisition (DAQ) cards PXIe-6124 and PXIe-6361 offering 4 output channels and 4 input channels with a maximum sampling frequency of 1 MHz for all the 8 channels. A Thinkpad 440p laptop with 2.5 GHz 4-core CPU, 16GB RAM, and 500 GB hard-drive is utilized to be the master controller carrying out all of the system commands, transferring and saving experimental data, and analyzing and evaluating the performance of the prosthetics. The master controller and target controller are connected by an Ethernet patch cable, which means the whole system has the capability of long-distance remote monitoring through the internet. The cables from the NI data acquisition cards are connected to custom-designed piezoelectric interface boards that then feed the signals to/from the PZT elements bonded to the prosthetic rod. Figure 30(a) shows the NI-8101 chassis with the DAQ cards. The custom piezoelectric interface boards and connecting wires are shown in Figure 30(b).

To operate the system, software is written in LabVIEW which offers a flexible, graphical approach to operating the National Instrument system. All of the waveforms captured by the NI 8101 are

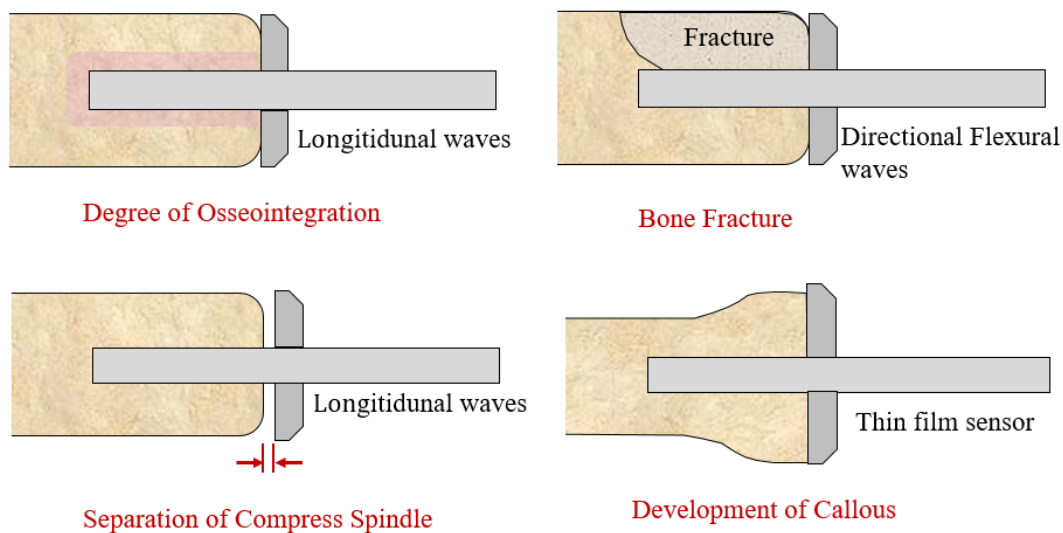


Figure 29. Four potential cases for the study objective: degree of osseointegration, separation of compress spindle, bone fracture, and development of callous.



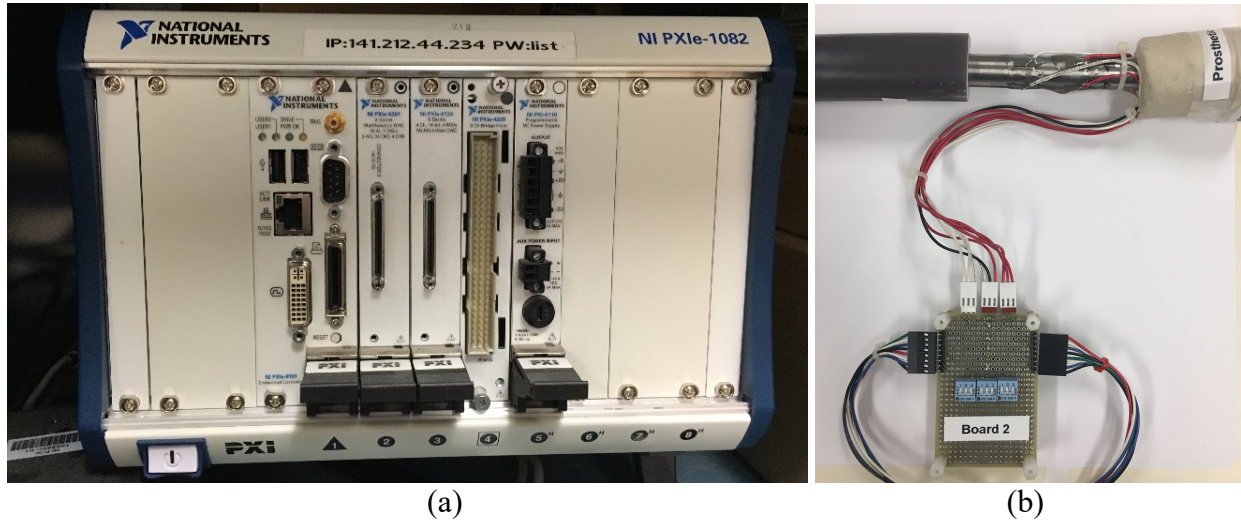


Figure 30. Experimental setup: (a) target controller NI-8101 chassis with DAQ cards installed, and (b) custom designed piezoelectric interface circuit.

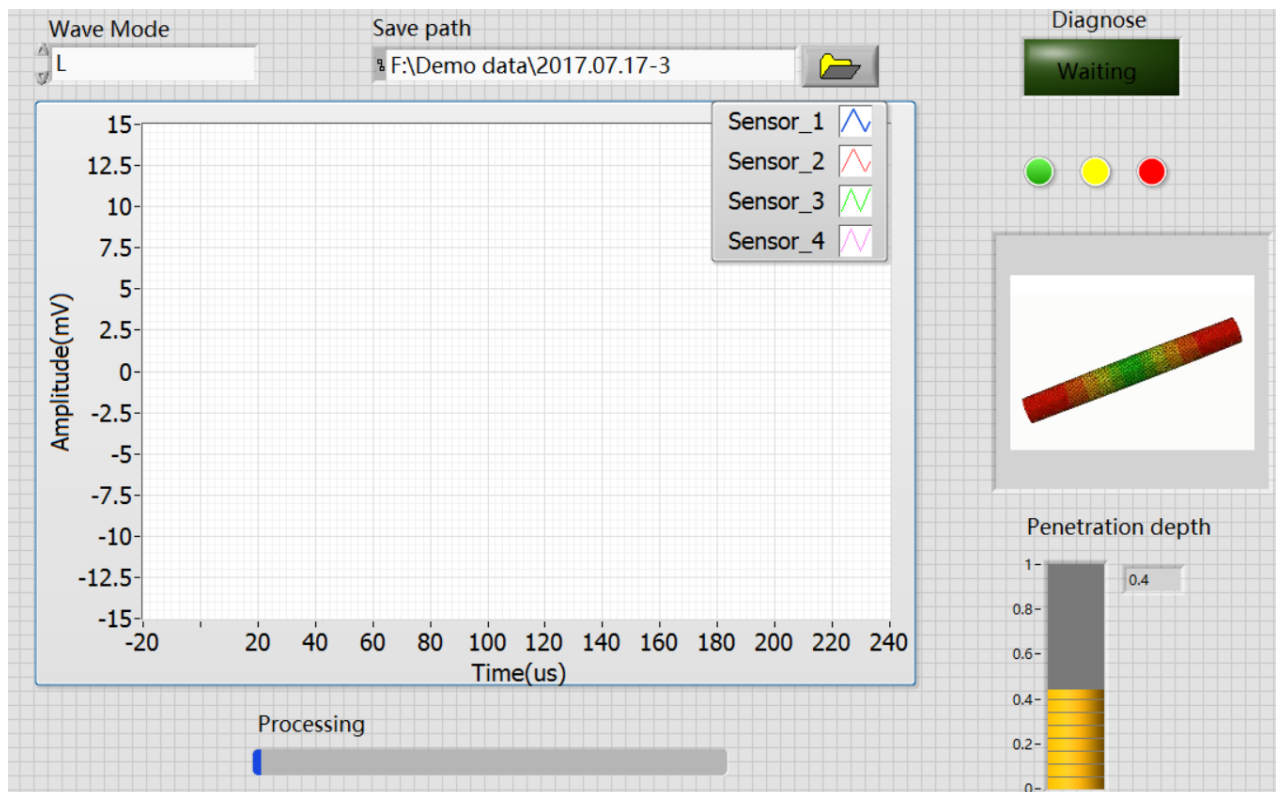


Figure 31. Front panel of the diagnose software.

transferred from the chassis to the remote equipment in real-time. Two different LabVIEW codes are loaded into the master and target controllers. The code running in the target controller executes the launching of the guided wave in the prosthetic titanium rod by applying 3-cycle tone burst



signals with a 100 kHz central frequency to all the four actuators. Meanwhile, reflected guided waves are measured and transferred to the master controller for further analysis.

Another LabVIEW program is written to receive and save the captured waveforms. Furthermore, the reflected waves were analyzed to measure changes. After the waveform data is transferred to the master controller, the data is saved and analyzed. A user-friendly dashboard offers end-users an interface so that clinical decisions can be made. Figure 31 shows the front panel of the laptop running the user-interface: a diagnose button, processing bar, the picture of the wave mode used to excite the prosthesis, and a green-yellow-red indicator light is offered. In this view of the user interface, the penetration depth of the prosthesis is calculated based on baseline of a fully seated fixture. Other user interfaces are also created to assess osseointegration and to detect bone fracture.

## **SUMMARY**

In this section, the flexural wave mode is explored to quantitatively identify bone fracture associated with OI prostheses. Fracture alters the flexural waves by superimposing their own wave packets in the received sensing signal. The numerical results presented suggest this approach has great promise for detecting fracture. However, the work is preliminary because it adopted an infinite element set at the percutaneous end of the prosthesis which prevented waves from reflecting from this end of the wave guide. Future work must explore the situation of waves reflecting off of the percutaneous end of the fixture. Second, the analysis of the flexural waves were only performed numerically. Future work must explore the approach in an experimental set-up.

## SECTION 5: DEVELOPMENT OF BIO-COMPATIBLE WIRELESS INDUCTIVE THIN FILM STRAIN SENSOR FOR BONE GROWTH MONITORING

### INTRODUCTION

The monitoring of orthopedic implants such as OI prostheses can benefit from the monitoring paradigms associated with the structural health monitoring (SHM) field <sup>41</sup>. One relevant technology that has emerged in SHM are thin film sensors for monitoring structural strain and damage states. Conformable thin film sensors can deform with the structure on which they are installed, providing them with a high degree of versatility in their application. These sensor solutions are also designed to be flexible and are therefore not prone to the same brittle failures observed in rigid counterparts. As a result, thin film solutions may be beneficial in monitoring bone and implants where surfaces are curved and complex. Similar to the sensing solutions proposed for smart implants, thin-film sensors can be designed as passive circuits with wireless inductive elements that receive power from and communicate data to a reader. SHM researchers have investigated various methods for wireless strain sensing and crack detection in thin film assemblies <sup>42-47</sup>. Specific to identifying cracks or peak strain in structures, wireless passive sensing solutions have been proposed where a sensing component is designed to fail under a specific damage state (*e.g.*, corrosion, cracking). A failed sensing component can provide an unambiguous change in the electrical properties of the sensor leading to robust detection of the damage event. For example, Wood *et. al.* <sup>48</sup> illustrates wireless sensing with two RFID circuits one of which is a reference circuit and the other is a sensor for detecting corrosion. Similarly, Zhang *et. al.* <sup>49</sup> proposed a “breakage-triggered” sensor where an acrylic bar is used as a brittle fuse in an RFID circuit designed to detect peak strain. Both Wood *et. al.* <sup>48</sup> and Zhang *et. al.* <sup>49</sup> are contained in three-dimensional sensor packages and are not designed using a thin film architecture. None the less, they teach means of using wireless passive sensors to detect limit states in a structure.

The goal of this section of the study is to explore the advancement of bio-compatible thin film sensors that can be used to monitor the growth and strain response of bone after implantation of a compress-type OI prosthesis. A key novelty of the work is the use of physical vapor deposition (PVD) and photolithography to deposit and pattern layers of bio-compatible polymers and metals on a flexible polymeric substrate. The sensor is designed to be passive as a resistor-inductor-capacitor (RLC) circuit whose inductive elements are used for wireless coupling with a wireless reader positioned outside the body. Attached to the surface of the bone, the sensor will offer a measure of axial strain using a thin film parallel plate capacitor whose capacitance changes under applied strain. In addition, a thin resistive element is also included in the RLC circuit that will exhibit a high degree of nonlinear response under applied strain. This resistive element is designed to track hoop strain associated with circumferential bone growth common in compress OI prosthesis fixtures. This section begins with a description of the design and fabrication of thin film circuit primitives for a thin film RLC sensing circuit including a strain-sensitive parallel plate capacitor, spiral coil inductor for wireless coupling, and resistive fuse element for peak strain

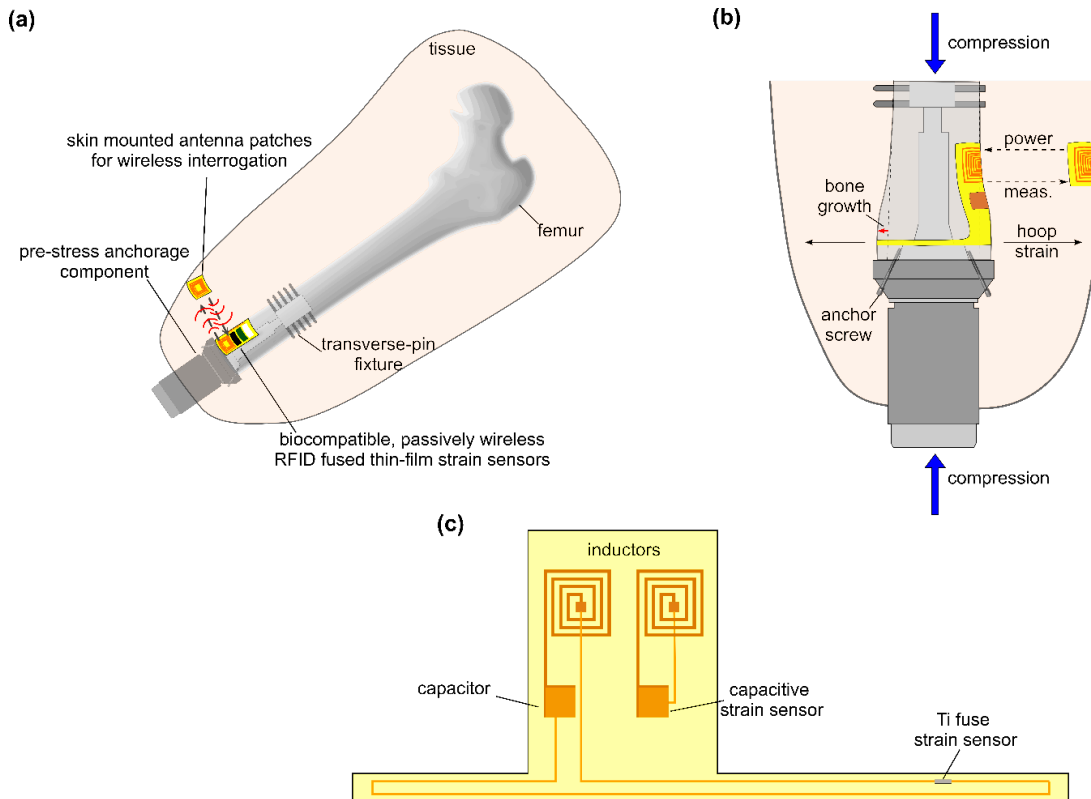


Figure 32. (a) Schematic of the proposed *in vivo* wireless thin film strain sensing system for a compression-type osseointegrated prosthesis fixture; (b) detailed view of sensor attachment to bone in compression region; (c) schematic of the thin film strain sensor with key circuit elements highlighted.

detection. In the next section, the individual circuit elements are fabricated and are experimentally validated to ensure their performance is as designed.

To monitor bone growth and strain response in OI prosthesis applications, a bio-compatible wireless thin-film sensor is developed. The sensor design is tailored for use in compress-type OI prosthesis fixtures but the operational concept of the device renders it suitable in a broader set of orthopedic implant applications. The sensor is designed as a passive RLC sensor that is intended to be wirelessly coupled to an inductor attached to an impedance analyzer positioned outside the body (Figure 32(a)). The thin film sensor is intended to be attached to the bone including wrapping around its circumference during surgical implantation to the OI prosthesis (Figure 32(b)). The thin film attached to the bone includes two separate RLC circuits. One circuit is designed to measure axial strain in the bone using a parallel plate capacitor whose dielectric layer changes thickness due to planar strain. A second RLC circuit is included with a titanium resistive element that can track monotonically increasing hoop strain in the bone (Figure 32(c)). The frequency response of the two RLC circuits are tuned to separate resonant frequencies that allow a single inductive reader connected to an impedance analyzer to measure the sensor output.

## DESIGN AND FABRICATION OF LCR THIN-FILM COMPONENT

### Plate Capacitor for Strain Sensing

Thin-film inductor and capacitor components of the RLC circuits are designed using implantable materials (*e.g.* gold, titanium and polyimide) and sealed within a bio-compatible coating (*e.g.* polyimide). A square parallel plate capacitor is designed with two gold conductive layers sandwiching a polyimide dielectric layer fabricated upon a flexible polyimide substrate. Gold and polyimide are biocompatible materials that are robust to harsh thermal, chemical, and physical environments<sup>50, 51</sup>. The capacitor design is investigated by varying its planar dimensions.

The theoretical value of capacitance,  $C$ , for a parallel plate capacitor is,

$$C = \epsilon_r \epsilon_0 \frac{A}{d} \quad (44)$$

where  $A$  is the area of overlap between the two plates (if the shape is rectangular,  $A = wl$  where  $w$  and  $l$  are width and length, respectively),  $\epsilon_r$  is the relative static permittivity of the material between the plates (*e.g.* for polyimide  $\epsilon_r=3.4$ ),  $\epsilon_0$  is the electric constant ( $\epsilon_0 = 8.854 \times 10^{-12} \text{ F}\cdot\text{m}^{-1}$ ), and  $d$  is the distance between the plates. Derived from equation (44), the change in capacitance that is caused by changes in the geometry of the capacitor can be represented as:

$$\delta C = \epsilon_r \epsilon_0 \left( \frac{w \delta l}{d} + \frac{l \delta w}{d} - \frac{wl}{d^2} \delta d \right) \quad (45)$$

Hence,

$$\delta C / C = \epsilon_x + \epsilon_y - \epsilon_z \quad (46)$$

where  $\epsilon_x$ ,  $\epsilon_y$  and  $\epsilon_z$  correspond to strain along the length, width and thickness of the parallel plate capacitor, respectively. Under the assumption of plane stress ( $\sigma_{zz} = \sigma_{zx} = \sigma_{zy} = 0$ ),  $\epsilon_z$  can be computed as,

$$\epsilon_z = -\frac{\nu}{1 - \nu} (\epsilon_x + \epsilon_y) \quad (17)$$

where  $\nu$  is the Poisson's ratio of the dielectric polymer situated between the conductive plates. By substituting equation (17) into equation (46), the relative change in capacitance for a free-standing capacitor under plane strain can be written as:

$$\delta C / C = \frac{1}{1 - \nu} (\epsilon_x + \epsilon_y) \quad (48)$$

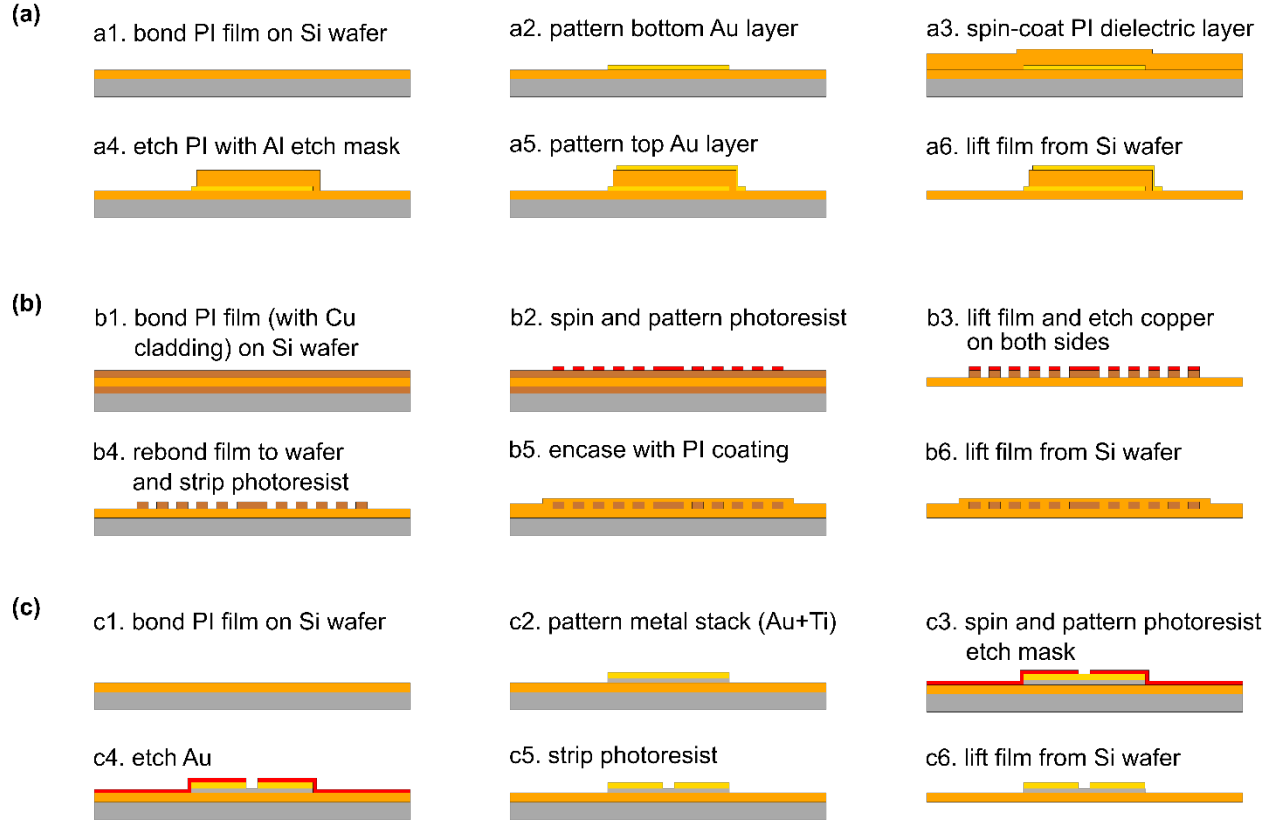


Figure 33. Fabrication flow of the: (a) capacitor, (b) inductor, and (c) fuse (not to scale).

When the free standing capacitor is under perfect uniaxial tensile loading (*e.g.*,  $\sigma_x = 0$  and  $\sigma_y \neq 0$ ), then  $\frac{\delta C}{C} = \frac{1}{1-\nu} \epsilon_y$ . When the thin-film capacitor is affixed to a structure that is under uniaxial tensile load, then the Poisson's ratio of the structure (or substrate),  $\nu_s$ , must be considered. In that case the percent change in capacitance is  $\frac{\delta C}{C} = \frac{1}{1-\nu} (1 - \nu_s) \epsilon_y$ . Finally, the gage factor,  $GF_c$ , of the capacitive strain sensor can then be calculated as,

$$GF_c = \frac{1 - \nu_s}{1 - \nu} \quad (49)$$

where  $GF_c$  is defined as the percent change in capacitance per unit strain.

A schematic of the capacitor fabrication process can be seen in Figure 33(a). The capacitor fabrication is conducted in the Lurie Nanofabrication Facility at the University of Michigan and begins with the attachment of a commercial 50  $\mu\text{m}$  polyimide (PI) flexible substrate (American Duarfilm FT Kapton 200 HN) to a silicon wafer using quartz wax (Logitech 0CON-200). The silicon wafer offers a rigid substrate only for processing. Once the PI substrate is bonded, a layer of gold is patterned on top of the PI substrate to serve as both the bottom plate of the capacitor and

electrical traces for the sensing circuit. The gold layer is deposited in a controlled manner using optical lithography which is a well-established process in microelectromechanical systems (MEMS). First, the polyimide substrate surface is treated with an oxygen plasma etch to promote the adhesion of metal layers upon it. Next, a sacrificial photoresist layer is spun on the substrate. Areas of the photoresist layer are exposed to UV light through a stencil-like mask. The photoresist layer is developed to remove areas of the layer that have been exposed to light with solution. Next, a thin metallic adhesion layer of chromium 50 nm thick is deposited followed by a 700 nm gold layer both deposited over the entire substrate using physical vapor deposition (PVD). The photoresist remaining is exposed to lift off the undesired metal layer leaving only the desired pattern of metal which is the bottom capacitor plate and electrical traces of the sensor.

After the initial metal layer of gold is deposited, a polyimide dielectric layer (HD Microsystems PI 2525 polyimide) is spin-coated onto the substrate at a speed of 5000 rpm and is soft baked at 90°C until firm. The polyimide is then fully cured in a vacuum oven in a nitrogen gas environment by ramping from 25°C to 350°C and holding for 1 hour before gradually cooling back to 25°C. According to the product datasheet<sup>31</sup>, the thickness of PI spin-coated at 5000 rpm would be around 5.5 µm after curing for 30 min at 200°C and 30 min at 350°C. Although curing occurs for 1 hour at 350°C, the thickness of the cured polyimide is confirmed to still be approximately 5.5 µm. The polyimide layer is then etched using reactive ion etching (RIE). Etching is intended to pattern the dielectric layer in the capacitor and to remove the polyimide covering the gold electrodes that are connected to the bottom plate of the capacitor. A layer of aluminum is first sputtered to the top surface of the PI to create a hard mask. Lithography and wet chemical etching is used to pattern the aluminum mask. With the hard mask in place, the substrate is placed in a chamber parallel plate tool (Plasmatherm 790) for RIE. The etch rate is controlled to ensure the 5.5 µm upper layer of PI is removed except where masked by the aluminum layer. Using the same procedure described for the lower gold plate, an upper 700 nm thick gold plate is deposited on the PI dielectric layer using a 5 nm chromium adhesion layer. Following the fabrication process, the PI substrate can be lifted from the silicon wafer for device characterization and application.

### Spiral Coil Inductor for Wireless Communication

In the proposed RLC circuit for the thin film sensor, the inductor not only should be optimized for inductive coupling of the sensor with a reader, but also should be tailored so that it is insensitive to in-plane strain (*e.g.*,  $\epsilon_x$ ,  $\epsilon_y$ ). The inductance of a square spiral inductor (Figure 34) can be calculated from the inductor diameter ( $D_{out}$ ), turn width ( $w$ ), spacing between turns ( $s$ ), and number of turns ( $n$ ) using expressions derived by Mohan *et al.*<sup>52</sup>. This requires maximizing the coil inductance while simultaneously minimizing the resistance of the inductor, which means maximizing the quality factor,  $Q$ , as defined:

$$Q = \frac{\omega L}{r} \quad (50)$$

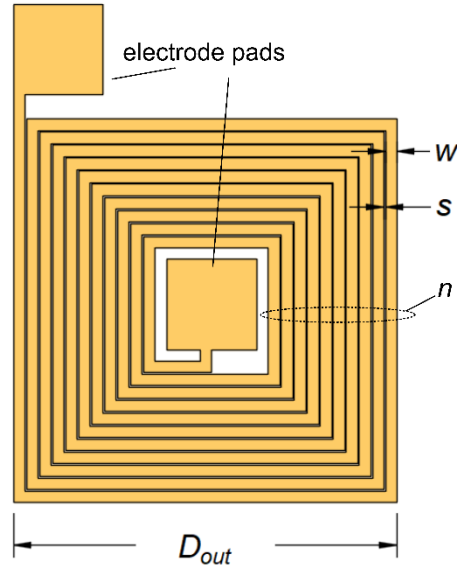


Figure 34. Planar design of square spiral coil inductor. Outer diameter ( $D_{out}$ ), turn width ( $w$ ), spacing between turns ( $s$ ), and number of turns ( $n$ ) are marked.

where  $L$  is the inductance,  $r$  is the DC resistance (DCR), and  $\omega$  is the radian operating frequency. Geometry of the inductor plays a very important role in designing an inductor with a high quality factor. A single-layer, thin-film, square coil antenna is selected to limit strain sensitivity and to maximize utilized geometry;  $n$ ,  $s$ , and  $w$  are optimized to maximize  $Q$ . The thickness of the thin film inductor is critical in determining the DC resistance in equation (50) with the optimized planar geometry. For example, a design of the inductor used in this study is  $D_{out}=16.925$  mm,  $w=500$   $\mu\text{m}$ ,  $s=75$   $\mu\text{m}$ , and  $n=10$ ; this yields a theoretical inductance of  $L = 1.386$   $\mu\text{H}$ .

The fabrication flow for the inductor can be seen in Figure 33(b). In order to achieve a high  $Q$ , the DCR of the metal layer used in fabrication must be as low as possible. Fabrication is first attempted at the Lurie Nanofabrication Facility by electroplating gold and copper metal layers on PI. However, numerous issues are encountered including difficulty in achieving a uniform metal layer without stress issues that cause brittle cracking in the metal layer. Due to the importance of a low DCR with a well-controlled deposition of a uniform metal layer, a commercial polyimide substrate with a thick layer of copper cladding on both sides (DuPont Pyralux-AP9111R) is utilized as the source of conductive material and polymer film as shown in first step of Figure 33(b). The three-layer film has a 25.4  $\mu\text{m}$  thick polyimide layer sandwiched between two 35  $\mu\text{m}$  thick layers of copper. A layer of photoresist is patterned as an etch stop and the top copper layer is etched to create the shape of the inductor. The bottom copper layer is etched off completely at the same time. The photoresist is then stripped from the inductor copper to fabricate a relatively thick copper film with a higher quality factor. The inductor is then encased in a thick polyimide layer repeating the spin coating process previously described for the capacitor. Because a thicker polyimide layer is needed to coat the inductor than is used as a dielectric layer for the capacitor, two layers of polyimide are spun and stacked over the inductor. The existing inductor and polyimide layers are cleaned prior to spinning the initial polyimide encasing layer using an Argon plasma etch. Each

layer of polyimide is spun at 2000 rpm for a target thickness of 13  $\mu\text{m}$ . Each layer is soft baked at 90°C until firm and the final film is fully cured in a vacuum oven offering a nitrogen gas environment; the oven is ramped from 25°C to 350°C and holding at 350°C for 1 hr before gradually cooling back to 25°C.

The fabricated inductor has a small amount of inherent resistance,  $R$ . When the inductor and capacitor are combined in parallel on the same substrate as shown in Figure 32, a strain-sensitive RLC circuit is created. The RLC circuit has a resonant peak at a frequency defined by the inductance,  $L$ , and capacitance,  $C$ , of the circuit; changes in capacitance due to strain will result in a distinguishable shift in resonant frequency.

### Metal Fuse for Threshold Strain Sensing

To create a second RLC circuit capable of detecting high levels of strain (such as the hoop strain associated with circumferential bone growth), a resistive fuse element is proposed. The fuse is designed to have minimal but constant electrical resistance until a strain threshold is reached corresponding to the metal in the fuse yielding. Post yielding, the resistance of the fuse exponentially increases under monotonically increasing levels of strain. A metal thin film is chosen to serve as the fused element because a metal layer can be easily fabricated using the previously described thin film fabrication methods. Titanium is selected as the fuse material because it is has low resistance (pre-yield) and is less ductile compared to many other metals (such as gold). Another reason is that titanium can also be used as an adhesion layer making circuit design and fabrication easier.

The fuse is fabricated as a lithographically patterned metal electrode (stacked gold and titanium layers with the necked area as shown in Figure 35(a)); the necked area of the gold is etched to expose a small area of the titanium layer (as show in Figure 35(b)). The process is controlled to yield a titanium fuse element with length,  $l_f$ , width,  $w_f$ , and thickness,  $t_f$ , as shown in Figure 35(c). The fabrication process for the metal fuse is summarized in Figure 33(c). First, the PI substrate bonded to the silicon wafer has a titanium seed layer deposited based on the optical lithography and PVD steps previously described for the gold electrodes of the capacitor. However, during metal deposition, the thickness of the titanium layer (which normally serves as a thin adhesion layer) is enlarged to serve as a fuse with lower initial resistance. A photoresist mask is spun on top

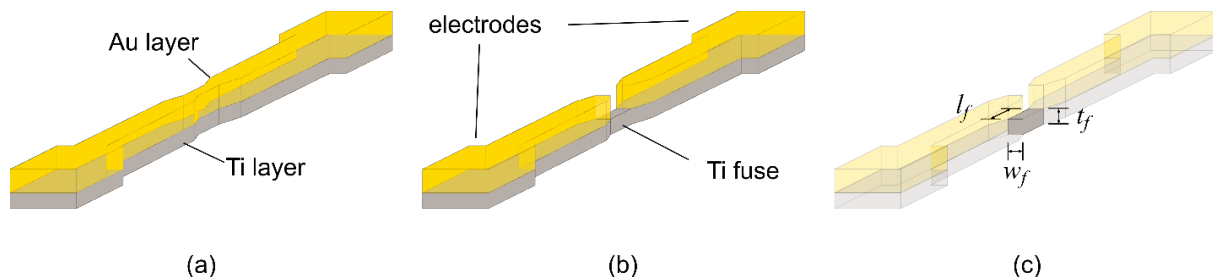


Figure 35. Schematics of fuse fabrication: (a) fuse element before gold etching; (b) fuse element after gold etching; (c) the dimensions of the fuse element (not to scale).



of the gold layer and cured as an etch stop so that the gold can be etched from only the fuse portion of the metal electrodes. The fabrication process is finished by removing the photoresist and lifting the film from the wafer.

## WIRELESS STRAIN THRESHOLD SENSING SYSTEM INTEGRATION

The electrical components, including two capacitors, two inductors and a fuse, are utilized to create a complete passive wireless strain sensing system as shown in Figure 36. While the previous sections described the fabrication of each circuit element type, the fabrication flow that combines the primary circuit elements is summarized in Figure 36(a). This system is designed as two circuits: one to measure bone strain (using the capacitor and inductor) and a second with the resistive fuse (also using the capacitor and inductor) to detect high hoop strain in the bone. Each circuit has an inductor and capacitor so that a read inductor can be used to interrogate the resonance of the circuit. The resonant frequency of the first RLC circuit,  $f_{r1}$ , is used as a reference to show that the sensor and readout is functional. Additionally,  $f_{r1}$  can be utilized for strain sensing by monitoring the shift of  $f_{r1}$  due to the strain-induced change in the capacitance of the strain sensitive capacitor. In the second RLC circuit, a fuse that is designed to yield is integrated to allow for detecting when hoop strain exceeds a specific threshold. While this sensing system described can be applied to various orthopedic applications, it has been optimized for monitoring bone-growth in OI prosthetics.

The system fabrication integrates the aforementioned electrical components in six process steps shown in Figure 36(a): (1) a polyimide film with copper claddings on one side is bonded to a silicon wafer; (2) the top copper layer is etched to create an inductor and the bottom layer of a capacitor on one side of the film (note, the bottom gold layer of the capacitor is replaced with copper); (3) the copper layer is encased in polyimide using spin coating and curing; (4) the polyimide layer is then etched using RIE to create a thin dielectric layer for the capacitors and to provide a route to connect the center of the inductor to the top parallel plate of the capacitor; (5) the top layer of the capacitor as well as an electrode connecting the top layer to the center of the

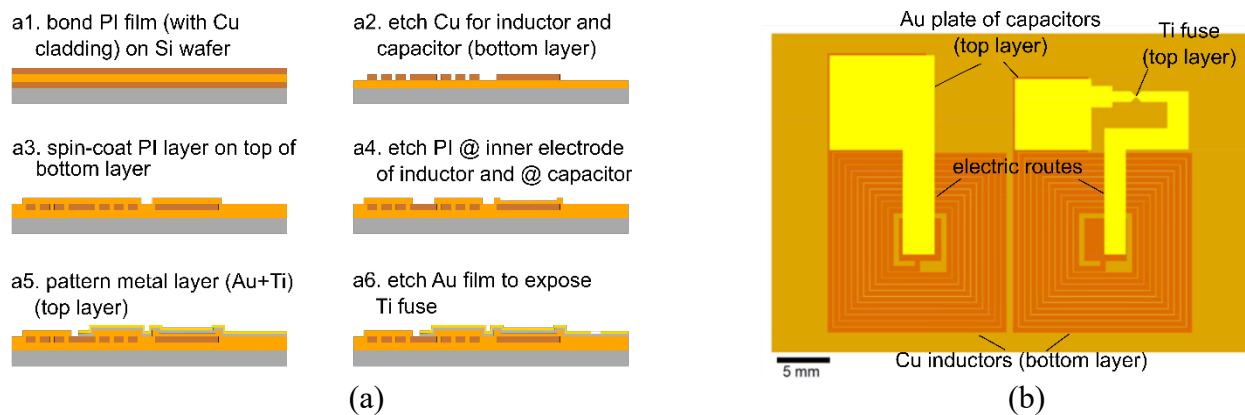


Figure 36. Complete passive wireless thin film sensor: (a) fabrication flow (not to scale) and (b) design layout of the wireless threshold strain sensor.

inductor is patterned over the previous layers using optical lithography and a gold metal layer; (6) the gold at the fuse area is etched to expose the titanium seed layer as a fuse. The photoresist is then stripped to complete the fabrication process. At the end of the fabrication, a final encasing polyimide layer is deposited over the final metal layer for robustness and biocompatibility so that the sensor be used in a real medical environment. The planar design of the thin film strain sensing system can be seen in Figure 36(b).

It should be noted that the fabrication of the capacitors when integrated into the total system design is slightly different from the one that is mentioned in the capacitor component design. First, the bottom electrode is copper; this change in metal should not affect the capacitor performance because it is the dielectric layer that controls its strain-sensitive performance. In step (3) of the system integration, the copper layer of the inductor and lower electrodes of capacitors are first encased by using two stacking layers of  $\sim 13\text{ }\mu\text{m}$  thick polyimide. In order to fabricate the dielectric layer of the capacitors in a conservative fashion, the  $\sim 26\text{ }\mu\text{m}$  thick polyimide film is further etched using RIE in step (4) to form the  $\sim 10\text{ }\mu\text{m}$  thick dielectric layer rather than directly spinning polyimide ( $5.5\text{ }\mu\text{m}$  thick). Hence, in a fabricated sensing system, the dielectric layer will be larger reducing the capacitance value of the capacitors. While the capacitors will have lower levels of capacitance, the change makes fabrication of the fully integrated thin film sensing system easier.

## SUMMARY

A passive wireless thin-film sensing system would benefit many applications in structural health monitoring, among them are monitoring bone growth and strain in orthopedic implant applications. In this section, a passive wireless strain sensing system is proposed using thin film fabrication methods to design a multifunctional strain sensor measuring low level bone strain and high levels of hoop strain associated with bone growth. Thin film circuit components, including parallel plate capacitors, square coil inductors and miniaturized resistive fuses, are fabricated and patterned using biocompatible materials in a traditional lithographic process. In the next section, the thin film prototypes are tested to verify their performance is as designed.

## SECTION 6: CHARACTERIZATION AND EXPERIMENTS OF THE BIO-COMPATIBLE WIRELESS INDUCTIVE THIN FILM STRAIN SENSOR

### INTRODUCTION

Individual capacitive and inductive circuit components, in addition to the complete strain sensor system, are electrically characterized using an impedance analyzer (Agilent 4294A) with impedance observed using phase ( $\theta$ ) and magnitude ( $|Z|$ ) frequency sweeps. The resistance of the fuse components are measured using a digital multimeter (Agilent 34461A).

To experimentally validate the thin film sensor (and its components), it will be tested on standard PVC coupons and on a synthetic sawbone as shown in Figure 37. First, the backside of the flexible polyimide films are roughed with sand paper and cleaned by acetone after liftoff from the rigid silicon substrate to promote better attachment to the testing coupons (PVC coupon and sawbone). The thin-film components are bonded to PVC coupons using cyanoacrylate fast-acting adhesive (Tokyo Sokki Kenkyujo CN adhesive). A strain gage is bonded to the back side of the same PVC coupon to serve as a baseline measurement of strain. The PVC coupons are then loaded in four point bending as shown in Figure 37(a). A computer-controlled stepper motor is utilized to drive

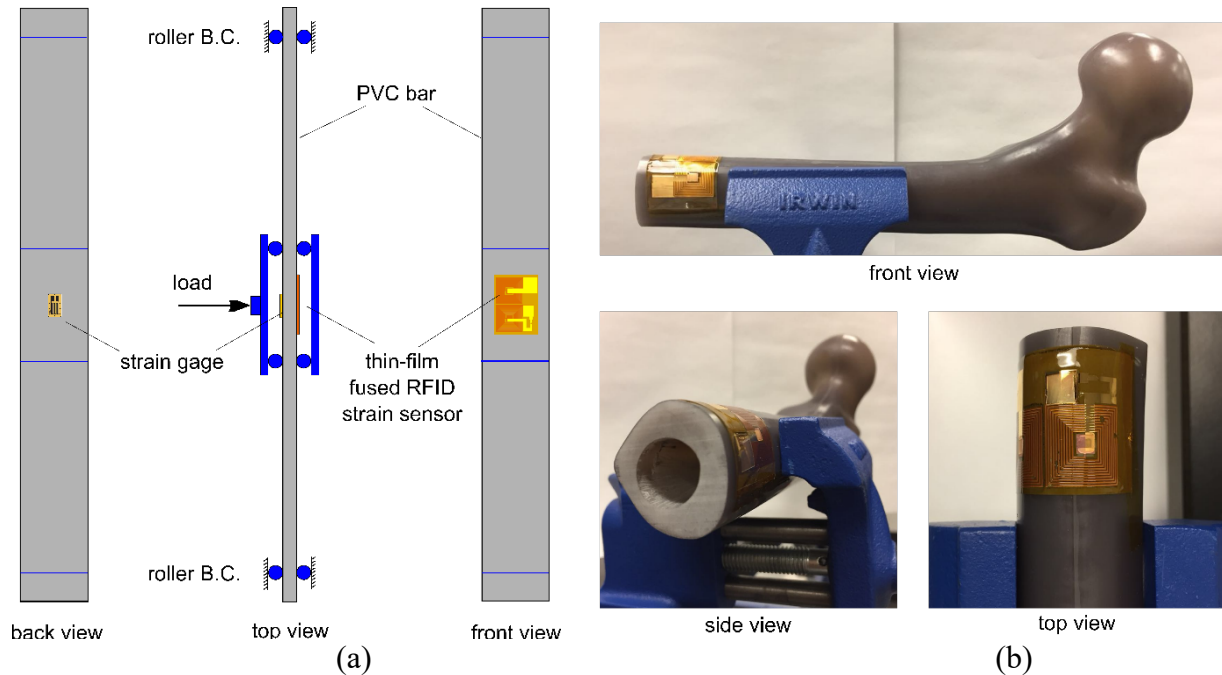


Figure 37. (a) Schematic of the loading setup and a thin-film fused RFID strain sensor on the front of a PVC bar, and (b) photos of a polyurethane femur model (with a thin-film fused RFID strain sensor mounted) held on a vise.

a turn screw linear actuator that applies load to a custom sample fixture. Additional testing is performed on the wireless strain sensors with the thin films attached to a realistic bone surface. Figure 37(b) shows the photos of a polyurethane femur model (*i.e.*, sawbone) with the conformable thin-film strain sensor bonded by cyanoacrylate fast-acting adhesive.

## LCR COMPONENT CHARACTERIZATION

### Cu/Au Capacitor

Three square capacitors with various side lengths (2 mm, 4 mm and 10 mm) are first fabricated on polyimide using the process previously described. The theoretical values of capacitance for the capacitors in addition to their gage factors are obtained using equation (44) and equation (49). The fabricated capacitors are mounted to the PVC coupons and tested under four point bending with the impedance analyzer used to continuously measure impedance over a wide range of frequencies. Experimental data is used to experimentally measure capacitance and to ascertain the capacitor gage factor. The details of the samples and the measured values of capacitances are shown in Table 4. The theoretical capacitances are all higher by roughly 3%. The lower measured capacitance of the thin film samples is attributed to slightly thicker dielectric layers than theoretically predicted (5.5  $\mu\text{m}$ ) by the process parameters.

Under four point bending, the gage factor can be estimated for the three capacitor samples. The change in capacitance as a function of strain is measured. The response of the relative change in capacitance for the three samples are plotted against measured strain in Figure 38. The 4 and 10 mm sized capacitors are nearly linear with R-squared values near 1. The smaller 2 mm square

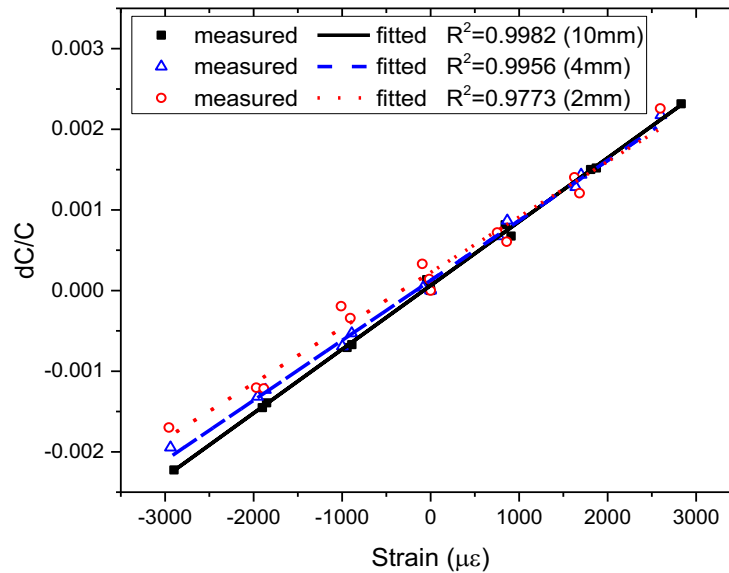


Figure 38. Relative change of capacitance as a function of applied strain for the three capacitive sensors with different sizes.

capacitor is less linear but the R-squared values of a linear regression is still high at 0.98. Based on the dimensions of the capacitors listed in Table 5, the theoretical values of the gage factor can be calculated for the three thin-film capacitors. Because  $\nu$  is 0.34 for polyimide and  $\nu_s$  is 0.45 for PVC at room temperature, the theoretical values of  $GF_c$  of the capacitors is estimated to be 0.83 by using equation (49). The gage factors for the larger capacitors appear to converge toward the theoretical value. For example, the 10 mm capacitor is within 5% of the theoretical gage factor. These results indicate the accuracy and quality of the design and fabrication of the capacitors.

**Table 4.** Capacitances and gage factors of the fabricated capacitive strain sensors.

Sample	$l$ or $w$ (mm)	$d$ ( $\mu\text{m}$ )	Capacitance (pF)		Gage factor	
			theoretical	measured	theoretical	measured
capacitor 1	2	5.5	21.89	21.11	0.83	0.69
capacitor 2	4	5.5	87.57	85.18	0.83	0.74
capacitor 3	10	5.5	547.34	529.44	0.83	0.79

## Cu Inductor

Five types of inductors with different geometric parameters are fabricated and tested as summarized in Table 5. The measured inductances are very close to the theoretical values, except the type 2 which has a smaller number of turns ( $n = 4$ ). A final fabricated thin-film copper inductor of type 3 is shown in Figure 39(a) with the impedance magnitude and phase plotted as a function of frequency in Figure 39(b). The final design is chosen to maximize the inductor quality factor

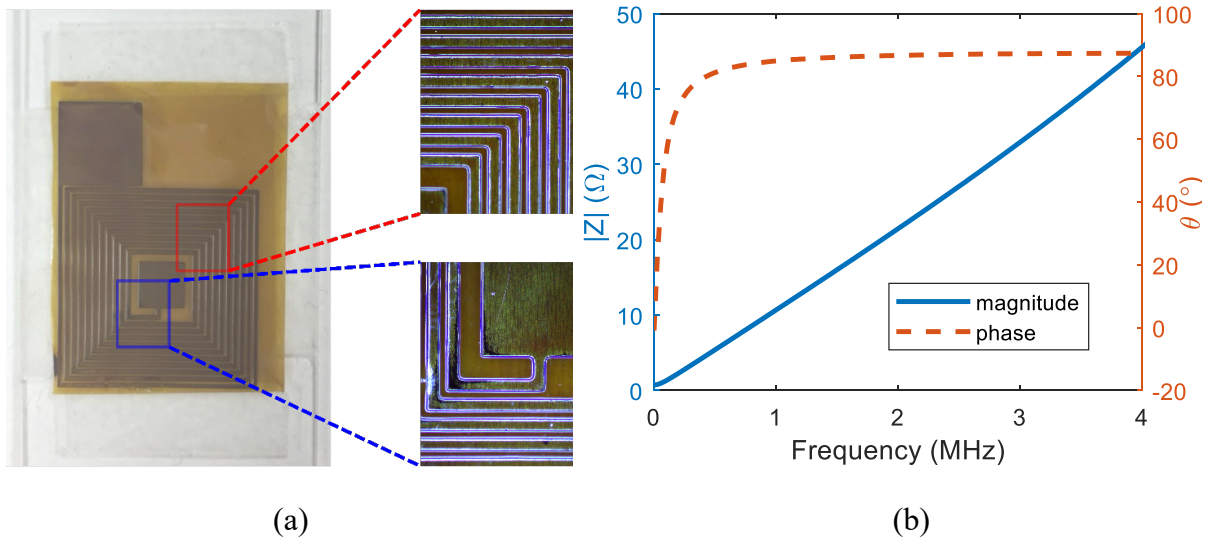


Figure 39. (a) Photo of the fabricated thin-film copper inductor (type 3) on polyimide (detailed microscopic images show on the right); (b) phase and impedance curves for the inductor characterization.

while minimizing the inductor footprint. The type 3 inductor, with  $D_{out}=16.925$  mm,  $w=500$   $\mu\text{m}$ ,  $s=75$   $\mu\text{m}$ , and  $n=10$ , is chosen as the inductor in the integrated system to achieve the balance between a large  $L/R$  value and a suitable size. The designed type 3 inductor with a footprint of roughly 17 mm<sup>2</sup> has its DCR measured as 934 m $\Omega$ . The inductance is estimated to be 1.691  $\mu\text{H}$  with a quality factor of around 11.38 at 1 MHz, as determined from the impedance spectra.

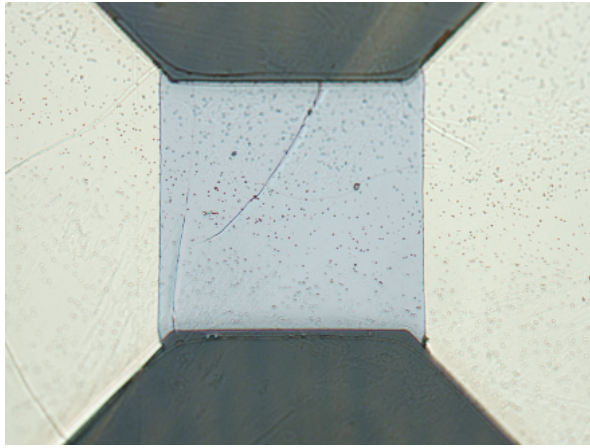
**Table 5.** Inductances and resistances of the fabricated thin-film inductors.

Type	Geometric parameters				$R(\Omega)$	$L(\mu\text{H})$		$L/R(\mu\text{H}/\Omega)$
	$D_{out}(\text{mm})$	$w(\mu\text{m})$	$s(\mu\text{m})$	$n$	meas.	theo.	meas.	meas.
1	11.675	250	75	10	1.945	1.233	1.264	0.650
2	13.450	1000	75	4	0.455	0.192	0.426	0.937
3	16.925	500	75	10	0.934	1.386	1.691	1.810
4	19.900	1000	75	7	0.620	0.678	0.721	1.162
5	25.800	1000	75	11	0.702	2.035	2.133	3.038

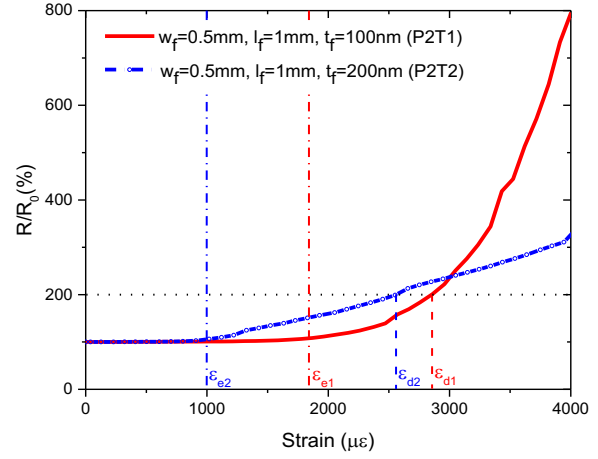
## Titanium Fuse

The electrical behavior of the resistive fuse elements are characterized to optimize their design. It is known that different PVD tools might cause different stress states within fabricated metal films during evaporation. In this study, the Angstrom Engineering EvoVac Evaporator is chosen to deposit the thin titanium layer during fabrication. As an important sensing component in the application of the hoop strain *in vivo* sensor (shown Figure 32(c)), titanium resistive elements of varying geometries are fabricated in the Lurie Nanofabrication Facility. An example of one such fuse is shown under an optical microscope in Figure 40(a) with  $w_f = 0.1$  mm,  $l_f = 0.1$  mm, and  $t_f = 200\text{nm}$ . The titanium elements are tested under monotonically increasing tensile strain using PVC coupons loaded in four-point bending (as previously described) with element resistance measured. Figure 40(b) shows two typical resistance responses to increasing tensile strain for specimens of varying film thickness (*i.e.*, 100 and 200 nm). While there is some variation between the tests, the fuse resistances are insensitive to strain within the range of  $(0, \epsilon_c)$  which corresponds to pre-yield stress in the titanium film. After yielding, the element resistance increased nonlinearly in a relatively exponential fashion. The resistance nonlinearity occurs due to the film undergoing plastic deformation while also forming micro-cracks due to high level of tensile strain at impurities in the film. A designed strain threshold is established by a resistance level that is two times the initial resistance ( $2R_0$ ) as denoted as  $\epsilon_d$  or  $\epsilon_{2R0}$ . Similarly, the strain when ten times and twenty times of the initial resistance are reached are denoted as  $\epsilon_{10R0}$  and  $\epsilon_{20R0}$ , respectively.

The dimensions and labeling convention of the fuse samples with varying widths, lengths, and thicknesses are shown in Table 6. Five planar types (denoted P1 through P5) are categorized with the combination of three length options ( $l_f=0.1, 1$  or  $2$  mm) and three width options ( $w_f=0.1, 0.5$  or  $1$  mm). Three thickness types (denoted T1 through T3) have three thicknesses ( $t_f=100, 200$  or  $300$  nm). Strain levels ( $\epsilon_{2R0}$ ,  $\epsilon_{10R0}$  and  $\epsilon_{20R0}$ ) corresponding to the resistances of  $2R_0$ ,  $10R_0$  and  $20R_0$



(a)



(b)

Figure 40. (a) Microscopy photo of a fabricated titanium fuse ( $w_f=0.1$  mm,  $l_f=0.1$  mm,  $t_f=200$ nm), and (b) typical resistive response of the titanium fuses to monotonically increasing tensile strain (fuse P2T1 is  $w_f=0.5$  mm,  $l_f=1$  mm,  $t_f=100$ nm,  $\epsilon_{e1}=1700$   $\mu\epsilon$ , and  $\epsilon_{d1}=2800$   $\mu\epsilon$ ; fuse P2T2 is  $w_f=0.5$  mm,  $l_f=1$  mm, and  $t_f=200$ nm,  $\epsilon_{e2}=1000$   $\mu\epsilon$ , and  $\epsilon_{d2}=2550$   $\mu\epsilon$ ).

for each fuse sensor in the P2 family are listed in Table 7. Both thinner (100 nm) and thicker (300 nm) titanium layers are more prone to large resistance increases. This interesting phenomena could possibly be due to mechanical weakness in the film resulting lack of overall material in the 100 nm film and greater residual stresses from deposition in the 300 nm film. As a result, the empirical evidence suggests the 200 nm film (*i.e.*, T2) is a potentially more robust middle ground thickness.

**Table 6.** Dimensions and labeling convention of fuse samples.

Sample label	Planar type			Thickness type	
	label	$l_f$ (mm)	$w_f$ (mm)	label	$t_f$ (nm)
P1T2	P1	0.1	0.5	T2	200
P2T2	P2	1	0.5	T2	200
P3T2	P3	2	0.5	T2	200
P4T2	P4	1	0.1	T2	200
P5T2	P5	1	1	T2	200
P2T1	P2	1	0.5	T1	100
P2T3	P2	1	0.5	T3	300

**Table 7.** Results of the fuses of planar type P2 with different thicknesses.

Thickness	Sample label	$R_0(\Omega)$	$\varepsilon_{2R0}(\mu\varepsilon)$	$\varepsilon_{10R0}(\mu\varepsilon)$	$\varepsilon_{20R0}(\mu\varepsilon)$
T1 ( $t_f=100$ nm)	P2T1_S1	133.60	2050	2400	7500
	P2T1_S2	148.60	1950	2500	2950
	P2T1_S3	152.90	2050	2100	2600
	P2T1_S4	99.18	2500	5400	4800
	P2T1_S5	88.59	2050	2400	4200
	<i>mean</i>	<i>124.57</i>	<i>2120</i>	<i>2960</i>	<i>4410</i>
	<i>std</i>	<i>29.16</i>	<i>217</i>	<i>1372</i>	<i>1946</i>
	<i>cov</i>	<i>23%</i>	<i>10%</i>	<i>46%</i>	<i>44%</i>
T2 ( $t_f=200$ nm)	P2T2_S1	29.66	3200	-	-
	P2T2_S2	31.55	3900	-	-
	P2T2_S3	74.03	4000	-	-
	P2T2_S4	30.30	2500	-	-
	P2T2_S5	12.76	5500	-	-
	<i>mean</i>	<i>35.66</i>	<i>3820</i>	-	-
	<i>std</i>	<i>22.79</i>	<i>1117</i>	-	-
	<i>cov</i>	<i>64%</i>	<i>29%</i>	-	-
T3 ( $t_f=300$ nm)	P2T3_S1	126.50	1200	2050	2250
	P2T3_S2	69.13	1200	2550	4200
	P2T3_S3	54.74	1600	2800	4650
	P2T3_S4	40.40	1700	2500	3150
	P2T3_S5	75.02	1250	2300	3000
	<i>mean</i>	<i>73.16</i>	<i>1390</i>	<i>2440</i>	<i>3450</i>
	<i>std</i>	<i>32.70</i>	<i>241</i>	<i>282</i>	<i>966</i>
	<i>cov</i>	<i>45%</i>	<i>17%</i>	<i>12%</i>	<i>28%</i>

The behavior of titanium fuses in the T2 thickness category are also documented in Table 8. By comparing planar type P1, P2 and P3 with different lengths (with  $t_f=200$  nm and  $w_f=0.5$  mm held constant), it is observed that the designed strain level ( $\varepsilon_d$  or  $\varepsilon_{2R0}$ ) decreases slightly with increasing length with mean values of 3820  $\mu\varepsilon$  ( $l_f=0.1$  mm), 3820  $\mu\varepsilon$  ( $l_f=1$  mm) and 3040  $\mu\varepsilon$  ( $l_f=2$  mm), respectively. By comparing planar type P4, P2 and P5 with different widths (with  $l_f=1$  mm and  $t_f=200$  nm held constant), it is hard to conclude the influence of increasing widths on the designed strain level ( $\varepsilon_d$  or  $\varepsilon_{2R0}$ ) with mean values of 5020  $\mu\varepsilon$  ( $w_f=0.1$  mm), 3820  $\mu\varepsilon$  ( $w_f=0.5$  mm) and 5190  $\mu\varepsilon$  ( $w_f=1$  mm), respectively.

Although there are five samples for each type of fuse considered, the number of samples is still not sufficient to reach a statistical conclusion. The tests conducted are only monotonic tensile strain tests because a study on hysteresis behavior is not required for designing a hoop strain sensor for the osseointegration application (*i.e.*, bone growth is only monotonically increasing). For now,



the results are studied as a basis for selecting a reasonable fuse design for this study and pending validation of consistency in the fuse behavior is needed in the future.

**Table 8.** Results of the fuses of thickness type T2 with different planar types.

Planar type	Sample label	$R_0(\Omega)$	$\varepsilon_{2R0}(\mu\epsilon)$	$\varepsilon_{10R0}(\mu\epsilon)$	$\varepsilon_{20R0}(\mu\epsilon)$
P1 ( $l_f=0.1$ mm, $w_f=0.5$ mm)	P1T2_S1	5.8	3600	9500	-
	P1T2_S2	5.62	3600	-	-
	P1T2_S3	4.94	2900	5700	-
	P1T2_S4	5.74	2900	9300	-
	P1T2_S5	6.52	6100	-	-
	<i>mean</i>	5.72	3820	8167	-
	<i>std</i>	0.56	1322	2139	-
	<i>cov</i>	10%	35%	26%	-
P3 ( $l_f=2$ mm, $w_f=0.5$ mm)	P3T2_S1	101.7	2800	-	-
	P3T2_S2	113.3	2400	-	-
	P3T2_S3	44.36	3700	-	-
	P3T2_S4	63.77	2000	3000	3800
	P3T2_S5	28.75	4300	-	-
	<i>mean</i>	70.38	3040	-	-
	<i>std</i>	36.32	945	-	-
	<i>cov</i>	52%	31%	-	-
P4 ( $l_f=1$ mm, $w_f=0.1$ mm)	P4T2_S1	73.77	5500	6400	8300
	P4T2_S2	59.38	10000	-	-
	P4T2_S3	82.5	2900	4050	5050
	P4T2_S4	101.8	3100	3200	4000
	P4T2_S5	62.04	3600	-	-
	<i>mean</i>	75.90	5020	4550	5783
	<i>std</i>	17.20	2968	1658	2242
	<i>cov</i>	23%	59%	36%	39%
P5 ( $l_f=1$ mm, $w_f=1$ mm)	P5T2_S1	73.81	3100	-	-
	P5T2_S2	36.26	3000	4200	9800
	P5T2_S3	58.07	3700	-	-
	P5T2_S4	79.58	10000	-	-
	P5T2_S5	11.01	6150	-	-
	<i>mean</i>	51.75	5190	-	-
	<i>std</i>	28.29	2977	-	-
	<i>cov</i>	55%	57%	-	-

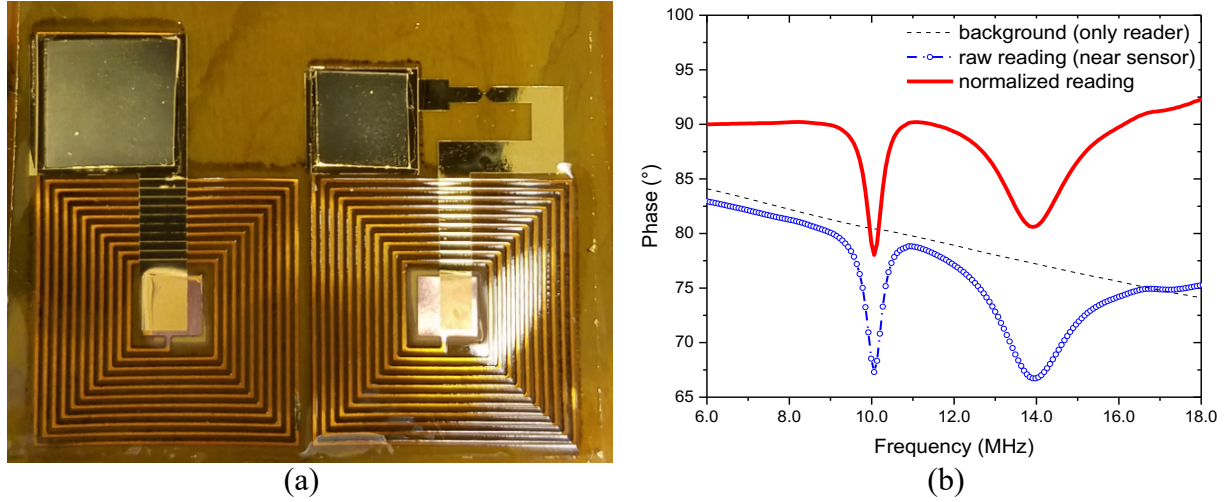


Figure 41. (a) Photo of a fabricated strain sensing system; (b) experimental phase-frequency plot from an inductor reader near the sensor.

## FINAL DESIGN OF THE SENSING SYSTEM

Based on experimental characterization of the various circuit components, a final thin film strain sensing is designed, fabricated and simulated. The first RLC circuit of the sensor intended to measure strain in the bone is designed with an inductive element with  $D_{out}=16.925$  mm,  $w=500$   $\mu\text{m}$ ,  $s=75$   $\mu\text{m}$ , and  $n=10$  resulting in an inductance and resistance of  $L_{ind}=1.386$   $\mu\text{H}$  and  $R_{ind}=0.934$   $\Omega$ , respectively. The capacitor integrated with the RLC circuit is designed with a nominal size of 9mm x 9mm (with an effective size of 7.70 mm x 7.70 mm governed by the top gold electrode) and polyimide dielectric thickness of 10  $\mu\text{m}$ ; this size capacitor has a capacitance of  $C_{cap1}=178.48$  pF. The size of the inductor and capacitor are selected to attain a specific resonant frequency associated with the RLC circuit. The second RLC circuit for hoop strain measurement employs an identical inductor as the first. However, to attain a distinct resonant frequency from the first RLC circuit, the capacitor in the second circuit is design with a nominal size of 7mm x 7mm (with an effective size 5.55 mm x 5.55 mm governed by the top gold plate) and polyimide dielectric thickness of 10  $\mu\text{m}$ ; this results in a capacitance of  $C_{cap2}=92.73$  pF. The resistive fuse element is designed to be 0.1 mm x 0.1 mm in area and 200 nm thick (Figure 40(a)). The initial, pre-yield resistance of the titanium element is measured to be  $R_{fuse}=15$   $\Omega$ . The final prototype fabricated with the aforementioned geometries is presented in Figure 41(a). To read the thin film wireless strain sensor, an inductive element with an inductance of  $L_{reader}=5$   $\mu\text{H}$  and resistance  $R_{reader}=0.1$   $\Omega$  is attached to the impedance analyzer to couple with the strain sensor.

## SIMULATION OF THE SENSING SYSTEM

Given the final wireless strain sensor design, an analysis of the sensor is performed in MATLAB to simulate its performance under applied strain. First, the unstrained impedance of the wireless

strain sensor is simulated. The impedance analyzer is simulated to sweep from 0.5 to 20 MHz. The sensor-reader coupled impedance phase ( $\theta$ ) and magnitude ( $|Z|$ ) is simulated by adding the responses of the impedance of the reader (without the sensor present) and the two RLC circuits of the sensor:

$$\theta = \theta_{reader} + \alpha\theta_{RLC1} + \alpha\theta_{RLC2} \quad (51)$$

where  $\alpha$  is a proportionality ratio of the two RLC circuit impedances due to the distance between the reader and the sensor. In this case,  $\alpha$  decreases with increasing distance between the reader inductor and the thin film wireless strain sensing system. As shown in Figure 42(a), the phase ( $\theta$ ) response due to the sweeping frequency shows the resonant frequencies of the two RLC circuits. The resonant frequency of an RLC circuit is,

$$f_r = \frac{1}{2\pi\sqrt{LC}} \quad (52)$$

For the given inductance and capacitances of the two circuits, the resonant frequencies are theoretically at  $f_{r1} = 10.1$  MHz and  $f_{r2} = 14.0$  MHz. As anticipated, the two resonant frequencies are not very distinguishable in the magnitude ( $|Z|$ ) plots of Figure 42(b), especially when they are closer to each other. Hence,  $\theta$  is chosen over  $|Z|$  as the feature space for identifying the resonant frequency of the RLC circuits.

Planar strain is simulated in the wireless strain sensor substrate assuming it is bonded to a PVC coupon loaded under uniaxial tension with free boundary conditions in the orthogonal direction (e.g.  $\sigma_x = 0$  and  $\sigma_y \neq 0$ ). By using equation (49), the gage factor for the capacitor,  $GF_c$ , under such strain condition is calculated ( $GF_c = 0.83$  for PVC). This allows the strain induced capacitance to be calculated as:

$$C(\varepsilon) = C_0 + \frac{\partial C}{\partial \varepsilon} \delta \varepsilon = C_0 + GF_c \cdot C_0 \cdot \delta \varepsilon \quad (53)$$

where  $C$  is the capacitance of the capacitor as a function of applied strain,  $\varepsilon$ , given the initial capacitance,  $C_0$ , and gage factor,  $GF_c$ . Using the phase peak of the RLC circuit, a gage factor for the resonant frequency can also be formulated. The RLC circuit resonant frequency gage factor,  $GF_{RLC}$ , is defined as:

$$GF_{RLC} = \frac{\partial f_r}{f_r \partial \varepsilon} = -\frac{1}{2} \frac{\partial C}{C \partial \varepsilon} = -\frac{1}{2} GF_c \quad (54)$$

Hence, the relationship between  $df_r$  and  $d\varepsilon$  is defined as:

$$df_r = GF_{RLC} \cdot f_r \cdot d\varepsilon \quad (2)$$

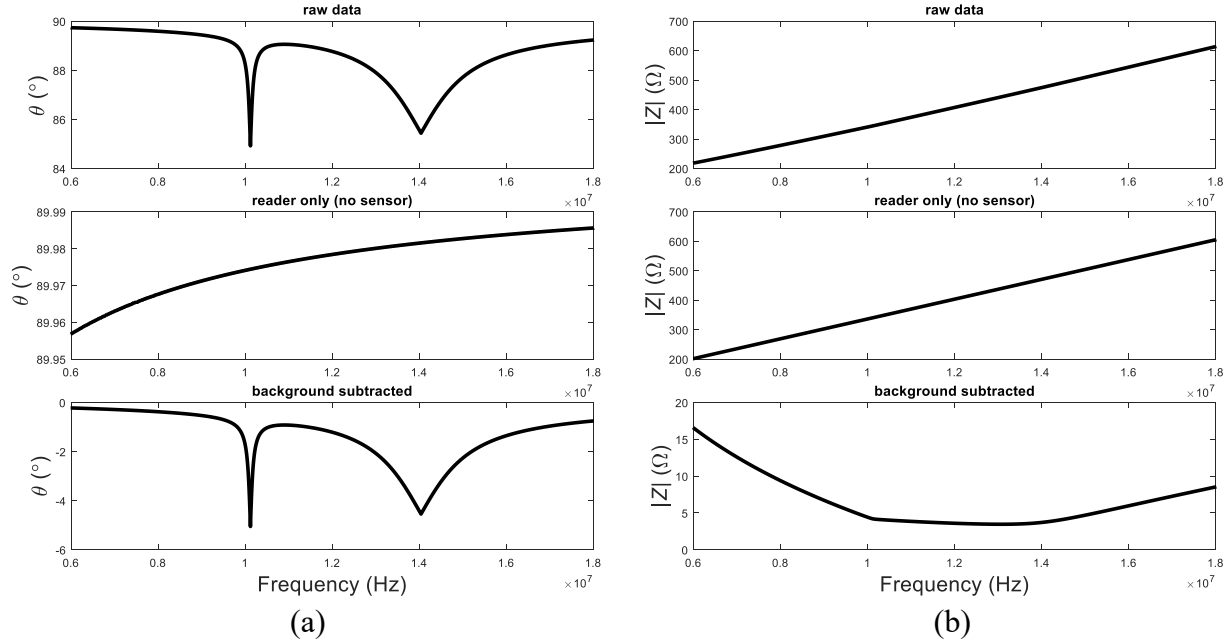


Figure 42. Simulated impedance plots of (a) phase,  $\theta$ , and (b) magnitude,  $|Z|$ , responses of the coupled system (wireless sensor and reader), reader only (without the wireless sensor) and that of the sensor (by removing the reader impedance from the simulated coupled system impedance).

where  $df_r$  and  $d\varepsilon$  are the resolutions of the resonant frequency and the strain, respectively. Assuming the wireless strain sensor is bonded to a PVC coupon, the  $GF_{RLC}$  is -0.415 and if 1000  $\mu\varepsilon$  is applied to the sensor, the first resonant frequency which is nominally at 10.1 MHz would see the resonant frequency change  $df_r = -4.2$  kHz. This is simulated in MATLAB as shown in Figure 43. In the simulation, strain is applied to the wireless strain sensor bonded to a PVC coupon ranging from -4000  $\mu\varepsilon$  to 4000  $\mu\varepsilon$  with a 1000  $\mu\varepsilon$  step. The phase of the first RLC circuit is plotted in Figure 43(a) for the -4000, 0 and 4000  $\mu\varepsilon$  cases while Figure 43(b) plots the extracted resonant peak frequency as a function of applied strain.

Figure 43(c) shows the phase impedance plots with various resistances of the fuse ( $R_0$ ,  $2R_0$ ,  $10R_0$ ). The second RLC circuit of the wireless strain sensor is also explored for varying changes in resistance associated with large strain events. In this simulation, the resistance of the fuse element is changed from  $R_0$  to  $20R_0$  to simulate the monotonically increasing hoop strain in the second RLC circuit. As shown in Figure 43(c), the absolute phase difference between the second valley and a reference point ( $f_0 = 1.1$  MHz),  $|\theta(f_{r2}) - \theta(f_0)|$ , can serve as a good indicator for threshold hoop strain. There is a nonlinear feature to the curve in Figure 43(d) as expected from the nonlinear behavior of the resistive element.

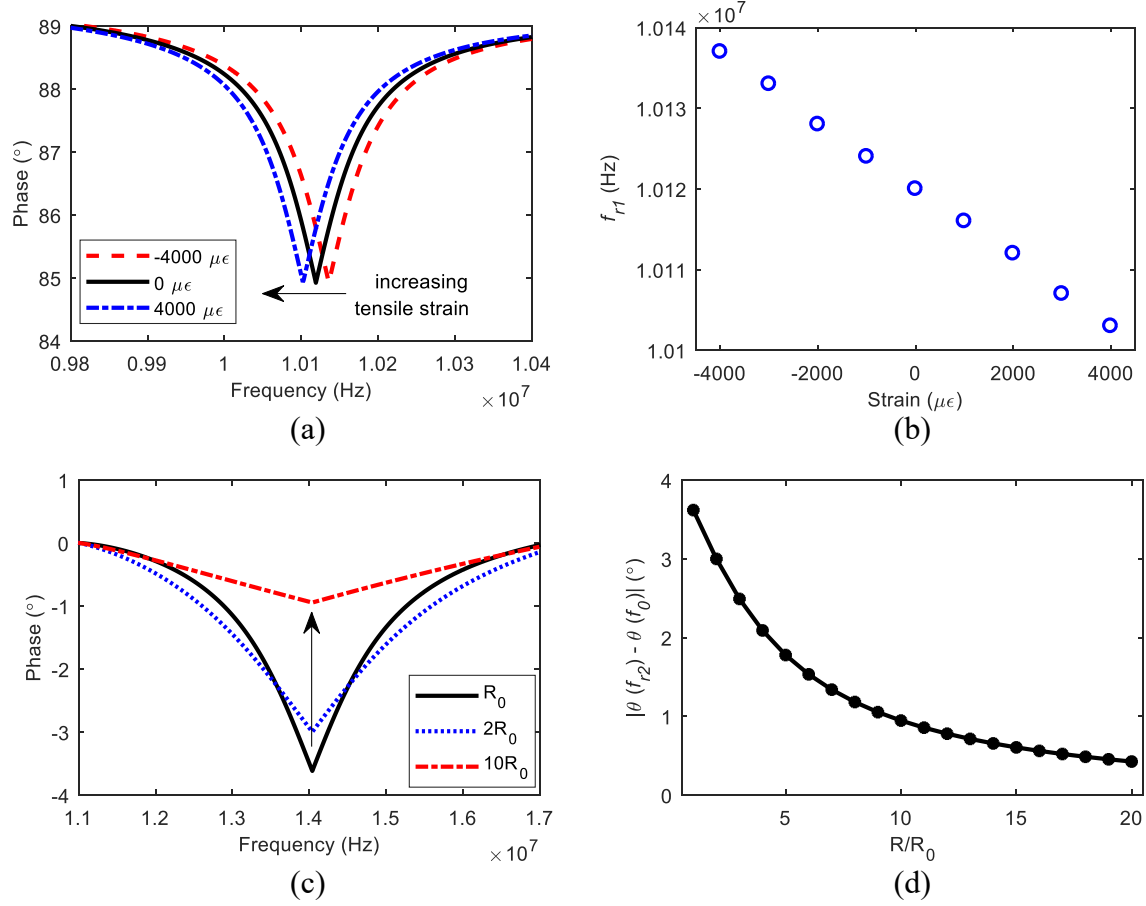


Figure 43. (a) Phase impedance plots near the resonant frequency of the 1<sup>st</sup> RLC circuit ( $f_{r1}$ ) with various strain condition; (b) plot of resonant frequency of the 1<sup>st</sup> RLC circuit versus strain; (c) phase impedance plots normalized to the reference point  $f_0 = 11$  MHz; (d) plot of the absolute phase difference between the 2<sup>nd</sup> valley and the reference point ( $|\theta(f_{r2}) - \theta(f_0)|$ ) versus fuse resistances.

## EXPERIMENTAL VALIDATION OF THE WIRELESS STRAIN SENSING SYSTEM

### Phase Readout

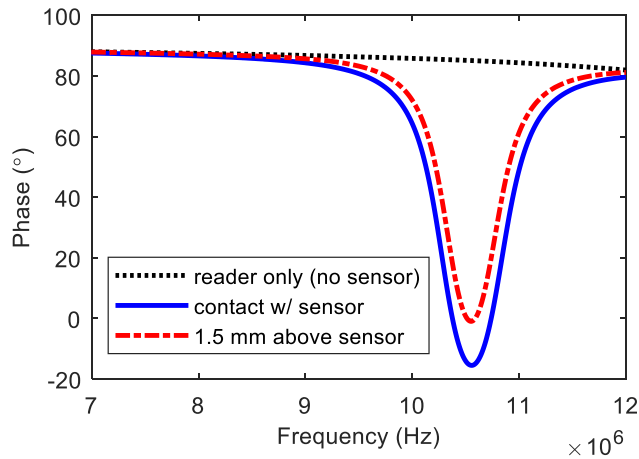
The fabricated wireless strain sensing system (Figure 41(a)) is interrogated using a read inductor connected to an impedance analyzer. The reactive phase response of the two RLC circuits are measured by the impedance analyzer under a sweep of AC frequencies. Valley features can be observed in the phase Bode plots around the resonant frequencies in Figure 41(b). The result in Figure 41(b) shows the phase response of the read inductor with and without the sensing system in the measurement range of the read inductor. As the read inductor is moved near the sensing system, the two valleys in the phase response corresponding to the resonant frequencies ( $f_{r1}$  and  $f_{r2}$ ) are visible; the resonant frequencies are similar to the simulated results as expected.

As show in Figure 44(a), a femur bone model is used with the conformable strain sensing system bonded to its surface. Figure 44(b) shows the impedance response data obtained by the coil reader with the phase of the first resonant frequency shown. As expected, as the reader is moved away from the thin film the magnitude of the peak reduces for the same level of energy provided by the impedance analyzer. The phase magnitude of the first RLC circuit is not critical in this application since the bone strain measurement is modulated on the first resonant frequency which is easily detectable even as the magnitude reduces. The tests validate the ability of the reader to inductively couple with the sensor even though it is mounted to a complex bone surface.

### Strain Measurements using the First RLC Circuit



(a)



(b)

Figure 44. (a) A photo of the femur bone with a thin-film sensor mounted at the bone end; (b) the phase bode plots of the thin-film sensor measured by an inductive reader.

The resonant frequency corresponding to the first RLC circuit is utilized for precision strain sensing. Strain is calculated using the shift of the first resonant frequency which is affected by the strain-induced change in capacitance. In order to obtain a precise resonant frequency from measured phase response, the valley of the phase magnitude is fit (as shown in Figure 45(a)) using Gauss functions at the resonant frequency. As shown in Figure 45(b), the strain induced capacitance change can be detected from the phase valley with the results indicating a near linear relationship between the measured resonance frequency and the applied strain. Linear regression is performed on the resonant frequency versus strain curve resulting in an R-squared value of 0.982. Thus, the first RLC circuit in the proposed sensing system is validated as a good indicator for strain with a sensitivity of 4.555 Hz/ $\mu\epsilon$ .

### **Hoop Strain Measurement using the Second RLC Circuit**

A gradually increasing tensile strain is applied to approximately 10,000  $\mu\epsilon$  with a step size of about 1,000  $\mu\epsilon$  to mimic hoop strain as bone growth occurs in an osseointegrated implant (shown in Figure 32(b)). The phase valley corresponding to the second RLC circuit is expected to broaden and in effect disappear as the fuse fails under large strain.

The signal from the reader alone (background) is first subtracted from the raw data, which is obtained when the read inductor is interrogating near the sensor. As shown in Figure 45(c), the resulting impedance phase plot is then normalized by shifting it to start from a 90° phase at 6.0 MHz. This normalization stage is done to enhance the visualization of changes in impedance phase as large strain is experienced. Valley fitting is again performed using a Gauss function in order to obtain an accurate measurement of the second RLC circuit resonance frequency.

At each loading step, the two valleys are observed by sweeping the frequency using the impedance analyzer over a wide range (e.g. 6 MHz – 18 MHz). Then the data around each valley is collected with more precision by sweeping over a narrower frequency range. The first valley from the first RLC circuit is shown in Figure 45(c) from 9.0 MHz to 11 MHz and the second valley from the second RLC circuit is shown in Figure 45(d) from 11 MHz to 17 MHz. The plots in Figure 45(c) and (d) have been normalized by subtracting from the coupled impedance the impedance of the reader and by shifting the impedance phase plots to start at 90° at 9.0 MHz and 11 MHz, respectively. The results shown in Figure 45(d) and (e) reveal the phase valley of the second (hoop strain) RLC circuit generally broadens and decreases under increasing tensile strain starting at 4000  $\mu\epsilon$ . In this specimen, the fuse clearly fails at around 6600  $\mu\epsilon$ . Figure 45(e) shows the plot of the absolute phase difference between the second valley and the reference point ( $|\theta(f_{r2}) - \theta(f_0)|$ ) versus monotonically increasing strain. The abrupt drop starting from around 5000  $\mu\epsilon$  to 6000  $\mu\epsilon$  indicates the efficiency of using  $|\theta(f_{r2}) - \theta(f_0)|$  as an efficient indicator for representing large threshold hoop strain in osseointegration applications. Two other samples of the sensing systems are tested showing fuse failure at similar strains. The results clearly illustrate the proposed sensing system as a viable means for monitoring the bone growth in OI prosthesis applications.

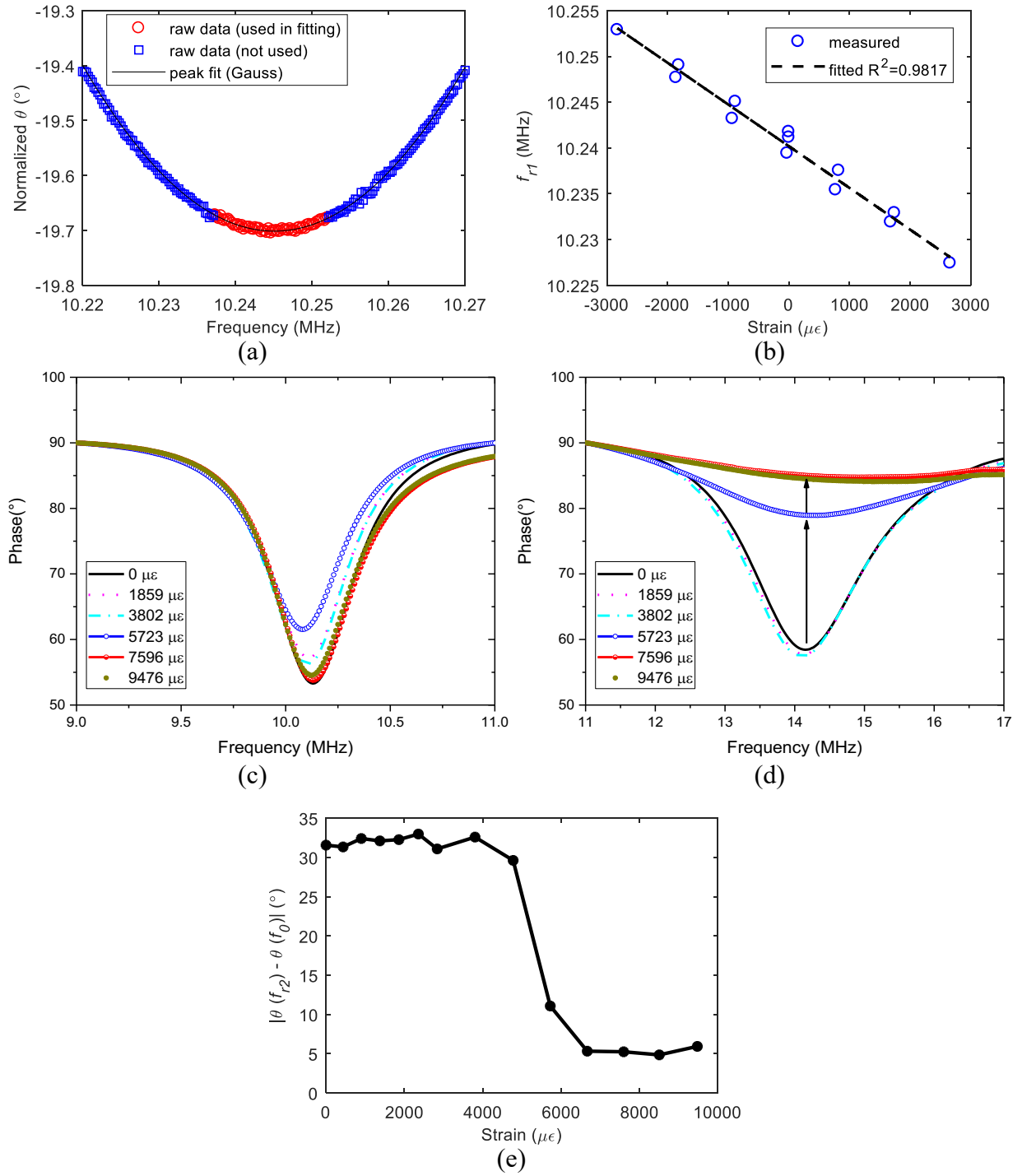


Figure 45. Plots of (a) an examples of gauss valley fitting near the resonant frequency of the 1<sup>st</sup> RLC circuit, (b) response of the resonant frequency to the applied strain, (c) 1<sup>st</sup> valley (normalized) in the phase response from the 1<sup>st</sup> RLC circuit, (d) 2<sup>nd</sup> valley (normalized) in the phase response from the 2<sup>nd</sup> RLC circuit due to the monotonically increasing tensile strain, and (e) plot of  $|\theta(f_{r2}) - \theta(f_0)|$  versus monotonically increasing strain.



## SUMMARY

In this section, the characterization of the components and the integrated systems are carried out *prior to* the simulation and experimental validation of the fully integrated strain sensing system. The individual circuit components are characterized experimentally and found to agree closely with theory. For the fully integrated strain sensing system, the first RLC circuit is validated for measurement of bone strain within a lower range of strain (*e.g.*, from -3000 to 3000  $\mu\epsilon$ ). The sensitivity of the first RLC circuit to strain is 4.555 Hz/ $\mu\epsilon$ . Monotonically increasing tensile strain is applied to the sensing system to mimic the hoop strain of a bone under compression osseointegration. Failure behavior of the fuse element in the second RLC circuit is observed within the impedance phase plots obtained by the inductor reader coupled with the nearby sensing system. The results validate both the proposed hoop strain sensing architecture and the utilization of a mechanical-electrical design of a thin film metal fuse in such sensing systems.

## SECTION 7: CONCLUSIONS

In this study, a unified *in vivo/ex vivo* sensing strategy is proposed to monitor the operation and environment of OI prostheses over their complete operational lifecycles. This comprehensive monitoring architecture is capable of providing the medical community quantifiable data after surgery. In the study, four states of OI prostheses are considered when designing and optimizing the monitoring system: 1) post-surgery development of osseointegration, 2) looseness of the fixture in the bone, 3) bone fracture, and 4) the development of callous in a compress-type OI prosthesis.

Guided waves are proposed as the *ex vivo* approach to interrogate the prosthesis-bone interface after surgery for clinical decision making (*e.g.*, when can an osseointegrated prosthesis be loaded?) and long-term performance monitoring over the lifecycle of the prosthesis. This *ex vivo* active sensing strategy is conducted from outside the body using the exposed percutaneous end of the prosthesis. Specifically, piezoelectric wafers are bonded to the prosthesis to introduce guided wave into the prosthesis fixture. Reflected guided waves are employed to assess the degree of osseointegration, loosening of the prosthesis, and bone fracture based on a scalar energy metric. The functionality of the guided wave sensing strategy is validated in the laboratory on models consisting of titanium femoral stems implanted in synthetic sawbones. First, the theory of tuning guided waves in solid cylindrical rods using perfectly bonded PZT wafers is developed. The optimization of the length of the PZT and the excitation frequency are achieved based on the tuning curves of longitudinal and flexural waves to enhance the accuracy of the proposed technique. Next, the study explored the use of longitudinal waves to monitor osseointegration at the bone-prosthesis interface. Osseointegration is mimicked by increasing the elastic modulus and density of the bone at the prosthesis surface. The energy of received longitudinal guided waves decrease with the healing processing as is validated by both numerical and experimental models. Full osseointegration results in approximately a 50% change in longitudinal wave energy. To verify the sensitivity of the longitudinal wave model on changes in an interface between the prosthesis and bone, experimental results were conducted with epoxy serving as a surrogate for bone healing. In addition, the separation of the prosthesis from the bone was also studied via pull-out experiments whose results show the wave energy has a significant increase with pullout. Hence, the proposed strategy is sensitive and selective to both osseointegration and prosthesis loosening. These results demonstrate the potential of guided waves for clinical evaluation of the bone-prosthesis interface. The study also offered preliminary investigation of flexural waves to identify bone fracture. Numerical models revealed the potential for identifying fracture and its relative location in the bone. However, these results require verification from experimental tests.

*In vivo* sensing is also proposed using a passive wireless strain sensing system based on thin film fabrication methods. A thin film multifunctional strain sensor measuring low level bone strain and high levels of hoop strain associated with bone growth is specifically explored. Thin film circuit components, including parallel plate capacitors, square coil inductors and miniaturized resistive fuses, are fabricated and patterned using biocompatible materials in a traditional lithographic process. The characterization of the components and the integrated systems are carried out *prior to* the simulation and experimental validation of the fully integrated strain sensing system. The individual circuit components are characterized experimentally and found to agree closely with theory. For the fully integrated strain sensing system, the first RLC circuit is validated for

measurement of bone strain within a lower range of strain (*e.g.*, from -3000 to 3000  $\mu\epsilon$ ). The sensitivity of the first RLC circuit to strain is 4.555 Hz/ $\mu\epsilon$ . Monotonically increasing tensile strain is applied to the sensing system to mimic the hoop strain of a bone under compression osseointegration. Failure behavior of the fuse element in the second RLC circuit is observed within the impedance phase plots obtained by the inductor reader coupled with the nearby sensing system. The results validate both the proposed hoop strain sensing architecture and the utilization of a mechanical-electrical design of a thin film metal fuse in such sensing systems.

This study offers two approaches to monitoring OI prostheses. Future work should focus on refining the monitoring methods to optimize them for potential use in a clinical setting. Some challenges anticipated in transition these methods to human subjects is the sensitivity of the methods to soft tissue and the ability to establish a robust baseline behavior of the guided waves. In the case of the implantable sensors, one challenge will be how the sensor can be bonded to human bones. Finally, future work should revisit the actual mechanical design of the prosthesis to co-optimize its design for both mechanical strength (for which it is solely designed) and the ability to serve as a sensitive wave guide.

## REFERENCES

1. Ziegler-Graham K, MacKenzie EJ, Ephraim PL, et al. Estimating the prevalence of limb loss in the United States: 2005 to 2050. *Archives of Physical Medicine and Rehabilitation* 2008; 89(3): 422-429.
2. Vertriest S, Coorevits P, Hagberg K, et al. Static load bearing exercises of individuals with transfemoral amputation fitted with an osseointegrated implant: loading compliance. *Prosthet Orthot Int* 2017; 41(4): 393-401.
3. Aaron RK, Herr HM, Ciombor DM, et al. Horizons in prosthesis development for the restoration of limb function. *J Am Acad Orthop Sur* 2006; 14(10): S198-S204.
4. Tillander J, Hagberg K, Hagberg L, et al. Osseointegrated titanium implants for limb prostheses attachments: infectious complications. *Clinical Orthopaedics and Related Research* 2010; 468(10): 2781-2788.
5. Sullivan J, Uden M, Robinson K, et al. Rehabilitation of the transfemoral amputee with an osseointegrated prosthesis: the United Kingdom experience. *Prosthetics and Orthotics International* 2003; 27(2): 114-120.
6. Frölke J, Leijendekkers R and van de Meent H. Osseointegrated prosthesis for patients with an amputation. *Der Unfallchirurg* 2017; 120(4): 293-299.
7. Tyler WK, Healey JH, Morris CD, et al. Compress periprosthetic fractures: interface stability and ease of revision. *Clinical Orthopaedics and Related Research* 2009; 467(11): 2800-2806.
8. Xu W and Robinson K. X-ray image review of the bone remodeling around an osseointegrated trans-femoral implant and a finite element simulation case study. *Annals of Biomedical Engineering* 2008; 36(3): 435-443.
9. Shalabi MM, Wolke JG, Cuijpers VM, et al. Evaluation of bone response to titanium-coated polymethyl methacrylate resin (PMMA) implants by X-ray tomography. *Journal of Materials Science: Materials in Medicine* 2007; 18(10): 2033-2039.
10. Vayron R, Mathieu V, Michel A, et al. Assessment of *in vitro* dental implant primary stability using an ultrasonic method. *Ultrasound in Medicine and Biology* 2014; 40(12): 2885-2894.
11. Pye A, Lockhart D, Dawson M, et al. A review of dental implants and infection. *Journal of Hospital Infection* 2009; 72(2): 104-110.

12. Bencharit S, Byrd WC, Altarawneh S, et al. Development and applications of porous tantalum trabecular metal-enhanced titanium dental implants. *Clinical Implant Dentistry and Related Research* 2014; 16(6): 817-826.
13. Kramer M, Tanner B, Horvai A, et al. Compressive osseointegration promotes viable bone at the endoprosthetic interface: retrieval study of Compress® implants. *International Orthopaedics* 2008; 32(5): 567-571.
14. Hagberg K and Brånemark R. One hundred patients treated with osseointegrated transfemoral amputation prostheses-rehabilitation perspective. *J Rehabil Res Dev* 2009; 46(3): 331-344.
15. Wang W and Lynch JP. Ultrasonic longitudinal waves to monitor the integration of titanium rods with host bone. *Proc SPIE*, Portland, OR, USA, 2017, pp. 1016829-1016810.
16. Rose JL. *Ultrasonic waves in solid media*. Cambridge University Press, Cambridge, England, 2004.
17. Graff KF. *Wave motion in elastic solids*. Dover Publication, New York, NY, 2012.
18. Gazis DC. Three-dimensional investigation of the propagation of waves in hollow circular cylinders. I. analytical foundation. *The Journal of the Acoustical Society of America* 1959; 31(5): 568-573.
19. Silk M and Bainton K. The propagation in metal tubing of ultrasonic wave modes equivalent to Lamb waves. *Ultrasonics* 1979; 17(1): 11-19.
20. Hodgkinson R and Currey J. Young's modulus, density and material properties in cancellous bone over a large density range. *Journal of Materials Science: Materials in Medicine* 1992; 3(5): 377-381.
21. Giurgiutiu V. *Structural health monitoring: with piezoelectric wafer active sensors*. Academic Press, Cambridge, MA, 2007
22. Zhang S, Jiang W, Meyer Jr RJ, et al. Measurements of face shear properties in relaxor-PbTiO<sub>3</sub> single crystals. *Journal of Applied Physics* 2011; 110(6): 064106.
23. Wang W, Zhou W, Wang P, et al. In-plane shear piezoelectric wafer active sensor phased arrays for structural health monitoring. *Proc SPIE*, 2016, pp. 98030H-98030H.
24. Wang W, Lynch JP and Li H. Damage detection in metallic plates using d36 piezoelectric phased arrays. *Composite Structures* 2016; 9(12).
25. Crawley EF and de Luis J. Use of piezoelectric actuators as elements of intelligent structures. *AIAA Journal* 1987; 25(10): 1373-1385.

26. Ojanen X, Töyräs J, Inkinen SI, et al. Differences in acoustic impedance of fresh and embedded human trabecular bone samples - scanning acoustic microscopy and numerical evaluation. *The Journal of the Acoustical Society of America* 2016; 140(3): 1931-1936.
27. Saied A, Raum K, Leguerney I, et al. Spatial distribution of anisotropic acoustic impedance assessed by time-resolved 50-MHz scanning acoustic microscopy and its relation to porosity in human cortical bone. *Bone* 2008; 43(1): 187-194.
28. Raum K. Microelastic imaging of bone. *IEEE Transactions on Ultrasonics, Ferroelectrics, and Frequency Control* 2008; 55(7): 1417-1431.
29. Wang W and Lynch JP. Identification of bone fracture in osseointegrated prostheses using Rayleigh wave methods. *Proc SPIE*, 2018, pp. 106000T.
30. Alleyne D and Cawley P. A two-dimensional Fourier transform method for the measurement of propagating multimode signals. *The Journal of the Acoustical Society of America* 1991; 89(3): 1159-1168.
31. HKS Inc. *ABAQUS/Standard user's manual*. Hibbitt, Karlsson & Sorensen, Inc., Manchester, England, 2001.
32. Ribolla EL and Rizzo P. Modeling the electromechanical impedance technique for the assessment of dental implant stability. *Journal of Biomechanics* 2015; 48(10): 1713-1720.
33. Taheri E, Sepehri B and Ganji R. Mechanical validation of perfect tibia 3D model using computed tomography scan. *Engineering* 2012; 4(12): 877-880.
34. Krone R and Schuster P. An investigation on the importance of material anisotropy in finite-element modeling of the human femur. SAE Technical Paper 2006-01-0064, 2006.
35. Integrum AB, OPRA implant system instruction for use <https://www.accessdata.fda.gov/scripts/cdrh/cfdocs/cfhde/hde.cfm?id=h080004>. 2015.
36. Manjubala I, Liu Y, Epari DR, et al. Spatial and temporal variations of mechanical properties and mineral content of the external callus during bone healing. *Bone* 2009; 45(2): 185-192.
37. Friswell M and Mottershead JE. *Finite element model updating in structural dynamics*. Springer, London, England 2013.
38. Bishop C. *Pattern recognition and machine learning*. Springer, New York 2007.
39. Rasmussen CE and Williams CK. *Gaussian processes for machine learning*. MIT Press Cambridge, MA 2006.

40. Hagberg K and Brånemark R. One hundred patients treated with osseointegrated transfemoral amputation prostheses—rehabilitation perspective. *J Rehabil Res Dev* 2009; 46(3): 331-344.
41. Lynch JP, Farrar CR and Michaels JE. Structural health monitoring: technological advances to practical implementations. *Proceedings of the IEEE* 2016; 104(8): 1508-1512.
42. Kalansuriya P, Bhattacharyya R and Sarma S. RFID tag antenna-based sensing for pervasive surface crack detection. *IEEE Sensors Journal* 2013; 13(5): 1564-1570.
43. Cho C, Yi X, Li D, et al. Passive wireless frequency doubling antenna sensor for strain and crack sensing. *IEEE Sensors Journal* 2016; 16(14): 5725-5733.
44. Kim J, Wang Z and Kim WS. Stretchable RFID for wireless strain sensing with silver nano ink. *IEEE Sensors Journal* 2014; 14(12): 4395-4401.
45. Yi X, Cho C, Cooper J, et al. Passive wireless antenna sensor for strain and crack sensing—Electromagnetic modeling, simulation, and testing. *Smart Materials and Structures* 2013; 22(8): 085009.
46. Jia Y, Sun K, Agosto FJ, et al. Design and characterization of a passive wireless strain sensor. *Measurement Science and Technology* 2006; 17(11): 2869.
47. Caizzone S and DiGiampaolo E. Wireless passive RFID crack width sensor for structural health monitoring. *IEEE Sensors Journal* 2015; 15(12): 6767-6774.
48. Wood SL and Neikirk DP. Passive sensors for infrastructure monitoring. *Proc SPIE*, 2009, pp. 729202.
49. Zhang Y and Bai L. Rapid structural condition assessment using radio frequency identification (RFID) based wireless strain sensor. *Automation in Construction* 2015; 54(1-11).
50. Seo J-M, Kim SJ, Chung H, et al. Biocompatibility of polyimide microelectrode array for retinal stimulation. *Materials Science and Engineering: C* 2004; 24(1-2): 185-189.
51. Demann ET, Stein PS and Haubenreich JE. Gold as an implant in medicine and dentistry. *Journal of Long-term Effects of Medical Implants* 2005; 15(6).
52. Mohan SS, del Mar Hershenson M, Boyd SP, et al. Simple accurate expressions for planar spiral inductances. *IEEE Journal of Solid-State Circuits* 1999; 34(10): 1419-1424.